Wesleyan University ♦ Department of Physics

Probing Complex Dynamics via Loschmidt Echoes

By
Joshua David Bodyfelt
Faculty Advisor: Dr. Tsampikos Kottos

A Dissertation submitted to the faculty of Wesleyan University in partial fulfillment of the requirements for the Degree of Philosophiæ Doctor

Middletown, Connecticut May 2009

Abstract

This dissertation investigates echo dynamics (Loschmidt Echo) due to small perturbations, in the framework of disordered media where Anderson localization is the dominant mechanism dictating the transport. Various temporal decay laws of the Loschmidt Echo (LE) were identified and shown to accurately probe the diffusive, localized, or even critical nature of the transport. Our theory, based on Random Matrix Theory modeling, agrees perfectly with scattering echo experiments (that we have recently proposed and performed) on a quasi-one-dimensional microwave cavity filled with randomly distributed scatterers.

Dedication

I dedicate my work in this dissertation to Virginia L. Kraen, a woman with a sassy wit gained from quotidian observation of the world around her. She has always believed in my potential, and taught me that there are facts worth knowing that simply can't be found in any textbook - especially the importance of keeping a light heart and a heavy laugh in the face of troubles. Even though she is not able to physically see the culmination of my efforts, I know she takes breaks from dancing with Grandpa to check up on me, watching with the pride of our venerable Mater Familia. Grandma, this lemonade from my decade of lemons is for you...

Acknowledgements

I would maintain that thanks are the highest form of thought, and that gratitude is happiness doubled by wonder.

-Gilbert K. Chesterton

If you can judge a man by the company that he keeps, this dissertation is both my gentleman's club and courtroom. It is the culmination of my aspirations and dreams to date; but more importantly, it is the start of another journey. There are no words that can be adequately said to repay the Caesar's due I owe my fellow travelers, but perhaps I may be able to make a small tribute here.

First and foremost, thanks to my advisor, Dr. Tsampikos Kottos. I have been an incessant thorn in his side the past few years, and he certainly ought to have abandoned me at various times; however, he always has strongly supported me throughout it all. Thanks are definitely due for his patience with these agitations. I also owe him a debt of gratitude for giving me an image of what it means to be a scientist. This includes: (a) a genuine care, responsibility, and fellowship towards one's students - rotisserie lambs at Easter, sushi feasts, and Mania's late-night pasta dinners far outweigh the typical graduate Ramen meals! (b) always maintaining a professional manner in lectures and publications, and (c) a constant vigil of skepticism in every calculation. Thanks goes toward his tremendous assistance in the preparation of this manuscript. Lastly, I owe him the biggest debt for taking a chance on accepting a complete stranger into his group, and reshaping him into the professional I am now. Tsampikos, there simply aren't enough words in any human tongue, whether that be English or Greek; regardless I will simply say "$\Sigma\alpha\varsigma\ \epsilon\upsilon\chi\alpha\varrho\iota\sigma\tau\upsilon\mu\epsilon$", and look forward to our future endeavors!

I also wish to thank my Ph.D. committee of Drs. Reinhold Blümel, Fred Ellis, & Doron Cohen for spending their precious time in reading this dissertation, and for all their interesting questions and discussions during my past research presentations. I would also like to extend a thanks to the remaining faculty of the Wesleyan Physics Department, especially to Dr. Francis Starr for the BBQ invites and Anna Milardo for her constant efforts in maintaining a smooth-sailing

department. Additionally, thanks to the U.S.-Israel Binational Science Foundation (BSF) and the Deutsche Forschungsgruppe (DFG) 760 for scientific funding.

A big "Vielen Dank" goes to Hans-Jürgen Stöckmann and Ulrich Kuhl for hosting me during my Summer 2007 visit to Marburg, and introducing me to the German 'Lebengenußen'. Also to Ulle, thanks for being there for me in Argentina! Du bist einen getreuen Freund.

For my peers and friends: may those of us remaining in academia have globally mixing trajectories! I'd especially like to single out Gim Seng Ng and Moritz Hiller. You two have been instrumental in helping me set a professional standard for myself through our collaborations. Honorable mentions are due to Pennan Chinnasamy, Fredrick Sußmann, Steve-O Coppage, Rangga Budoyo, Mei Zheng, the Puelz Pair, Danny Dan Blum, and Iulian Clapa. Great thanks also to all my 'non-physics' friends who help keep me grounded - especially Corey Schmidt, Pat Heimann, and Bliss & Iago Ragsdale.

Many, many, many (and so on ad infinitum) thanks are due to my family, especially my folks. Their endearing love and support has kept me sane through all my tough daytrips to the crunch. Dad's acceptance of physics as "a real job" (albeit the haircut is still needed) and Mom's "I don't get it, but I get you love doing it" have strengthened my decision to pursue academic physics. Mom and Dad, I will never be able to repay you for all that you have done for me - I can only hope the pride in having a son finally fulfill a childhood dream is enough reward. To my eldest little sister - Virg, the weekends in Jersey were good times, especially us two poor college students fighting over the Texas Weiner check. Hopefully we can continue the fights across the pond. To my middle little sister Martha and her husband Shahin, thank you so much for showing me D.C. is something besides a crooks' haven, including delicious Belgian feasts and walks with the Good Doctor. To my youngest sister Margaret and her husband Russ, thanks for keeping your noses to the grindstones -inspiring me to do likewise; 'Dr. Maggie' and 'Head Chef Russ' certainly have a nice ring! A honorable mention for Uncle Floyd and Aunt Eva, whose childhood gift of Madeleine L'Engle's "A Wrinkle In Time" started me down this winding road.

Lastly, the greatest thanks goes to the Big Guy Upstairs and Gaia. They have installed in me both the potential I try hard to meet and my flaws to gain insight and forge ahead. Their Providence reminds me daily to stay Human...Thank you everyone, and I hope I can one day make the impact for someone that y'all have had on me. Cheers!

Contents

Chapter 1

The Complex World We Face

I would not give a fig for the simplicity this side of complexity, but I would give my life for the simplicity on the other side of complexity.

-Oliver Wendell Holmes, Sr.

1.1 The Motivation for Research

Wave propagation in complex media is an interdisciplinary problem holding both fundamental and applied interests. Examples abound, such as light propagating in fog and clouds, or electromagnetic waves passing through interstellar materials. Electronic, acoustic and electromagnetic waves are used to transmit energy and information and to control, probe and image our world. The propagation of waves draws interest in both complex media occurring naturally in electronic and photonic devices, and complex media occurring artificially in metamaterials, which are fabricated to highlight the characteristics of the wave interaction with

structural elements on the scale of the wavelength. The particularities of wave interactions of different types of waves and different systems are the basis of our rich experience of the world, but their common characteristics provide a framework for understanding transport and often lead to new applications.

One such characteristic is wave interference, resulting in complex wave-patterns due to scattering from a confining complex potential. This complex potential models the inherent structure of the environment, such as irregular boundaries and scattering regions. The effect of complexity is then seen in the wave interference, and it is interference that is responsible for various transport phenomena.

Another source of complexity in wave transport results from interactions. An exemplary system that portrays an interaction-induced complexity is atomic Bose-Einstein Condensates (BECs) in optical lattices. Tuning of the interatomic interaction strength allows the study of transitions from integrable to chaotic behavior - even allowing novel quantum phase transitions. In order to observe such behaviors of a wave, one needs to resolve the wave itself - a daunting task (as of yet impossible, in the case of electron waves in nanowires). The question is then how else may complexity be probed?

1.2 The Role of this Dissertation

This dissertation attempts to answer the above question - it primarily focuses on developing dynamical measures that probe the degree of complexity of a system

via its sensitivity to small external perturbations. The stability of the complex dynamics under such perturbations is quantified by measuring "echoes" of the unperturbed system within the perturbed one. Such a measure is called a "Loschmidt echo" or "fidelity". The goal of this dissertation is to utilize this measure to quantify the degree of complexity of various systems and deduce conclusions on their transport characteristics. Although fidelity has been studied much during the last 7 years, the main emphasis in the literature was on wave systems with classical chaotic dynamics. Very little was done for the case where complexity is an outcome of many body interactions and even less was known about the fidelity of random media showing Anderson localization. Our main contribution is done, in fact, for this last category of systems. Via a detailed study (both theoretical and experimental), we are able to propose fidelity as a new measure to quantify randomness (and thus localization) of the medium at hand.

Within Chapter 2, a general physical background is presented to give an overview of complex dynamics, both in classical and quantum systems. Useful concepts such as phase space, parametric Hamiltonians, and correlations will be introduced as tools to 'see' complexity and to motivate a correspondence between classical and quantum systems. A modeling technique for complex wave/quantum dynamics, called Random Matrix Theory, will then be introduced. The chapter will conclude with the application of Random Matrix Theory to statistical concepts. The tools developed in this chapter will give a general framework for later discussions about quantifying/calculating fidelity.

Within Chapter 3, fidelity is historically presented. Both quantum and classical versions are discussed and are connected to the notion of fidelity as a measure of the sensitivity of the dynamics in small perturbations. We will also discuss how fidelity is connected with other well-studied dynamical quantities like local density of states, recurrence, and survival probability. Finally, we will distinguish the decay of fidelity depending on the strength of the perturbation, in three regimes. In each of these regimes, we will present the available methods that can be used in order to calculate it. The chapter will close with fidelity as a probe of complexity.

Within Chapter 4, the first system which we apply fidelity is the Bose-Hubbard Hamiltonian, which describes interacting boson particles placed into a finite periodic potential (lattice). We find echoes associated with non-universal structures that dominate the energy landscape of the perturbation operator. Despite their classical origin, these echoes persist deep into the quantum (perturbative) regime and can be described by an improved random matrix modeling. In the opposite limit of strong perturbations, classical considerations reveal the importance of self-trapping phenomena in the echo efficiency [1].

Within Chapters 5-6, a question is posed and answered: the existing literature on fidelity deals mainly with chaotic systems, but can fidelity also identify localization phenomena? In Chapter 5, we utilize a banded RMT approach to derive a novel decay law for localized systems, in which the localization characteristics are encoded in the decay rates. We verify our analytical result with numerics.

Within Chapter 6, a variant of the standard fidelity, based on scattering matrices, is used to study localization in an experimental framework. The experiments are performed using microwave propagating quasi-one-dimensional waveguides with scatterers [2], and the experimental data verifies our model.

Within Chapter 7, we investigate a disordered system at a critical point, at which the wavefunction becomes multifractal, caught between the case the localized and chaotic. Using a random matrix approach, for strong perturbations we find the fidelity decays algebraically, with a rate related to the correlation dimension of the local density of states [3].

Within Chapter 8 an epitome is given, and future potentials for research avenues along the vein of this dissertation are presented for consideration.

This dissertation was based in a number of papers published throughout the years [1–3]. Within Appendix A we present our published work, Ref. [4], as an alternative characterization of localization in random media. The main portion of the appendix deals with the notion of the energy derivative of scattering phases - the Wigner delay times. Three different 1D physical systems (i.e. disorder potentials) are used in our investigations: an electronic sample (Anderson), a microwave waveguide (correlated Kronig-Penny), and hard scatterers in an optical lattice (binary). From the resulting delay times, we are able to extract a universal scaling relation, *independent* of the disorder potential. Comparison to localization lengths shows similar scaling, suggesting Wigner delay time as a possible tool to probe localization behavior in 1D systems.

Appendix B.6 contains a lengthy derivation of the correlator seen in Chapter 7. Additional derivations and other information referred to within other chapters are also included within Appendix B.

Chapter 2

Complexity: To Quantify and Model

> *Tools arm the man. One can well say that man is capable of bringing forth a world; he lacks only the necessary apparatus, the corresponding armature of his sensory tools. The beginning is there.*
>
> -Novalis, Blüthenstaub

Within complex systems, the question arises "How is complexity quantifed and measured?" Along these lines, one may also ask "How can one theoretically model systems with complexity?" It is the purpose of this chapter to provide the reader with a brief perspective of some of these 'tools', whose role is to answer the two questions of quantification and modeling of complex systems. Although our presentation follows the traditional quantum chaology approach to quantification of complexity, we note that many of these tools and models will be used latter on, in the analysis and description of random media showing Anderson localization.

2.1 Describing a System Classically

In order to provide a complete deterministic description of the state of the system with classical Hamilton-Jacobi theory [5], the *degrees of freedom* (DOF) are defined. One degree of freedom is a pair of coordinates - typically position and momentum, (q, p) - that describe a point-like body (particle). For a collection of M particles, the degrees of freedom are the set $(q, p) = \{q_i, p_i\}$, which are indexed for an N-dimensional system as $i \in [1, 2, \ldots, d = M \times N]$. These coordinates are *canonical*: they have a delta Poisson bracket. For two functions $f(q, p)$ and $g(q, p)$, a Poisson bracket is defined as

$$\{f, g\} = \sum_i \left[\frac{\partial f}{\partial q_i} \frac{\partial g}{\partial p_i} - \frac{\partial f}{\partial p_i} \frac{\partial g}{\partial q_i} \right] \tag{2.1}$$

Therefore **canonicity** is

$$\{p_i, p_j\} = \{q_i, q_j\} = \delta_{ij}, \quad \{q_i, p_j\} = 0. \tag{2.2}$$

Another meaning of canonicity is the DOF are *independent* of one another. This independency gives a $2d$-dimensional manifold spanned by the DOF - this manifold is named the *phase space*.

Generally, we are interested in a *flow field* within the phase space. For a given body (say the m^{th}), as the system evolves in time, the body traces out a *trajectory* in phase space, denoted as $\{q_j(t), p_j(t)\}$, $j \in [m, m + N)$. The collection of all trajectories is a set of pathlines in a flow field, $\{q_i(t), p_i(t)\}$, $i \in [1, 2, \ldots, d =$

$M \times N$]. Given a set of initial conditions, $\{q_i(t_0), p_i(t_0)\}$, the first classical task is to find these pathlines. This is done via (generally numerical) integration of the Hamiltonian Equations of Motion (HEOMs)

$$\begin{aligned} \frac{dq_i}{dt} &= \frac{\partial H}{\partial p_i}, \\ \frac{dp_i}{dt} &= -\frac{\partial H}{\partial q_i} \end{aligned}$$

where H is the Hamiltonian, $H(q, p; t)$; a known function built from kinetic and potential energies that defines isopotentials within the flow field. The isopotential behavior of the Hamiltonian therefore gives a conservation in the flow - in fact, since the Hamiltonian measures energies, the conservation is one of energy.

Consider some set of state functions $\{A_k(q, p; t)\}$, which correspond to measurable observables of the system. In Hamilton-Jacobi theory, measured observables evolve in time as

$$\frac{dA_k}{dt} = \frac{\partial A_k}{\partial t} + \{A_k, H\} \tag{2.3}$$

where the second term is the Poisson bracket. In the quantum realm, the above equation looks very similar to the Heisenberg equations of motion, in particular the comparison of the Poisson bracket to quantum commutation, therefore the importance of Hamilton-Jacobi formalism in the development of quantum mechanics can not be overstated. One particular result from Eq.(2.3) is the idea of *constants of motion*. The condition for a state function to be an constant of motion is $\frac{dA_k}{dt} = 0$ - giving $\{A_k, H\} = 0$ and $A_k = A_k(q, p)$. Therefore, if the Poisson

bracket vanishes (i.e. the state function commutes with the Hamiltonian), and there is no explicit time-dependence then the state function remains constant for all time - they are 'constants of motion'. In turn, constants of motion create a dependencies in the DOF that allows the reduction of the phase space dimension, $2d \rightarrow 2d - k$, where k is the number of constants of motion.

Armed with the Hamiltonian and initial conditions, we have a complete deterministic description of the system. If complexity is present in system, it should therefore be manifest within the Hamiltonian and its associated dynamics.

2.2 Complex Signatures in Classical Phase Space

For a $2d$-dimensional phase space, there are generally $2d$ unknown variables. If the number of known constants of motion is $k = 2d$, the number of knowns equals number of unknowns and the system is 'solvable', in an analytical sense. In this case, the motion is said to be *integrable*. In the opposing case that the number of degrees of freedom is larger than the constants of motion (Poisson bracket commuting quantities), $2d > k$, we then encounter complex dynamics in phase space. The complex dynamics look stochastic (i.e. noisy), but stochastic systems require very large dimensions in their description - complex dynamics only require the condition $2d > k$.

There are two basic tenets of chaotic motion [6,7]. The first is an *extreme sensitivity to initial conditions*. Consider two initial points in phase space, separated by

an infinitestimal distance $\delta r(t_0) = |(q_1, p_1) - (q_2, p_2)| \ll 1$. As the two trajectories evolve in time, their separation grows as $\delta r(t) \approx e^{\lambda t}\delta r(t_0)$, with a positive rate given by the *Lyapunov exponent*, λ. However, extreme initial sensitivity is not enough to dictate chaotic motion. As an example, think of a simple pendulum in a gravitational field. Set two initial conditions on either side of the unstable fixed point at $\theta = \pi$. The separation in trajectories grows exponentially, but the motion remains integrable! It is not enough to have a **local** trajectory separation in phase space, but there must be a **global** meandering of these trajectories in phase space.

This global meandering is the second tenet of chaotic motion, and is conceptualized by *mixing and ergodicity*. Suppose there are two small uniform distributions of initial conditions in phase space, $\varrho_{1,2}(q(t_0), p(t_0))$, occupying meager fractional volumes, $f_{1,2}$ of the total phase space (V) at t_0, so that $\int \varrho_{1,2}(q(t_0), p(t_0))\, dV_{1,2} = 1$. For a time $t \gg t_0$, long enough so that $f_{1,2} \to 1$, both sets of trajectories visit all of accessible phase space; however $\left| f_2 - \int \varrho_2(q(t), p(t))\, dV_2 \right| < \epsilon$ for some arbitrarily small ϵ, **irrespective** of the volume V_1. A way to view this is presented in Fig. (2.1). As time progresses, the two separate subvolumes $V_{1,2}$ become "stretched, folded, and kneaded" until at t, the two are intermingled so that regardless of how far one zooms in phase space, the striations between $V_{1,2}$ (red and blue in the figure) are present - this is the definition of "mixing".

Ergodicity is a statistical concept related to mixing. Rather than two subvolumes evolved for a long timeframe, we have a large ensemble of subvolumes numbering

$R \gg 2$ that are evolved for a short time, t_s, such that $f_{1,2,\ldots,R}(t_s) \sim f_{1,2,\ldots,R}(t_0)$. An ergodic process is one in which the time average over a long time (t) for a *single* trajectory is equivalent to the ensemble average of trajectories over a short time

$$\frac{1}{|t-t_0|}\int_{t_0}^{t} \varrho_1(q(\tau),p(\tau))\,d\tau = \frac{1}{R}\sum_{r=1}^{R} \varrho_r(q(t_s),p(t_s)) \tag{2.4}$$

Non-integrable systems can then be said to have a *mixed* phase space, and are *ergodic*. As a last point to chaotic motion, it should be noted that for non-integrable systems, flow dictated by the HEOMs is generally *nonlinear*.

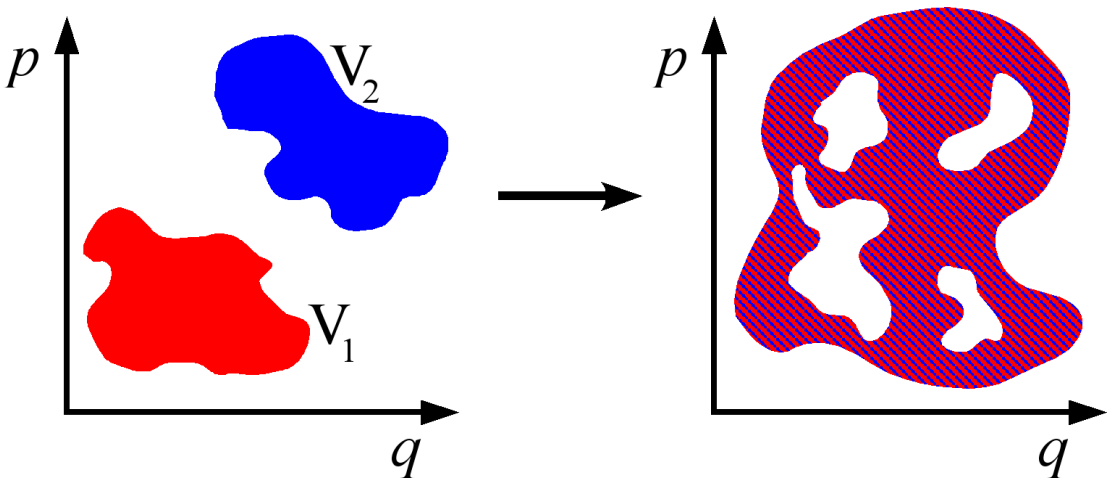

Figure (2.1): An illustrative definition of mixing. At t_0, two ensembles of initial conditions are presented in red and blue, respectively. At long times, the red/blue volumes become stretched and folded in on each other, to the extent that any zoom in on the phase space displays similar red/blue striations.

This is all easy to visualize if one has a two-dimensional phase space, but generally, systems have large dimensions. How can we visualize motion in large dimensional

systems? The answer is similar to what is done in the Visible Human Project ® [8] - a 3-D human is 'sliced' into 2-D images. Phase space can similarly be 'sliced' into *Poincaré sections*. A Poincaré section is a fixed subsurface S in phase space whose span is transverse to all flows that penetrate it [6,7]. Any time a trajectory tranversely penetrates the Poincaré section, it is marked. This is illustrated by a sketch in Fig. (2.2). In the left portion of the figure, closed trajectories of regular motion appear as lower-dimensional closed submanifolds - hypersurfaces become shells, shells become loops, loops become fixed points, and trajectories stay on these set paths in the ergodic limit (long time). Recall that such closed manifolds correspond to an integral of motion. The right portion of the figure contrastly shows a chaotic trajectory. It is **not** closed, and is folded back in on itself (mixing). In the ergodic limit (long time), the trajectory will puncture most of the available Poincaré section, creating a vastly filled image called "the chaotic sea".

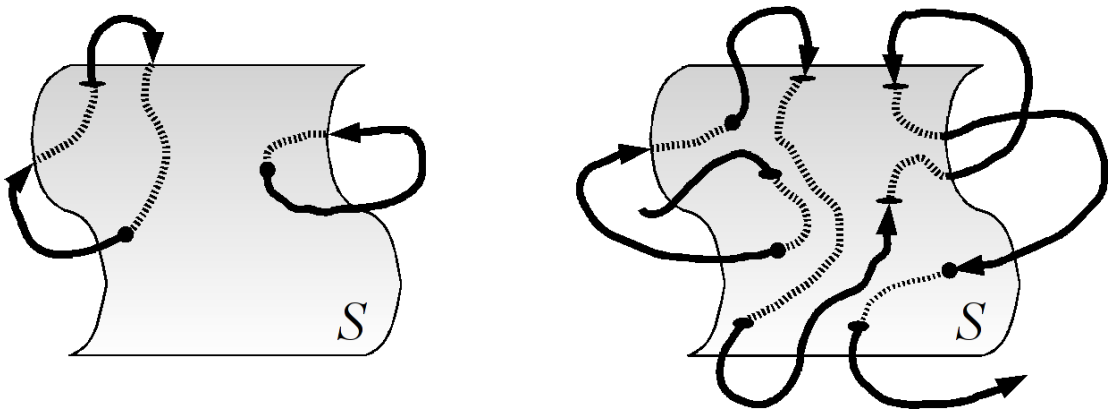

Figure (2.2): A sketch of transverse flow penetration through a Poincaré section. Solid lines are trajectory portions 'in front' of the surface, and dashed lines are those 'behind' the surface. Regular motion is seen in closed submanifolds (left), while chaotic motion creates a "sea" of penetrations (right) all across the Poincaré section.

Numerically, Poincaré sections are defined by fixing a subset of phase space to constant values, $\{q_j = \alpha_j, p_j = \beta_j\}, j < 2d$. For a two-dimensional Poincaré section (plot), a $2d-2$ set of constant values needs defined. It is important to note that several Poincaré sections may be needed in order to get a general picture of the dynamical behavior, especially for higher-dimensional systems. Typically, separate Poincaré sections are taken orthogonal to each other.

To conclude this subsection, let us state the original goal of observing complexity's manifestations in the trajectories. Regardless if one is using a $2D$ phase space or multiple Poincaré sections through a multidimensional phase space, chaotic trajectories locally diverge from one another with an exponential rate given by the Lyapunov exponent, and globally mix with each other ergodically. Local exponential divergence and global mixing are then responsible for the presence of a trajectory 'sea' seen in the phase-space/Poincaré sections. This is the manifestation of complexity within classical dynamics.

2.3 Parametric Systems

It is very common in physical circumstances to encounter examples where in order to probe the behavior of the system, first one must interact with it, i.e. to *perturb* it. In these cases, the Hamiltonian is described as $H(p, q; x)$ where (p, q) are some generalized canonical coordinates and x is a parameter that quantifies the degree of perturbation to the system. In cases that $\delta x = x - x_0$ is classically very small

(such that $H(q,p;x)$ and $H(q,p;x_0)$ globally generate similar dynamics), one can linearize the perturbed Hamiltonian

$$H(q,p;x) \approx H(q,p,x_0) + \delta x \cdot \mathcal{F}(q,p) \tag{2.5}$$

where $\mathcal{F}(q,p)$ is a perturbative function that acts as a 'generalized force' on the system, and δx plays the role of a constant perturbative strength. The crossover where this linearization fails is δx_c - often empirically found from the Hamiltonian deformation.

The parametric changes in energies are characterized by the reversible fluctuations of the Hamiltonian's generalized force

$$\mathcal{F}(t) = -\frac{\partial H(q,p;x)}{\partial x}, \tag{2.6}$$

$$\mathfrak{f}(t) = \mathcal{F}(t) - \overline{\mathcal{F}}(t) \tag{2.7}$$

in which $\overline{\mathcal{F}}(t)$ is a time averaging. Recall chaotic dynamics are ergodic, so ensemble averaging may be used in this case (second equation above). Dissipations in energies and states are generally irreversible, which will be discussed in the next chapter, but can be related to reversible fluctuations via a Green-Kubo formalism in response theory. This is done by taking the fluctuation autocorrelation

$$\mathcal{C}(\tau) = \overline{\mathfrak{f}(t+\tau)\cdot\mathfrak{f}^*(t)} \to \langle \mathfrak{f}(t+\tau)\cdot\mathfrak{f}^*(t)\rangle \tag{2.8}$$

in which the right hand side holds for ergodic systems only, and * denotes a

complex conjugate. From Weiner-Khinchin theorem, the autocorrelation is the inverse Fourier transform of the power spectrum

$$\tilde{C}(\omega) = \frac{1}{2\pi} \int_{\Re} C(\tau)\, e^{-i\omega\tau}\, d\tau \tag{2.9}$$

The above equation is an important example of a 'fluctuation-dissipation' connection, in that it relates a power (dissipation) on the LHS to a fluctuation on the RHS.

The robustness of autocorrelations and power spectra as signatures of complexity is apparent in Fig. (2.3). In the top left subfigure, an integrable case is shown in which the autocorrelation of a periodic function is periodic itself. This yields a **discrete** power spectrum with peaks at the periodic frequencies. On the other hand, fluctuations in a chaotic Hamiltonian exhibit autocorrelations with finite, nearly constant transient over a *correlation timescale*, τ_c, before rapidly decaying to zero. This yields a **continuous and rugged** power spectrum, seen in the top right subfigure, that is defined over a finite bandwidth $\omega_c = \frac{2\pi}{\tau_c}$. The bandwidth is a *universal* feature, characteristic to all similar chaotic trajectories; however, the rugged structure of the power spectrum is system-specific. It is important to contrast the chaotic system with one that is stochastic (Markovian), as done in the bottom subfigure. Ideal stochastic systems are "delta-correlated", for the autocorrelation $C(\tau) = \delta(\tau)$, and all higher correlations.

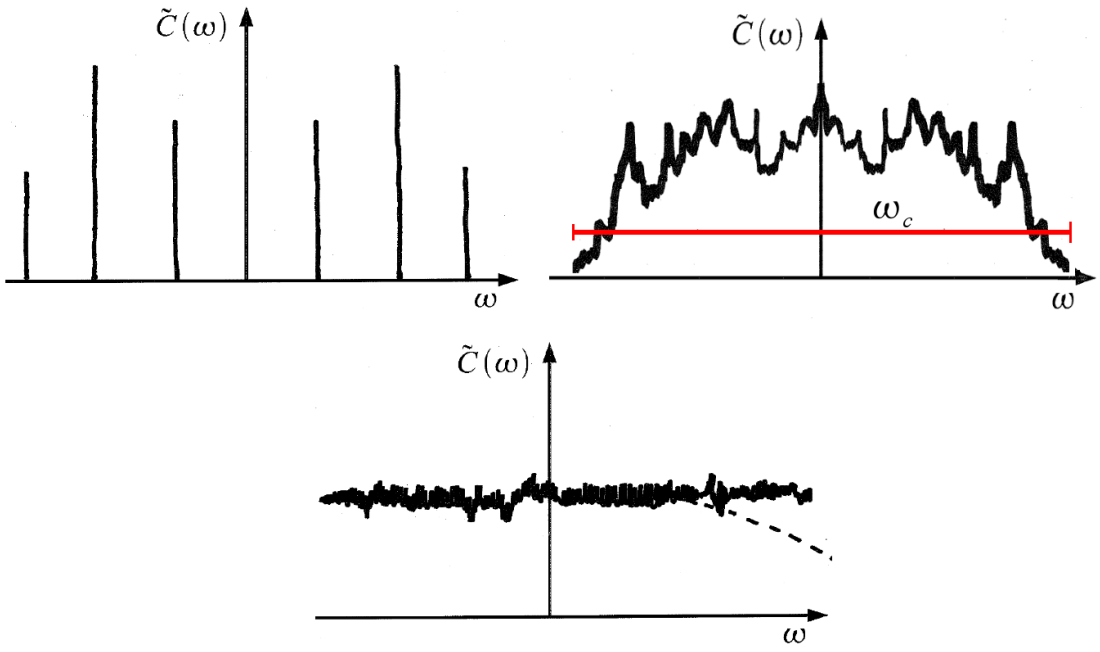

Figure (2.3): Power spectra for systems that are integrable (upper left), chaotic (upper right), and stochastic (bottom). The integrable spectrum is discrete and system-specific. The chaotic spectrum is *rugged* - it is structurally system-specific (where the 'peaks' occur), but universally continuous over a finite bandwidth. The stochastic spectrum is universally flat and generally non-structured. Often 'real' stochastic spectra display a high-frequency roll-off, whose average would follow the dashed line.

This yields a universally flat power spectrum; however, 'real' stochastic systems have a power spectrum with a somewhat universal high frequency attentuation (the $1/f^{\alpha}$ "flicker" phenomenon) [9–11].

As the first example, consider the piston model, presented in Fig. (2.4a). The parameter x controls the position of a large piston within a cavity (and therefore the 'generalized force' is actually the force exerted by the piston), in which also an ensemble of classical particles (gas) is placed. Slow changes in the piston affect

the microcanonical arrangements of the particles, thus also statistically affecting the internal energy of the system - changes to this internal energy can then be thermodynamically seen as the "heating/cooling" of the gas temperature. Another example is a classical charged particle within a chaotic cavity, Fig. (2.4b).

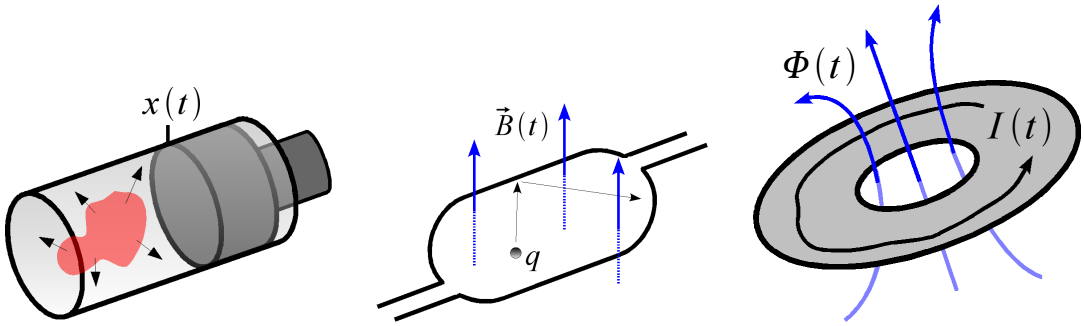

(a) Classical piston model

(b) Metallic particle in external field

(c) Aharonov-Bohm ring topology

Figure (2.4): Three examples of parametric systems. The parameters in these three systems are: piston head position (2.4a), magnitude strength of a magnetic (or electric) field (2.4b), and the magnetic flux strength (2.4c).

The parameter $x(t)$ is a change in an external electric or magnetic field, yielding an electromotive or Lorentz force as the 'generalized force'. The quantum example has an experimental realization using a quantum dot, with the fields applied by gate voltages and currents. Changes in the transport of the particle across the cavity can then be investigated. As a last example, consider charged particles in an Aharonov-Bohm topology, Fig.(2.4c), in which the parameter is the magnetic flux through the ring, $\Phi(t)$. The change of the parameter induces an electromotive force within the ring, $\frac{d\Phi}{dt} = \mathcal{E}$, which starts a closed current, I flowing around the ring. Taking Joule's law, $P = \mathcal{E}I$ and substituting Ohm's law $\mathcal{E} = IR$ yields

$P = \mathcal{E}^2/R$. The conductance fluctuation $(1/R)$ is then directly proportional to the power, i.e. energy dissipation.

2.4 The Quantum Bandprofile and QCC

Weyl quantization is of interest in the question of how complexity manifests in quantum systems. Recall that the classical phase space is continuous. Under first quantization, the uncertainty principle is $\delta q \cdot \delta p \leq \hbar/2$. Weyl quantization is the application of the LHS of the uncertainty principle to phase space - discretizing the phase space into cells with volume $\sim \hbar$. In the tenets of classical chaotic motion, there must be locally divergent trajectories within global mixing. However, Weyl quantization gives a discrete 'phase space' (a finite resolution, so that we can say phase space is 'coarse-grained'), which prevents mixing (must occur at ANY resolution) and destroys local divergence - sensitivity to initial conditions fails, since the initial separations can not be defined smaller than $\hbar$. The tenets of classical chaotic motion fail at the quantum level, so how can one discuss chaos in quantum systems?

For a quantum system, in which $\hat{H} = \hat{H}_0 + \delta x \cdot \hat{\mathcal{F}}$ we can choose to work with basis sets of either $\hat{H}_0$ or $\hat{H}$:

$$\hat{H}_0 \left|\phi_n^0\right\rangle = E_n^0 \left|\phi_n^0\right\rangle, \tag{2.10}$$

$$\hat{H} \left|\phi^m\right\rangle = E_m \left|\phi_m\right\rangle \tag{2.11}$$

In the latter basis, the Hamiltonian becomes $\hat{H} = E_0 + \hat{B}\delta x$ where E_0 is a diagonal matrix of the eigenvalues $\{E_n^0\}$ and $\hat{B}$ is the *quantum perturbation operator*, $B_{nm} = \langle \phi_n^0 | \hat{\mathcal{F}} | \phi_m^0 \rangle$, which can be viewed as the quantum 'fluctuator'. Generalized Shnirelmann theorem states within a semiclassical limit ($\hbar \to 0$), there is an equivalence between the quantum mechanical expectation average and an energy average of a state function in a classical ensemble; thus taking an average of the classical correlation with respect to an energy E_j (denoted by $\langle \cdots \rangle_j$) corresponds to an expectation average of the quantum 'correlation' (see appendix for derivations)

$$\langle \mathcal{C}(\tau) \rangle_j = \sum_k |B_{jk}|^2 e^{i\omega_{jk}^0 t} \tag{2.12}$$

in which $\omega_{jk}^0 = (E_j^0 - E_k^0)/\hbar$. The LHS can be seen as an inverse Fourier transform of the power spectrum, and changing the sum to an integration weighed with the density of states $g(E_k^0)$ yields

$$\frac{\tilde{C}(\omega)}{2\pi\hbar g(E_k^0)} = \left\langle |B_{jk}|^2 \right\rangle_j \tag{2.13}$$

This last equation shows a *quantum-classical correspondence* (QCC) - the statistics of **classical** fluctuations (correlation) are directly related to the variance in a semiclassical limit of a **quantum** perturbation (bandprofile). For chaotic systems, this quantum perturbation bandprofile also exhibits its own finite bandwidth scale of Δ_b. In the case of a QCC, the quantum bandwidth is equivalent with the classical bandwidth, $\Delta_b \sim \omega_c$. In later chapters, we will present this correlation-bandprofile QCC for a specific system, but for now, simply note its importance.

It answers the previous question of how chaos in quantum systems is observed: any chaotic signatures seen in the classical fluctuations (system-specific rugged structures with a universal bandwidth) should also be manifest in the quantum bandprofile.

2.5 Random Matrix Theory

In the last section, we have discussed how one can trace the chaotic dynamics in the quantum realm. Using semiclassical arguments, we show the band-profile of the perturbation operator in the basis of the unperturbed Hamiltonian is proportional to the power spectrum of the classical perturbation. Is there any other place where traces of classical chaotic dynamics can be found? The answer is yes; within the statistical properties of the diagonal elements of the unperturbed Hamiltonian - which in its own basis, is nothing else than the eigenvalues. A powerful mathematical theory has been developed (and widely used) during the past 50 years, which addresses exactly this issue. It goes by the name of *Random Matrix Theory* (RMT), and its foundations were largely masoned by Mehta, Dyson, and Wigner [12]. In the following section, we will discuss some of the predictions from this theory.

2.5.1 Symmetries

RMT first asks 'What is the minimum that we can know about our system?' Suppose I know nothing about the Hamiltonian except: 1) the system is closed, and 2) it is on the quantum scale. For any such quantum system, the evolution is given by the dynamical Schrödinger equation

$$i\hbar\frac{\partial\left|\psi(t)\right\rangle}{\partial t}=\hat{H}\left|\psi(t)\right\rangle \tag{2.14}$$

which yields an evolution operator $\left|\psi(t)\right\rangle=\hat{\mathcal{U}}(t)\left|\psi(0)\right\rangle$, $\hat{\mathcal{U}}(t)=\exp\left(-i\hat{H}t/\hbar\right)$.

Recall classically a conserved constant of motion is one that has a Poisson commutation with the Hamiltonian $\{A_k,H\}=0$. Quantum mechanically, the Poisson commutator becomes $\{A,B\}\overset{\hbar\to0}{\to}i\hbar\left[\hat{A},\hat{B}\right]$ in which $\left[\hat{A},\hat{B}\right]=\hat{A}\hat{B}-\hat{B}\hat{A}$, and therefore quantum mechanically an invariant operation has $\left[\hat{A},\hat{H}\right]=0$, (note this is $\left\{\hat{A},\hat{H}\right\}=\hat{A}\hat{B}+\hat{B}\hat{A}$ for fermionic systems, but throughout the remainder, we will only use bosonic systems). Symmetries therefore really answer the question of the 'minimum information of the system'. But which symmetry in particular?

If we consider the dynamics as a "movie", and then run the "movie" backwards - a process called time-reversal [13] - the relevant terms in the Schrödinger equation behave as $t\to-t$, $i\frac{\partial}{\partial t}\to-i\frac{\partial}{\partial t}$. This corresponds to two operations, respectfully a time operator $\hat{T}f(t)=f(-t)$, and a conjugation operator $\hat{C}f(t)=f^*(t)$. Let us consider the operation of time-reversal then as $\hat{\mathcal{T}}=\hat{C}\hat{T}$, in which *time-reversal*

symmetry is defined as $\left[\hat{\mathcal{T}}, \hat{H}\right] = 0$, but what 'minimum information' about the Hamiltonian does this tell us?

First, we said the system was closed. That means total energy is conserved throughout all time, therefore $\left[\hat{T}, \hat{H}\right] = 0$. It also additionally infers that the probability is normalized, $\langle\psi(t)|\psi(t)\rangle = \langle\psi(0)|\hat{\mathcal{U}}^{\dagger}(t)U(t)\,|\psi(0)\rangle = 1$, giving the unitary evolution $\hat{\mathcal{U}}^{\dagger}\hat{\mathcal{U}} = 1$, which yields a Hamiltonian that is Hermitian, $\hat{H} = \hat{H}^{\dagger}$. Hermitian Hamiltonians are invariant under the evolution operator, and are invariant for any unitary transform, $\hat{\tilde{H}} = \hat{U}\hat{H}\hat{U}^{\dagger}$. What about the remaining time-reversal commutation $\left[\hat{C}, \hat{H}\right] = 0$? Commuting operations have the same basis set, so we can construct a basis so that $\hat{C}\,|\phi_n\rangle = C_n\,|\phi_n\rangle$. Since the operation of $\hat{C}$ is only conjugation, $C_n = \pm 1$, the basis must then be either only all real values $(+1)$, or only all imaginary values (-1). We will select the real values, since imaginary values are the same magnitude, but with a global phase of $\pi/2$. From the Hermiticity, then we find $\hat{H} = \hat{H}^{T}$. This result is a property of *orthogonal invariance* - a rotation in basis (orthogonal transform) given by $\hat{O}$ so that $\hat{\tilde{H}} = \hat{O}\hat{H}\hat{O}^{T}$ gives the same eigenvalues/vectors as $\hat{H}$. Although not used heavily, one last symmetry is of note. If one includes spin interactions in addition to time-reversal, the basis becomes quaternionic, and the Hamiltonians are invariant under symplectic transforms.

As a quick recap, let us look at the 'mimimum' information to construct a Hamiltonian:

- If the system is closed, the Hamiltonian is unitarily invariant.

- If the system is closed, time-reversible, and does NOT have spin interaction, the Hamiltonian is real and orthogonally invariant.
- If the system is closed, time-reversible, and DOES have spin interaction, the Hamiltonian is symplectically invariant.

Other than placing these symmetry stipulations, we are now free to model the Hamiltonian randomly.

Random sequences are built in such a way that their elements follow known distributions. So which distribution is chosen for the Hamiltonian elements? We start with the joint probability of a Hamiltonian elements $p(H_{11}, H_{12}, \ldots, H_{NN})$. The symmetry stipulations are placed on the joint probability - for example, let us consider the orthogonally invariant case. Any function of an orthogonally invariant matrix will depend only on functions of the traces, so $p(H_{11}, H_{12}, \ldots, H_{NN}) = f(\mathrm{Tr}[\hat{H}], \mathrm{Tr}[\hat{H}^2], \ldots)$. Additionally, we want the distribution to be truly "random", that is the elements are uncorrelated such that
$p(H_{11}, H_{12}, \ldots, H_{NN}) = p(H_{11})p(H_{12}) \ldots p(H_{NN})$. The only function that fits this is

$$p(H_{11}, H_{12}, \ldots, H_{NN}) = \gamma \exp(-\beta \mathrm{Tr}[\hat{H}] - \alpha \mathrm{Tr}[\hat{H}^2] \tag{2.15}$$

In the above, the average energy can be shifted to zero by setting $\beta = 0$. Then the above probability is one for a random Gaussian distribution - therefore, the matrix elements for an orthogonally invariant system follow Gaussian statistics. The proportionality constant γ and α in the above probability are found from normalization and by stating the variance of the Gaussian distribution (typically

1), so that

$$\mathrm{var}(H_{nm}) = 1 + \delta_{nm} \tag{2.16}$$

A collection of several random Hamiltonian matrices, all following the symmetry stipulation and with elements Gaussian distributed, is labeled a *Gaussian Orthogonal Ensemble* (GOE). The other symmetry stipulations yield different conditions on the joint probabilities, but they all yield similar Gaussian forms as Eq. (2.15). We will not discuss their derivation, just noting that the unitary invariance yields *Gaussian Unitary Ensembles* (GUE) and symplectic invariance yields *Gaussian Symplectic Ensembles* (GSE).

The number of unique elements in a random matrix, of rank N, can be calculated very easily. For a GOE, there are N unique elements on the diagonal, which leaves $N^2 - N$ off-diagonal elements. From orthogonality, half the elements are the same, so there is a total of $(N^2 - N)/2$ unique off-diagonal elements - totaling $N + (N^2 - N)/2 = \frac{1}{2}N(N+1)$ unique elements. A similar argument can be made for GUE, except now complex-valued elements are allowed, giving $2N^2$ total elements (N^2 real parts, N^2 imaginary parts). The number of unique elements of the real portion of a GUE follow GOE statistics, so same amount of unique elements, leaving $2N^2 - N(N+1)$ off-diagonal terms. The imaginary portion has N^2 terms, but unitary invariance gives no diagonal terms (already accounted for in the real portion) (from unitary invariance) and yields $N^2 - N$ elements in the off-diagonals, of which only half are unique. The total number of unique elements then in a GUE matrix is $\frac{1}{2}N(N+1) + \frac{1}{2}(N^2 - N) = N^2$. A similar argument can be made for GSE

matrices, in which all off-diagonal elements now uniquely contribute "twice", due to spin arrangements. This yields N unique diagonal terms, and $2(N^2-N)$ unique off-diagonal terms, for a total of $N + 2(N^2 - N) = 2N^2 - N$ unique elements. As a last ensemble for consideration, integrable systems have no longer a Gaussian random matrix, for a Hamiltonian, but is in fact the Hamiltonian is diagonal. This yields only N unique elements. Integrable systems are called *Poissonian* - we shall see why in a bit. For the four classes of matrices (Poissonian/GOE/GUE/GSE), the total number of unique elements are easily re-written as

$$\text{Total Unique Elements} = N + \frac{\nu}{2}(N-1) \tag{2.17}$$

where $\nu = 0, 1, 2, 4$ for the respective classes. The value ν is called the *universality index*, and it appears often in the statistics as a way to delineate between the classes.

2.5.2 Density of States

The Hamiltonian acts on the system to give a discrete eigenspectrum $\hat{H}\,|\psi_n\rangle = E_n\,|\psi_n\rangle$. Since it the eigenvalues/eigenbasis of the Hamiltonian that are the 'solutions' for a quantum system, it is the statistics of these quantities, from an RMT approach, that really hold information. As a first step, the joint probability of the eigenenergies of a GOE random matrix can be derived with a Pechukas-Yukawa

formalism as

$$p(E_1, E_2, \ldots, E_N) \sim \prod_{n>m}^{N} (E_n - E_m)^{\nu} \exp\left[-A \sum_n E_n^2\right] \tag{2.18}$$

The above joint energy probability holds all the similar information as the Hamiltonian, and therefore makes a good candidate for use as the statistical distribution. There is a catch though: a 'real-world' Hamiltonian is of infinite rank, and finite Hamiltonians display anamolies near the outer energy band edges - "finite-size effects" This is apparent in another spectral statistic, the average density of states. The density of states, defined as $\rho(E) = \sum_n \delta(E - E_n)$ holds for single RMT matrix. Taking an average over the ensemble yields the averaged density of states, $\langle \rho(E) \rangle$. For all three Gaussian classes, an analytical form of the averaged density of states can be derived with a Green's function approach or supersymmetry. This analytical form is the *Wigner semi-circle law*

$$\langle \rho(E) \rangle = \begin{cases} \sqrt{1 - \left(\frac{\pi E}{2N}\right)^2}; & |E| < \frac{2N}{\pi} \\ 0; & |E| > \frac{2N}{\pi} \end{cases} \tag{2.19}$$

The average density of states is shown in Fig.(2.5). How are "finite-size effects" present here? The statistics that we are interested in are **fluctuations** of eigensolutions around a mean value; for each Hamiltonian, we have $\rho(E) = \langle \rho(E) \rangle + \delta\rho(E)$ where $\delta\rho(E)$ is an fluctuating portion. We wish to hold $\langle \rho(E) \rangle$ at a constant value - which is only true for a small window of energies on the semi-circle, $|E| \leq N$. The solution is to *unfold* the spectra - in short, we map the semi-circle to a straight

line. This is done by taking $\{E_i\} \to \{E_i\} \,/\, \langle\{E_i\}\rangle$. **All spectral statistics from here out are unfolded.**

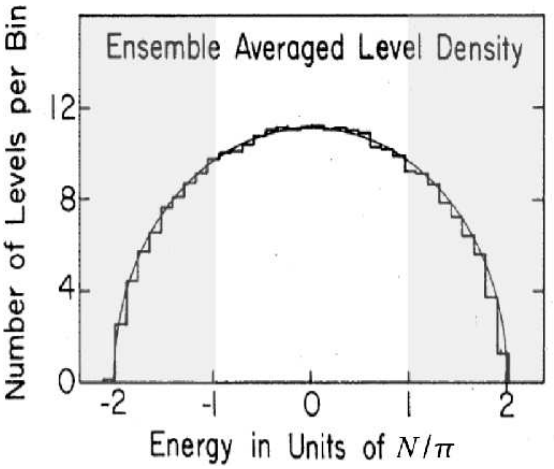

Figure (2.5): Histogram of the average density of states for 50 GOE matrices of $N = 264$. The analytical Wigner semi-circle law, Eq. (2.19) is the smooth solid line. The grey regions denote where finite-size effects begin to occur - where the distribution begins deviating from a nearly constant value of ~ 10. Figure is taken from [14].

2.5.3 Two-point Correlation and Form Factor

How do the differences between the classes manifest themselves in the statistical properties of the energy levels? The density of states certainly does not suffice, since all Gaussian classes follow the Wigner semi-circle law of Eq.(2.19). We must go to a 'next order' in the averaging - and that means correlations! If properly unfolded, the density of states behaves as $\rho(E) = 1 + \delta\rho$. However, the fluctuation is in energy, and therefore the correlator will be energy-dependent [as opposed to the time-dependent form of Eq.(2.8)]. Doing so yields the *spectral autocorrelation function*

$$\mathcal{C}(E) = \langle \delta\rho(E + E')\delta\rho(E - E') \rangle_E \,, \tag{2.20}$$

in which the average is done over E. This can alternatively be written as $\mathcal{C}(E) = \delta(E) + Y_2(E)$, in which $\delta(E)$ is a delta function, and $Y_2(E)$ is the *two-point clustering function*. The differences between the classes now manifest themselves in $Y_2(E)$ - in particular, the 'benchmark' is the Poissonian case, in which the energies are fully uncorrelated. This yields $\mathcal{C}(E) = \delta(E)$, which gives no clustering at all; *i.e.* for a Poissonian case, $Y_2(E) = 0$. However for the Gaussian classes, the two-point clustering varies, as given below and shown in Fig.(2.6)

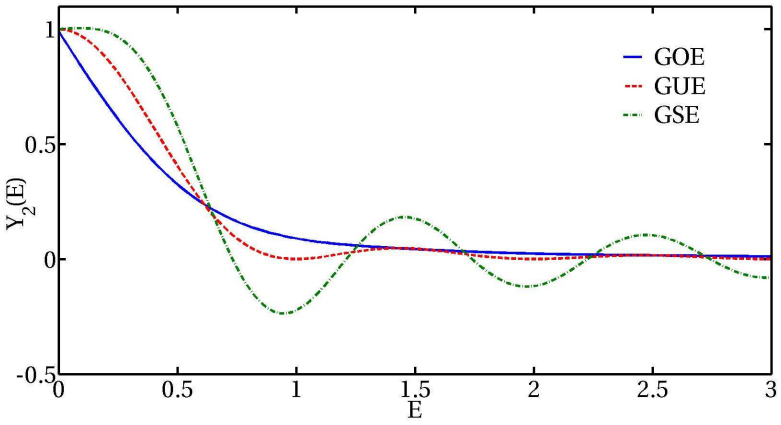

Figure (2.6): Two-point energy density correlation, $Y_2(E)$. The blue solid curve is the GOE case, red dashed curve is the GUE case, and the green dot-dashed curve is the GSE case. Note the strong oscillations in GSE correlation. The 'limiting' case of $Y_2(E) = 0$ is the uncorrelated Poissonian.

$$Y_2(E) = \begin{cases} s^2(E) + \frac{ds(E)}{dE} \int_E^\infty s(E')dE' & \text{GOE} \\ s^2(E), & \text{GUE} \\ s^2(2E) - \frac{ds(2E)}{dE} \int_0^E s(2E')dE' & \text{GSE} \end{cases} \tag{2.21}$$

where $s(E) = \mathrm{sinc}(E) = \sin(\pi E)/\pi E$. Note that $Y_2(E)$ can be obtained [12,15,16] from a second order truncation on the joint probability, Eq.(2.18).

Taking the fourier transform of the above gives the *two-point form factor*, $b_2(t) = \int_{\Re} Y_2(E)\, \exp(-iEt)dE$, shown in Fig.(2.7).

Analytically, integrations give simply $b_2(t) = 0$ for the Poissonian case; however for the Wigner ensembles, we have

$$b_2(t) = \begin{cases} 1 - 2t + t\ln(2t+1), & t \leq 1 \\ -1 + t\ln\frac{2t+1}{2t-1}, & t > 1 \end{cases} \quad \text{GOE} \tag{2.22}$$

$$b_2(t) = \begin{cases} 1 - t, & t \leq 1 \\ 0, & t > 1 \end{cases} \quad \text{GUE} \tag{2.23}$$

$$b_2(t) = \begin{cases} 1 - \frac{t}{2} + \frac{\ln|t-1|}{4}, & t \leq 2 \\ 0, & t > 2 \end{cases} \quad \text{GSE} \tag{2.24}$$

Note the strong singularity at $t = 1$ for GSE, and the cusp for GUE, while the GOE case is relatively smooth. The two-point form factor is a very useful statistic, and is used to define higher-order long-range statistical quantities such as the level variance ($\Sigma^2(L)$) and spectral rigidity ($\Delta_3(L)$). In particular, we will see it again within the linear response theory of Chapter 3.

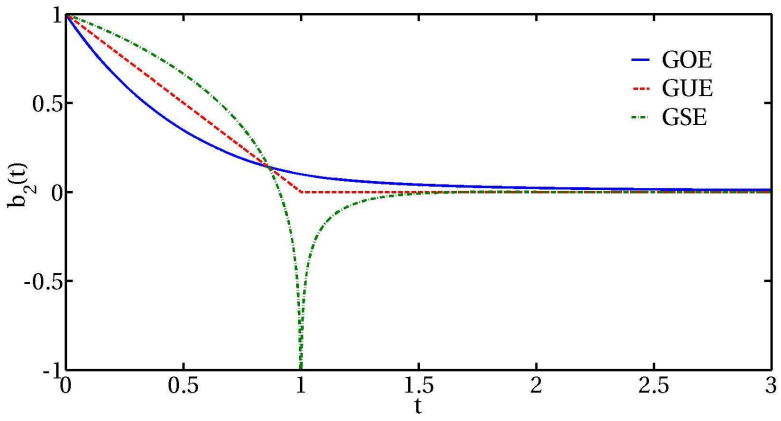

Figure (2.7): Two-point form factor, $b_2(t)$. The blue solid curve is the GOE case, red dashed curve is the GUE case, and the green dot-dashed curve is the GSE case. At $t = 1$, there is a singularity in the GSE case, from the oscillations in Fig.(2.6). There is also a cusp in the GUE case, while the GOE case is smooth. The 'limiting' case of $b_2(t) = 0$ is the uncorrelated Poissonian.

2.5.4 Level Spacing Statistics

We looked at correlations of the energies, which is a way of looking at energy differences across the whole spectrum. What if we just look at short-range behavior, i.e. only neighboring energy levels? Such a statistic is present in the distribution of energy level spacings, which are mathematically defined as $s_n = |E_n - E_{n-1}| / \Delta$ where Δ is the mean level spacing $\Delta = \langle E_n - E_{n-1} \rangle$. For unfolded spectra, $\Delta \sim 1$. The derivation of the level spacing distribution is easily done with a general $2x2$

matrix in a process called *Wigner's surmise*. Taking a GUE $2x2$ matrix

$$\hat{H} = \begin{pmatrix} a+b & f+ig \\ f-ig & a-b \end{pmatrix} \tag{2.25}$$

where a, b, f, g are real elements in a Gaussian distribution, given by $W(a, b, f, g)$. Diagonalizing the above matrix gives the eigenvalues of $a \pm \sqrt{b^2 + f^2 + g^2}$. The level spacing is then just $s = \sqrt{b^2 + f^2 + g^2}$. Calculating the level spacing over the Gaussian element distribution gives

$$P(s) = \int_{\Re} db \int_{\Re} df \int_{\Re} dg\, W(b, f, g)\, \delta(s - \sqrt{b^2 + f^2 + g^2} \tag{2.26}$$

The result of $s^2 = b^2 + f^2 + g^2$ allows a mapping of three variables to a single steradian solid angle, with a Jacobean transform of $db \cdot df \cdot dg \rightarrow 4\pi\pi r^2 dr$

$$\begin{aligned} P(s) &= 4\pi \int_{\Re} dr\; r^2 W(r)\delta(s-r) \\ &= 4\pi \int_{\Re} r^2 \frac{1}{\sqrt{2\pi\sigma}} \exp\left(-\frac{r^2}{2\sigma^2}\right) \delta(s-r) \\ &= \frac{2\pi}{\sigma} s \exp\left(-\frac{s^2}{2\sigma^2}\right) \end{aligned} \tag{2.27}$$

A similar approach can be done for GOE ($g = 0$, solid angle Jacobean goes to simple angle) or for Poissonian (map of $s \rightarrow \sqrt{(r)}$). GSE can also be done similarly, but requires a $4x4$ quaternionic matrix in the Wigner surmise. After normalizing

the probability to unity to get σ, the level spacing distributions are

$$P(s) = \begin{cases} \exp(-s); & \text{Poissonian} \\ \frac{\pi}{2} s \exp\left(-\frac{\pi}{4} s^2\right); & \text{GOE} \\ \frac{32}{\pi^2} s^2 \exp\left(-\frac{4}{\pi} s^2\right); & \text{GUE} \\ \frac{2^{18}}{3^6 \pi^3} s^4 \exp\left(-\frac{64}{9\pi} s^2\right); & \text{GUE} \end{cases} \tag{2.28}$$

The function $P(s) = \exp(-s)$ is the Poissonian distribution function, hence the use of the word "Poissonian" to describe the statistics of integrable systems. The three Gaussian class distributions are collectively called "Wigner distributions". The Wigner distributions (and to some extent the Poissonian) can be seen as $P(s) \sim s^\nu \exp(-s^2)$. This factor of s^ν is important - its effect is to create a 'correlation hole' at $s = 0$ in the spacing distribution - that is integrable energy levels have a tendency to "bunch up" right next to each other (*level clustering*). The energy levels of Gaussian RMT classes are more spread, and do NOT cluster ($P(0) = 0$), a behavior called *level repulsion*). This is shown later on in Fig. (2.8). The presence of clustering/repulsion in the level spacing statistics is another method to characterizing chaotic systems. Further joint probability calculations can be done to create a parametrized version of Eq. (2.28), called the "Brody distribution", in order to study the transition between integrable and chaotic systems. In the Brody distribution, a free parameter q is used and numerical distributions are fit

to the following function

$$P_q(s) = (1+q)\beta s^q \exp\left(-\beta s^{1+q}\right), \tag{2.29}$$

where (2.30)

$$\beta = \Gamma^{2+q}\left(\frac{2+q}{1+q}\right)$$

in which Γ is the Gamma function. For $q = 0$, the Brody distribution becomes Poissonian, and for $q = 1$ the distribution becomes Wignerian (GOE).

The level-spacing distribution is interesting in that it provides strong evidence for proof of the *Bohigas-Giannoni-Schmit (BGS) conjecture*. From the original text [17]

> *Spectra of time-reversal invariant systems whose classical analogs are K systems show the same fluctuation properties as predicted by GOE... If the conjecture happens to be true, it will then have been established the* ***universality of the laws of level fluctuations*** *in quantal spectra...*

The powerful sentiment within the BGS conjecture is that quantum systems that can be taken to a semiclassical limit whose classical phase space is fully ergodic (no integrable islands), have the SAME behavior in energy fluctuations as a quantum random matrix model. The power is that ANY chaotic system (time-reversable), whether classical or quantum and regardless of small system differences, statistically have the same fluctuation behavior as an 'artifical' RMT matrix - this is the

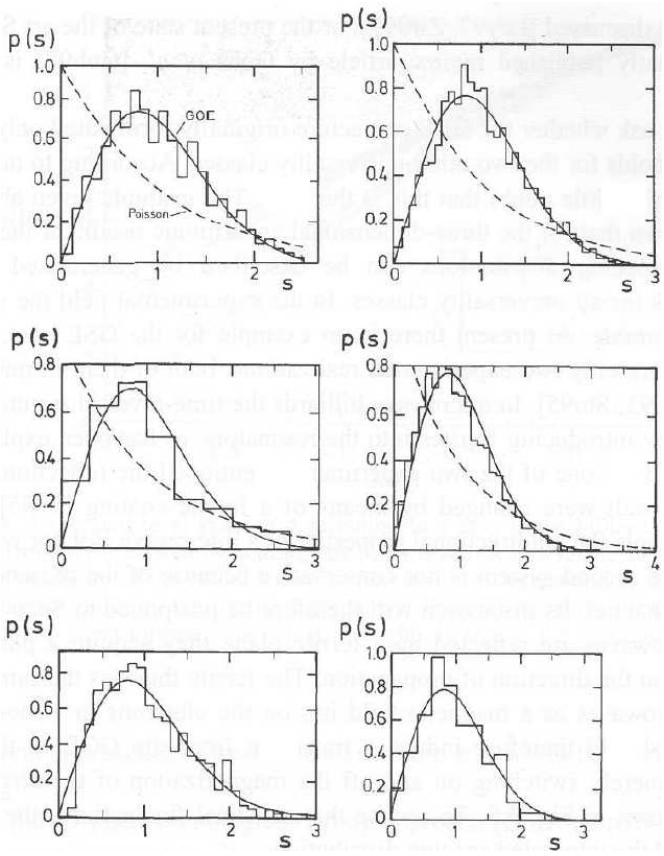

Figure (2.8): Level-spacing distributions for six different systems. Clockwise from the upper left: quantum Sinai billard, hydrogen atom in a strong magnetic field, NO_2 excitations, acoustic resonance of an irregularly-shaped quartz bulk, microwaves in a chaotic cavity, vibrations of a quarter-stadium plate. The last three systems are specifically classical. All six systems show distributions that follow Wigner distributions (black line), as opposed to Poissonian distributions (dashed line), providing evidence for the BGS conjecture. The 'correlation hole' can be seen at $s = 0$, in which $P(s) = 0$ for chaotic systems. The figure is from [15].

idea of *universality*. Fig. (2.8) illustrates this sentiment. The level-spacing distribution is shown for six different experimental systems - three that are quantum and three that are wholly classical. For all six systems, a universal behavior that matches the theory in Eq. (2.28) is observed. It should be noted that there are several other experimental systems in GOE that lend strong support to the BGS conjecture; however, only two experiments have been shown for GUE, and there are currently no such experiments for GSE systems [15].

2.5.5 Wavefunction Statistics

Another statistic is the eigenvector component distribution. While not heavily used, it often serves as another 'check' that a system is chaotic. For an eigenvector $|\psi\rangle = (\psi_1, \psi_2, \ldots, \psi_N)$, the distribution follows

$$P(y = |\psi_i|^2) = \begin{cases} \frac{1}{\sqrt{\pi}} \frac{\Gamma(N/2)}{\Gamma((N-1)/2)} \frac{(1-y)^{(N-3)/2}}{\sqrt{y}}; & \text{GOE} \\ (N-1)(1-y)^{N-2}; & \text{GUE} \\ (N-1)(N-2)y(1-y)^{N-3}; & \text{GSE} \end{cases} \tag{2.31}$$

Note that the eigenvalues (hence the distribution) have an N dependence, in that a chaotic eigenvalue on average is $1/N$. In a thermodynamic limit $N \to \infty$, the above distributions become

$$P(\eta) = \begin{cases} \frac{\exp(-\eta/2)}{\sqrt{2\pi\eta}}; & \text{GOE} \\ \exp(-\eta); & \text{GUE} \\ \eta \exp(\eta); & \text{GSE} \end{cases} \tag{2.32}$$

in which $\eta = Ny$. The GOE case is called the *Porter-Thomas distribution*, shown in Fig.(2.9).. Just as was seen in Fig. (2.8), the distributions of the eigenvector components should also behave universally, in accordance with the BGS conjecture.

GOE/GUE/GSE are not the limitation of RMT. Variations in the matrix construction, say by restricting off-diagonals to some bandwidth or engineering a

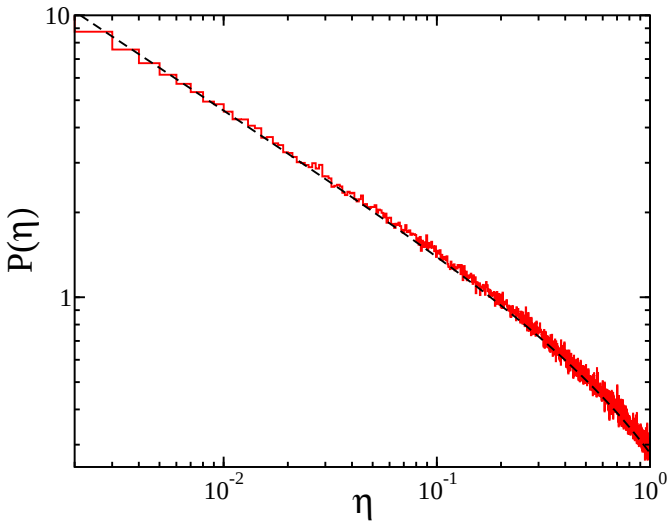

Figure (2.9): Eigenfunction component distribution for GOE matrices, $N = 1000$. The parameter $\eta = N\,|\psi_i|^2$ is the scaled wavefunction value. The red histogram shows the actual distribution, while the black dashed line shows the Porter-Thomas distribution from Eq.(2.32).

function in the variance, have been used to study various phenomena. In particular, in Chapters 5-6, these 'engineered' RMT ensembles are used to model the phenomena of Anderson localization and its critical transition. Further discussion on these alternative RMT ensembles will be savored in their respective chapters.

2.6 The Take-Home Message

We have discussed how complex systems classically evolve in time, and how their chaotic nature is shown in phase space. The definition of a "chaotic system" was given as local trajectory divergences and global mixing. Parametric systems were introduced to motivate a fluctuating quantity whose correlation spectra display strong differences between integrable, chaotic, and stochastic behavior. This power spectrum is reflected via a quantum-classical correspondence in the band-

profile structure of the quantum perturbation operator. Another point where chaoticity is encoded in the quantum realm is on the statistical properties of the eigenvalues of the unperturbed Hamiltonian. These properties are described by a powerful mathematical theory called Random Matrix Theory, whose basic predictions where presented at the end of the chapter. Gaussian random matrices were given by the BGS conjecture as a way to model the Hamiltonian of complex systems. Finally, universality within the different symmetry classes provides another signature of chaos. These concepts form the foundation to quantifying and modeling chaotic systems, and will be used throughout the remainder of this work.

Chapter 3

Fidelity: A Measure of Stability

'Twas whispered in Heaven, 'twas muttered in hell, and echo caught faintly the sound as it fell.

-Catherine M. Fanshawe, Enigma (The Letter H)

3.1 A Historical Introduction

3.1.1 Irreversibility

In thermodynamics, the idea of *irreversibility* was first introduced in the following manner. Consider a process within a system, which may or may not be cyclic. The process is called *reversible* if upon reversing the process, there is no change to either the system itself, or its surrounding environment. The system change

was quantified by Boltzmann's H-theorem using the Gibbs entropy

$$S = -k \sum_n p_n \log p_n, \tag{3.1}$$

where p_n is a given microstate probability. After reversing the process, this gives an entropic change of

$$\Delta S = 0 \quad \text{reversible systems},$$
$$\Delta S > 0 \quad \text{irreversible systems}$$

According to Boltzmann, irreversible processes are then certainly possible thermodynamically. However, Boltzmann's close friend Loschmidt drew attention to the fact the laws of classical mechanics (i.e. the HEOM in the previous chapter) are time symmetric, and therefore ALL molecular processes must be reversible within statistical mechanics.

This may be seen in the following *gendenken* experiment, illustrated in Fig. (3.1). Suppose that you are sitting in a bar with a tepid drink, into which you place a large ice cube. As the ice-water system evolves in time, the ice cube lattice 'melts', and the water molecules immediately begin to blend with the warmer drink molecules (alcohol, sugar, more water, etc.) until a thermal equilibrium is reached, upper panel of Fig. (3.1). Classically the interactions between the ice/drink molecules are complex, as to give trajectories that are *mixing* (as described in the previous chapter). Within the ice-drink example, V_2 is a phase

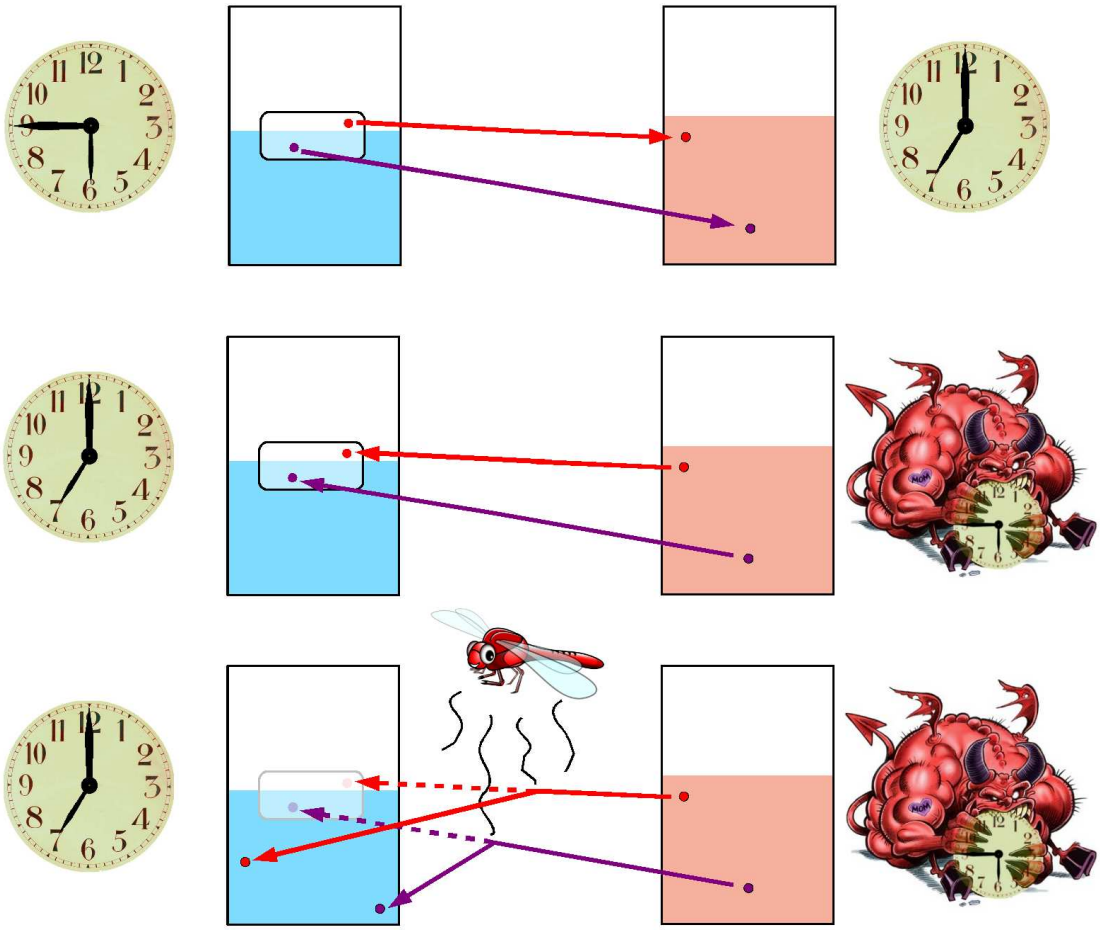

Figure (3.1): In the upper panel, an initial state of an ice-cube in a tepid liquid melts into a thermal equilibrium. The trajectories of two ice molecules are schematically represented by the two colored arrows. In the middle panel, the Loschmidt demon reverses the arrow of time, effectively reversing the direction of the trajectories. Time-reversal symmetry states we should be able to recover the ice cube. However, the mixing of trajectories and coarse graining in the Loschmidt demon manifest as small fluctuations in the environment, beyond the control of the Loschmidt demon. These environmental fluctuations (illustrated by thermal fluctuations created by the dragonfly's wings in the lower panel) perturb the trajectories, making the system irreversible.

volume in the final warm equilibrium mixture, and V_1 is a phase volume of the initial cold ice & drink. Note that within the figure, we are only considering the ice molecules within V_1. Since the dynamics are time-reversible, we see an ice cube re-emerge from the warm drink. Since most initial preparations of ice will melt into equilibrium within a finite time, the probability of finding the system in such a state is relatively large, so that it's fractional volume (i.e. probability) is $f_2(t) \sim 1$. Loschmidt introduced a "demon" - a theoretical 'device' external to the system that would be able to reverse the process by reversing the direction of time (Loschmidt's "arrow of time"). The mixed equilibrium mixture becomes the initial state, and the role of the Loschmidt demon is to just reverse the final velocities, middle panel of Fig. (3.1), so that the trajectories will retrace and an ice cube will re-emerge from the mixed equilibrium. Initial states go to final states, and final states go to initial states. However, thermodynamics state otherwise, and experience certainly supports this - no bar in the world has seen an ice cube emerge from a warm drink. We now have a nice contradiction - the *Loschmidt paradox* [18]. So what gives?

The answer rests in the Loschmidt demon. The cube-ice preparation occupies a very exact, small volume in phase space, and its final equilibrium state occupies a very contorted phase volume with very fine structures (from mixing). In order for the reversal process to occur, we must prepare an initial state that matches the finely structured equilibrium phase volume, taking into account both the system and environment, capturing all the correlations between the molecules. To adequately reproduce the fine structure of the warm equilibrium would require

a very fine resolution in our preparation instruments[†] - such a resolution simply does not exist in our current technology. This roughness in our ability to make a preparation is termed *coarse graining*. It is the flaw of coarse graining within the Loschmidt demon coupled with classical mixing that is responsible for 'irreversibility' within systems, and resolves the Loschmidt paradox.

What about in the quantum realm? Weyl quantization limits our resolution scales to $\hbar$, so we are unable to capture the fine structures associated with classical mixing. Coarse-graining also conceptually fails in the quantum realm, since it is theoretically possible to create pure, exact quantum states. Since the evolution of such states is unitary, the uncertainty from instrumental-coarse graining will not grow, and therefore can not be observed. How can we then probe the irreversibility of the system?

Peres [19] made the supposition that we can produce an exact initial state, either quantum mechanically or classically. He placed the role of coarse-graining into the environment - in our working example, suppose we could control the ice and drink mixture to infinite precision, but not the rest of the bar. The environmental portion of the Hamiltonian could then be said to be 'unknown', since we can not control all the parameters of the environment. The Hamiltonian can then be modeled parametrically, Eq. (2.5), in which the environment plays a perturbative role in $\mathcal{F}(q,p)$ (or $\hat{B}$ in the quantum basis of $\hat{H}_0$), and whose unknown behavior

[†]For the ongoing ice-cube/drink example, we have a fairly open system, so a Loschmidt demon also must be able to control all the molecules in the surrounding environment, including the air molecules in the bar, the molecules in surrounding patrons, molecules in said patrons' drinks, exhaust molecules of cars passing, and so on ad infinitum.

can be modeled with random matrix theory. Referring to the ongoing *gedenken*, suppose a dragonfly drifts into the neighborhood of our drink as soon as our Loschmidt demon reverses the velocities - its flight creating thermal fluctuations that transport across the glass interface into our drink and perturbing them from tracing their trajectories back to the initial state, as illustrated in the lower panel of Fig. (3.1). The system's sensitivity to these fluctuations in the uncontrollable environment is then responsible for the irreversibility of the system, but again back to the original question: How to probe the irreversibility of the system?

3.1.2 The Loschmidt Echo & Fidelity

Probing the irreversibility of the system begs the question: 'How close did I get to obtaining my initial state of an ice-cube?'[†] This naturally leads to Peres' idea of using state *overlaps* to define a measure of the stability of a system to external perturbations. Suppose that there are two Hamiltonians, which read

$$\begin{aligned} \hat{H}_{1,2} &= \hat{H}_0 \pm x\hat{B}, \\ H_{1,2} &= H_0 \pm xB \end{aligned} \tag{3.2}$$

where the top line is the quantum mechanical Hamiltonian, and the second line is the classical Hamiltonian. $\hat{H}_0$ (or H_0) describes the evolution of the system (ice and drink) only, and $\hat{B}$ (classically B) describes a parametric coupling of

[†]If one were to create an imperfect, yet marketable, device that acts as the Loschmidt demon, it would be more suitable to beg the question 'What is the efficiency of my device?'

the system to its environment (dragonfly and bar). Both Hamiltonians are assumed to be classically small, and $\hat{H}_1$ (classically H_1) then denotes the forward evolution of the system & environment before the Loschmidt demon is turned on and $\hat{H}_2$ (classically H_2) describes the time-reversed evolution of the system & environment. It is often the case that the evolutions are defined so that the backward evolution is the only term involving the environment. In this case, we have $\hat{H}_1 = \hat{H}_0, \hat{H}_2 = \hat{H}_0 + x\hat{B}$, but we shall leave the evolutions in the general symmetric form of Eqs. (3.2). Evolving a generic initial state, $|\psi_0\rangle$, forward in time and then performing the Loschmidt time-reversal yields an evolved state of

$$|\psi_{12}(t)\rangle = \hat{U}_2^\dagger(t)\hat{U}_1(t)\,|\psi_0\rangle\,, \tag{3.3}$$

$$= \exp(-i\hat{H}_2^\dagger t/\hbar)\exp(i\hat{H}_1 t/\hbar)\,|\psi_0\rangle \tag{3.4}$$

The *Loschmidt Echo* is then the overlap probability of the initial state with the forward/time-reversed state

$$F_{\rm LE}(t) = \left|\langle\psi_0|\exp(-i\hat{H}_2^\dagger t/\hbar)\exp(i\hat{H}_1 t/\hbar)\,|\psi_0\rangle\right|^2 \tag{3.5}$$

This can been seen graphically in Fig. (3.2), where the system is a 'Lorentz gas' - an arrangement of hard spheres [20]. The initial state is either a quantum Gaussian wavepacket, or a Gaussian phase distribution of initial states in a classical space, presented in green on the upper left. The evolution with $\hat{H}_1$ (or H_1) yields the evolved wave seen in the upper left. Note that for the Lorentz gas system, the

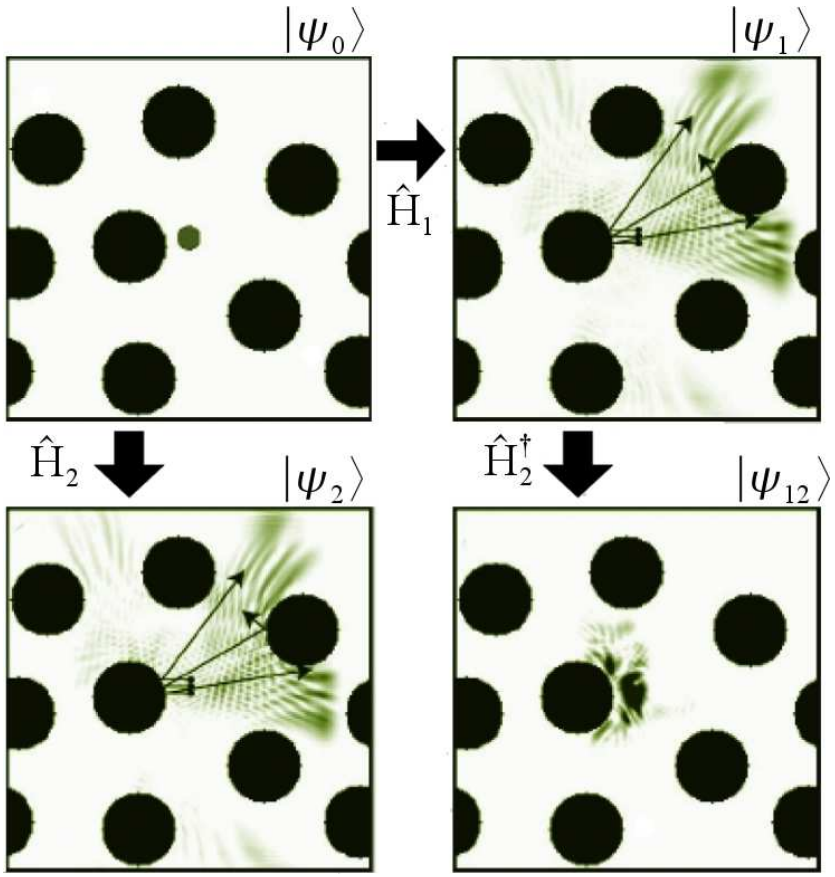

Figure (3.2): The Loschmidt echo and fidelity in a Lorentz gas environment. An initial quantum wavepacket (or an initial phase space distribution of classical states) is represented by the green area in the upper right figure. Both the Loschmidt echo and the fidelity evolves the state forward under the Hamiltonian $\hat{H}_1$ (H_1) to an evolved wavepacket shown in the upper left (the arrows denote possible trajectories the classical ensemble of states may take). The Loschmidt echo then evolves the state in the upper left under a time-reversed Hamiltonian, $\hat{H}_2^\dagger$, to the state shown in the lower right. The Loschmidt echo is then defined as the overlap between the initial state in the upper left and the forward/backward evolved state in the lower right. The fidelity takes the same initial state, in the upper left, and evolves it under a forward evolution of $\hat{H}_2$, to the state shown in the lower right. The fidelity is then defined as the overlap between the two forward evolved states shown in the upper right/lower left. Even though the wavefunction evolves into different forms under the evolutions, because the evolutions are unitary, the overlaps (Loschmidt echo and fidelity) give equivalent measures. Figure taken from [20].

Hamiltonian is just a free propagation† with specular reflection at the spherical scatterer and cavity boundaries. Classically, the trajectories move in position as shown by the arrows. The system is then perturbed, where the perturbation x is a shift in the mass distribution so that

$$p_x^2 \to \frac{x}{1+x} p_x^2, \quad p_y^2 \to x p_y^2 \tag{3.6}$$

and the backward evolution is performed, with $\hat{H}_2$ (or H_2) being a free propagation with the above perturbed momenta. The resulting state is shown in the lower right, and the Loschmidt echo is just the overlap between the upper left and lower right wavefunctions.

The measure of Eq.(3.5) could also be viewed in the following manner. Rather than evolving an initial state forward, and then reversing the velocities, it is perhaps more experimentally viable to create two identical initial states, and then evolve them forward under the two Hamiltonians, $\hat{H}_{1,2}$, without any time-reversing occurring; however, the Hamiltonians still maintain a time-symmetry. This yields two evolved states: $|\psi_1(t)\rangle$ is the forward evolution with $\hat{H}_1$ and $|\psi_2(t)\rangle$ is the forward evolution of $\hat{H}_2$. We then look at the overlap probability of the two forward evolved states, labeled *fidelity*

$$\begin{aligned} F_{\rm f}(t) = |\langle\psi_1(t)|\psi_2(t)\rangle|^2 &= \left|\left[\langle\psi_0|\exp(-i\hat{H}_2^\dagger t/\hbar)\right]\cdot\left[\exp(i\hat{H}_1 t/\hbar)\,|\psi_0\rangle\right]\right|^2 \\ &= F_{\rm LE}(t) \end{aligned} \tag{3.7}$$

†Just a reminder: "Free Propagation" is $|\vec{p}|^2/2m$ or quantum mechanically $\vec{p} \to -i\hbar\bigtriangledown$.

This is seen graphically in Fig. (3.2) as well, in which the forward evolution under $\hat{H}_1$ proceeds to the upper right, as previously mentioned. However, the *forward* evolution under $\hat{H}_1$ yields a state shown in the lower left. The fidelity is then the overlap between the lower left and upper right wavefunctions (in contrast to the fidelity). Even though the wavefunctions are different under each evolution, the *fidelity and the Loschmidt echo are equivalent* under unitary evolutions, $F_{\mathrm{LE}}(t) = F_{\mathrm{f}}(t)$.

Since the fidelity is defined via overlaps of states, it therefore can also be defined classically as

$$F_{\mathrm{f}}^{\mathrm{cl}}(t) = \left| \int_{\Omega} dq\, dp\ \varrho_1(q,p;t)\varrho_2(q,p;t) \right|^2 \tag{3.8}$$

where $\varrho_{1,2}$ are the phase space distributions (ie. classical states) for an ensemble of initial trajectories evolved under the classical Hamiltonians $H_{1,2}$. Just as in the quantum case, a classical Loschmidt echo can also be defined as

$$F_{\mathrm{LE}}^{\mathrm{cl}}(t) = \left| \int_{\Omega} dq\, dp\ \varrho_0(q,p;t)\varrho_{12}(q,p;t) \right|^2 \tag{3.9}$$

in which ϱ_0 is the phase space distribution for an ensemble evolved under H_0, and ϱ_{12} is the phase space distribution for an ensemble evolved forward under H_1 and then time-reversed under H_2. The dynamics of the classical operations are also unitary (HEOM), and therefore fidelity and Loschmidt echo are also equivalent in the classical case. From this equivalence, we shall henceforth stop distinguishing between the two and will simply call the measure 'fidelity', denoted by $F(t)$ (or $F_{\mathrm{cl}}(t)$ in the classical case) throughout the remainder of this work.

The fidelity gives us a measure of the stability/irreversibility of the initial wavefunction under environmental fluctuations - for $t = 0$, the fidelity equals unity, and for irreversible systems, has a decay from unity as time is evolved. This decay behavior has a dependence on the strength of the environmental coupling, presented as the parameter x. We shall now go on to discuss the behavior of the fidelity decay and its dependence on x.

3.2 Linear Response Theory

We want now to evaluate the temporal decay of fidelity given by Eq.(3.7). To this end, we rely on time-dependent perturbation theory. The technical details[†] are compiled within Appendix B.2 and give an approximation for the evolution operator. This operator applied to the two forward evolutions with Hamiltonians $H_1, 2$ read

$$\left|\psi_1^D(t)\right\rangle \simeq |\psi_0\rangle + \frac{ix}{\hbar}\int_0^t d\tau\, \hat{B}(\tau)\,|\psi_0\rangle - \left(\frac{x}{\hbar}\right)^2 \int_0^t d\tau \int_0^\tau d\tau' \hat{B}(\tau)\hat{B}(\tau')\,|\psi_0\rangle$$
$$\left|\psi_2^D(t)\right\rangle \simeq |\psi_0\rangle - \frac{ix}{\hbar}\int_0^t d\tau\, \hat{B}(\tau)\,|\psi_0\rangle - \left(\frac{x}{\hbar}\right)^2 \int_0^t d\tau \int_0^\tau d\tau' \hat{B}(\tau)\hat{B}(\tau')\,|\psi_0\rangle$$

where the superindex D indicates that we operate in the Dirac (interaction) picture (see Appendix B.2) and we have assumed that $\left|\psi_1^D(0)\right\rangle = \left|\psi_2^D(0)\right\rangle = |\psi_0\rangle$.

[†]A large part of this section's derivations come directly from Ref. [21].

Expanding the fidelity

$$\begin{aligned} F(t) &= |\langle\psi_2(t)|\psi_1(t)\rangle|^2 \\ &= \left|\left\langle\psi_2^D(t)\right| \exp(i\hat{H}_0 t/\hbar)\exp(-i\hat{H}_0 t/\hbar)\left|\psi_1^D(t)\right\rangle\right|^2 \\ &\simeq \left| \left(\langle\psi_0| - \langle\psi_0|\frac{ix}{\hbar}\int_0^t d\tau\hat{B}(\tau) - \langle\psi_0|\left(\frac{x}{\hbar}\right)^2\int_0^t d\tau\int_0^\tau d\tau'\,\hat{B}(\tau)\hat{B}(\tau')\right)\times \right. \\ &\quad \left.\left(|\psi_0\rangle + \frac{ix}{\hbar}\int_0^t d\tau\hat{B}(\tau)\,|\psi_0\rangle - \left(\frac{x}{\hbar}\right)^2\int_0^t d\tau\int_0^\tau d\tau'\,\hat{B}(\tau)\hat{B}(\tau')\,|\psi_0\rangle\right)\right|^2 \end{aligned}$$

Truncating the cross-terms to second-order yields

$$\begin{aligned} &\simeq \left|1 + \frac{2ix}{\hbar}\int_0^t d\tau\langle\hat{B}(\tau)\rangle_0 - 2\left(\frac{x}{\hbar}\right)^2\int_0^t d\tau\int_0^\tau d\tau'\,\langle\hat{B}(\tau)\hat{B}(\tau')\rangle_0 - \right. \\ &\qquad \left.\left(\frac{x}{\hbar}\right)^2\int_0^t d\tau\langle\hat{B}^2(\tau)\rangle_0\right|^2 \\ &\simeq 1 - 4\left(\frac{x}{\hbar}\right)^2\int_0^t d\tau\int_0^\tau d\tau'\,\langle\hat{B}(\tau)\hat{B}(\tau')\rangle_0 - 2\left(\frac{x}{\hbar}\right)^2\int_0^t d\tau\langle\hat{B}^2(\tau)\rangle_0 + \\ &\qquad 4\left(\frac{x}{\hbar}\right)^2\int_0^t d\tau\langle\hat{B}(\tau)\rangle_0^2 \end{aligned} \tag{3.10}$$

where $\langle\cdots\rangle_0 = \langle\psi_0|\cdots|\psi_0\rangle$. A further simplification can be done to the above expression if we recognize that

$$\mathcal{C}(\tau,\tau') = \langle\hat{B}(\tau)\hat{B}(\tau')\rangle_0 - \langle\hat{B}(\tau)\rangle_0\langle\hat{B}(\tau')\rangle_0 \tag{3.11}$$

where $\mathcal{C}(\tau,\tau')$ is the same correlator defined by Eq. (2.8). Therefore the fidelity can be re-written as

$$\begin{aligned} F(t) &\simeq 1-\left(\frac{2x}{\hbar}\right)^2\int_0^t d\tau\int_0^\tau d\tau'\,\mathcal{C}(\tau,\tau')+\ldots \\ &\approx \exp\left[-\left(\frac{2x}{\hbar}\right)^2\int_0^t d\tau\int_0^\tau d\tau'\,\mathcal{C}(\tau,\tau')\right] \end{aligned} \tag{3.12}$$

where in the second line we have assumed the infinite order series converges to an exponential. The correlator appearing on the right hand side of this equality encodes the fluctuating properties of the generalized force, while the fidelity in this framework can be seen as a loss (dissipation) of information.

One last important observation needs mentioned. From the linear response theory of fidelity (LRT), Eq. (3.12), a difference can be directly seen between integrable and chaotic systems. Recall in the previous chapter the discussion about the properties of the correlator - the more chaotic a system is, the faster its correlation decay, especially in comparison to an integrable system. Naively, one would expect that an integrable system will dissipate information slower than a chaotic one. The result of Eq.(3.12) indicates exactly the opposite - namely, chaos supresses the loss of information, *i.e.* leads to a slower fidelity decay. This result can be of great importance for quantum information processing.

3.2.1 Linear Response and Correlation Dynamics

It is obvious that the validity of the previous calculations are associated with the strength of the perturbation, x. In this section we will expand on these conditions and evaluate the integral appearing in Eq.(3.12) for various perturbation strengths, assuming generic behavior (for a case of chaotic systems) for the correlator $\mathcal{C}(\tau, \tau')$.

Wigner (FGR) Regime

We will assume hereafter that correlation $\mathcal{C}(\tau, \tau')$ is homogeneous in time[†], so that $\mathcal{C}(\tau, \tau') = \mathcal{C}(\tau - \tau')$. Under a substitution $\alpha = \tau - \tau'$ the first integration in Eq.(3.10) over τ' is performed, resulting in

$$F(t) \simeq 1 - \left(\frac{2x}{\hbar}\right)^2 \int_0^t d\tau (t-\tau)\mathcal{C}(\tau) \tag{3.13}$$

Correlations decay over a timescale, t_c (see Section 2.3 in Chapter 2). In chaotic systems, the correlation decay is very fast, so that after integration, the second term above is negligible. Furthermore, we assume that the correlation is considerably different from zero only for $t < t_c$. This yields

$$F(t) \simeq 1 - \left(\frac{2x}{\hbar}\right)^2 t \int_0^{t_c} d\tau \mathcal{C}(\tau) \tag{3.14}$$

[†]Correlations that are homogeneous in time are related to stationary processes.

At times $t > t_c$, the correlation fluctuates around zero, so that the integration can be extended for all times. This integration results in the *Green-Kubo linear transport coefficient*

$$\sigma = \int_0^\infty d\tau \mathcal{C}(\tau) \tag{3.15}$$

Assuming again an infinite order re-summation, one gets

$$F(t) \simeq 1 - \left(\frac{2x}{\hbar}\right)^2 \sigma t \approx \exp(-\gamma_e t) \tag{3.16}$$

The fidelity for $t > t_c$ in a complex system behaves **exponentially**, with a decay rate of

$$\gamma_e = \frac{4\sigma x^2}{\hbar^2} \tag{3.17}$$

Fidelity exhibiting this exponential decay is said to be in the *Wigner (FGR) Regime.*

Standard Perturbative Regime

In the above discussion, we stated the correlation function $\mathcal{C}(t)$ fluctuates around zero for $t > t_c$ and converges to the transport coefficient σ. However for systems in a finite Hilbert space, the correlation function does NOT asymptotically decay to zero, but rather reaches a finite value $\overline{C}$, similar to the asymptotic value of fidelity[†]. Our task is to calculate the value of this small, yet finite, plateau -

[†]Asymptotic behavior of fidelity decay is discussed in greater detail within Chapter 7, but generally $F(t \to \infty) \sim N^{-d}$, where N^d is the volume of the Hilbert space.

which is the time-averaged correlation function

$$\overline{C} = \lim_{t\to\infty} \frac{1}{t^2} \int_0^t d\tau \int_0^{\tau'} d\tau' \; \mathcal{C}(\tau, \tau') \tag{3.18}$$

The system we are considering is chaotic, so we will make a conjecture - suppose the diagonal elements are members of a Gaussian random sequence. We can use the quantum-classical correspondence, Eq. (2.13), to relate the variance in the diagonal elements to the center of a classical power spectrum. The power spectrum must include a factor of $\frac{1}{2}$ to account for the Gaussian diagonal variance seen in Eq.(2.16), and also needs to be normalized by a factor of N, since the system is finite. The center value of the classical power spectrum is, in fact, a classical version of the transport coefficent of Eq.(3.15)

$$\sigma_{cl} = \int_0^\infty d\tau \mathcal{C}(\tau) \exp(-i\omega\tau)|_{\omega=0} = \frac{1}{2N}\tilde{C}(\omega = 0) \tag{3.19}$$

The plateau value of $\overline{C}$ is reached at $t \sim t_H$, where t_H is the dimensionless Heisenberg time, $t_H = N/2$. Then for $t \geq t_H$, the correlation in Eq.(3.12) is equivalent to the plateau value of Eq.(3.18) giving

$$2\sigma_{cl} t_H \approx \overline{C} t_H^2 \tag{3.20}$$

The finite value of the plateau is then simply

$$\overline{C} \approx \frac{4\sigma_{cl}}{N} \tag{3.21}$$

Substituting this back into Eq. (3.12) gives the fidelity

$$\begin{aligned} F(t) &\simeq 1 - \left(\frac{2x}{\hbar}\right)^2 \frac{4\sigma_{cl}}{N} t^2 \\ &\approx \exp(-[\gamma_g t]^2) \end{aligned} \tag{3.22}$$

The fidelity behaves in a **Gaussian** fashion, with a decay rate of

$$\gamma_g = \frac{4x}{\hbar}\sqrt{\frac{\sigma_{cl}}{N}} \tag{3.23}$$

Note that in order to see this Gaussian decay before the Heisenberg time, the decay rate must be very slow - x must be very small. Otherwise, we would only see an exponential decay before a saturation to the finite plateau at $t \sim t_H$. We will refer to this regime where the fidelity decay is Gaussian as the *standard perturbative regime*.

Validity of the Linear Response

Rather than characterize the two regimes with the timescales (t_c, t_H) let us characterize the borders through the perturbation strength. The standard perturbative regime occurs when the time reaches t_H, so that equating the decay rate of γ_g with this time gives the characteristic perturbation strength x_c

$$\gamma_g \sim t_H^{-1} \longrightarrow x_c \sim \frac{\hbar}{2}\sqrt{\frac{1}{\sigma N}} \tag{3.24}$$

This gives us a threshold for the exponential/Gaussian decays: for $x < x_c$, the linear response follows Eq. (3.22). For $x > x_c$ the linear response follows Eq.(3.16).

However, there is a limit to linear response - its limitation can be evaluated by equating the rate γ_e^{-1} with the classical correlation time t_c. The outcome of this gives

$$x_{prt} \sim x_c \sqrt{\frac{\Delta_b}{\Delta}} \tag{3.25}$$

Once $x > x_{prt}$, the perturbative approach of linear response fails to adequately describe the fidelity, such an x is said to be in the *nonperturbative regime*. In order to get an approximation of the fidelity decay, semiclassical methods must be used, so this regime often goes by the alias of the *semiclassical regime*. Under such semiclassical considerations, the fidelity has been shown to decay exponentially, as

$$F(t) \sim \exp\left(-\Lambda t\right) \tag{3.26}$$

where Λ is the largest Lyapunov exponent in the classical manifold. While both linear response regimes show a decay rate that is proportional to x^2, within the nonperturbative regime, the fidelity has been shown [22–24] to be *independent* of the perturbation strength.

Linear Response and Random Matrix Theory

The linear response is about the correlation. The two operators $\hat{H}_0$ and $\hat{B}$ in the parametric Hamiltonians $\hat{H}_{1,2} = \hat{H}_0 \pm x\hat{B}$ can be modeled then with GOE matrices. The resulting correlator takes the form [25]

$$\mathcal{C}(t) = \frac{t^2}{\nu} + \frac{t}{2} + \int_0^t d\tau \int_0^\tau d\tau' b_2(\tau') \tag{3.27}$$

where ν is the universality index and $b_2(t)$ is the two-point correlation factor, both introduced in the previous chapter. This gives the fidelity in a linear response to be

$$F(t) \sim \exp\left(-(2\pi x)^2 \left[\frac{t^2}{\nu} + \frac{t}{2} + \int_0^t d\tau \int_0^\tau d\tau' b_2(\tau')\right]\right) \tag{3.28}$$

The RMT result of Eq.(3.28) has also been derived using field theoretical (supersymmetry) approaches.

3.3 Fidelity from Wavepacket Dynamics

3.3.1 The Local Density of States Kernel (LDoS)

A very useful way to determine the various perturbation borders, Eqs.(3.24, 3.25), is via the parametric analysis of the Local Density of States (LDoS). The main question asked is "How does a known unperturbed state couple and spread out

into the perturbed basis?" The *local density of states* is formally defined as

$$P(E|n) = \sum_m \left|\left\langle \phi_m | \phi_n^0 \right\rangle\right|^2 \delta(E - E_m) \tag{3.29}$$

with a kernel of

$$P_{nm} = \left|\left\langle \phi_m | \phi_n^0 \right\rangle\right|^2 \tag{3.30}$$

This kernel can be seen as a matrix formed by the unitary basis transform matrices Q_0, Q whose columns are the respective eigenvectors $\{|\phi_n^0\rangle\}, \{|\phi_m\rangle\}$, so that

$$P_{nm} = \left|(Q \cdot Q_0)_{nm}\right|^2$$

Averaging the kernel over a small energy window of unperturbed states gives the *quantum LDoS lineshape*

$$P(r) = \langle P_{nm} \rangle_E \tag{3.31}$$

The classical counterpart to this lineshape is found by integrating phase space over the perturbed/unperturbed isopotential surfaces

$$P_{cl}(E) = \int dqdp\, \rho_m(p,q)\rho_n(p,q) \tag{3.32}$$

where ρ_m and ρ_n are the Wigner functions of the states $|\phi_n^0\rangle$ and $|\phi_m\rangle$. If the two lineshapes of Eqs.(3.31, 3.32) are equivalent, one can then define a *detailed* QCC [26–28]. The behavior of $P(r)$ under perturbation theory shall dictate the three parametric regimes, but first, let us discuss how the LDoS kernel is manifest

in the fidelity.

3.3.2 Fidelity and the LDoS Kernel

Noting that if $\hat{H}_1 = \hat{H}_2 + 2x\hat{B}$, we can treat $\hat{H}_2$ as an 'unperturbing' Hamiltonian and work in its basis - $\hat{H}_1$ can then be seen as a 'perturbing' Hamiltonian. This is easiest within the mathematics if the forward evolution removes the environmental effects, so that $\hat{H}_2 = \hat{H}_0$. Absorbing the factor of 2 into the perturbation strength, we can write

$$F(t) = |f(t)|^2 = \left| \langle \psi_0 | \exp(-i\hat{H}_0 t/\hbar) \exp(i\hat{H}_1 t/\hbar) |\psi_0\rangle \right|^2 \tag{3.33}$$

Taking the fidelity amplitude and inserting completeness relations in the bases of $\hat{H}_0$ (which we will denote with a "(0)" superscript in the eigensolutions) and $\hat{H}_1$ (no superscript), we can evaluate the fidelity amplitude, $f(t)$, as

$$\begin{aligned} f(t) &= \langle \psi_0 | \exp(-i\hat{H}_0 t/\hbar) \exp(i\hat{H}_1 t/\hbar) |\psi_0\rangle \\ &= \langle \psi_0 | \left(\sum_n \left| n^{(0)} \right\rangle \left\langle n^{(0)} \right| \right) \exp(-i\hat{H}_0 t/\hbar) \exp(i\hat{H}_1 t/\hbar) \left(\sum_m |m\rangle \langle m| \right) |\psi_0\rangle \\ &= \sum_{n,m} \langle m|\psi_0\rangle \left\langle \psi_0|n^{(0)} \right\rangle \left\langle n^{(0)}|m \right\rangle \exp(-i\omega_{nm} t) \end{aligned} \tag{3.34}$$

where $\omega_{nm} = (E_n^{(0)} - E_m)/\hbar$. Denoting the initial density matrix as $\hat{\rho} = |\psi_0\rangle\langle\psi_0|$ and inserting a second completeness where appropriate

$$\begin{aligned} f(t) &= \sum_{n,m} \langle m|\,\hat{\rho}\,|n^{(0)}\rangle\langle n^{(0)}|m\rangle \exp(-i\omega_{nm}t) \\ &= \sum_{n,m} \langle m| \left(\sum_k |k^{(0)}\rangle\langle k^{(0)}|\right) \hat{\rho}\,|n^{(0)}\rangle\langle n^{(0)}|m\rangle \exp(-i\omega_{nm}t) \\ &= \sum_{n,m}\sum_k \rho_{kn}\langle m|k^{(0)}\rangle\langle n^{(0)}|m\rangle \exp(-i\omega_{nm}t) \end{aligned} \tag{3.35}$$

We can now see the connection between fidelity and the kernel of the local density of states (LDoS), P_{nm}. For the LDoS between $\hat{H}_{0,1}$, the kernel is $P_{nm} = \left|\langle m|n^{(0)}\rangle\right|^2$. Let us denote the amplitude of the LDoS kernel as $T_{nm} = \langle n^{(0)}|m\rangle$. Contracting across the k index yields

$$f(t) = \sum_{n,m} \left(\hat{T}^\dagger \cdot \hat{\rho}\right)_{nm} T_{nm} \exp(-i\omega_{nm}t) \tag{3.36}$$

The behavior of the fidelity - in particular, the plateau at $t \to \infty$ - is dependent on which initial state is chosen. There are two 'extremes' to the chosen initial states: (a) a random initial state, whose elements are drawn from a Gaussian distribution. This state has the largest Shannon entropy, *i.e.* it can contain the most information, (b) a pure initial state, which is an eigenstate of the unperturbed Hamiltonian. We consider these two extremes in later chapters. For the sake of discussion, let us simply chose a pure initial state. The density matrix for a pure state is an

identity matrix, so the fidelity amplitude in this case becomes

$$\begin{aligned} f(t) &= \sum_{n,m} T^*_{mn} T_{nm} \exp(-i\omega_{nm} t) \\ &= \sum_{n,m} P_{nm} \exp(-i\omega_{nm} t) \end{aligned} \tag{3.37}$$

For this initial state choice, the fidelity amplitude can then be seen to be directly related to the LDoS kernel - it is nothing more than a Fourier transform of the LDoS! Under the pure initial state choice, the fidelity in Eq.(3.33) becomes the *survival probability*

$$P(t) = \left| \langle \psi_0 | \exp(i\hat{H}_1 t/\hbar) | \psi_0 \rangle \right|^2 \tag{3.38}$$

The difference between initial state choice appears in the density matrix of Eq.(3.36). Although this calculation is very specific to the initial condition that we have chosen, nevertheless it clearly shows the tight connection between the LDoS, survival probability and fidelity. We would like to remark once more that Eq.(3.36) is quite generic and is applicable, independent of the initial conditions. While this affects the long-term behavior of the fidelity, the short-term behavior (Gaussian/exponential decays) remain relatively unaffected. Therefore, we can use the LDoS kernel to investigate the borders of the three fidelity regimes.

3.3.3 Regimes of Fidelity: Revisited

From the previous discussion and specifically Eq.(3.36), it is clear that the borders of perturbation theory pertain in exactly the same manner in both the calculation of the LDoS and the one of fidelity. We give here an overview of the border results based on LDoS analysis [26–28]. Recall the three regimes of fidelity (standard perturbative, Wigner (FGR), nonperturbative) and the associated borders between them, x_c, x_{prt}. Using first-order perturbation theory (FOPT), we get for the perturbed state

$$|m\rangle \approx \left|m^{(0)}\right\rangle + x \sum_{k\neq m} \left|k^{(0)}\right\rangle \frac{B_{mk}}{E_m^{(0)} - E_k^{(0)}} \tag{3.39}$$

Inserting into the LDoS yields

$$T_{nm} \approx \left\langle n^{(0)}|m^{(0)}\right\rangle + x \sum_{k\neq m} \left\langle n^{(0)}|k^{(0)}\right\rangle \frac{B_{mk}}{E_m^{(0)} - E_k^{(0)}} \tag{3.40}$$

Therefore the LDoS kernel, to first-order, is

$$P_{nm} \approx P_{\text{FOPT}} = \begin{cases} 1; & n = m \\ \frac{x^2|B_{nm}|^2}{\left|E_n^{(0)} - E_m^{(0)}\right|^2}; & n \neq m \end{cases} \tag{3.41}$$

The above approximation fails to adequately capture the actual lineshape when the levels begin to mix beyond the mean level spacing - this is sketched in the left of Fig. (3.3). Within this regime, the majority of the LDoS is contained within

the initial unperturbed level. Imposing such requirement, one obtains a threshold on the perturbation strength

$$1 \approx \frac{x^2\sigma_B^2}{\Delta^2} \longrightarrow x_c \sim \frac{\Delta}{\sigma_B} \tag{3.42}$$

where $\sigma_B = \left\langle |B_n m|^2 \right\rangle$ is the variance of $\hat{B}$ and Δ is the mean level spacing.

As the perturbation strength is increased, two regions are developed in the LDoS, a core region with a half-width given by Γ, and outer small tails, with the majority of occupying states within the core region. This is sketched in the middle of Fig. (3.3). The width factor Γ arises in the approximation by taking the perturbation theory out to infinite order (PRT), and appears in the LDoS kernel approximation as

$$P_{nm} \approx P_{\mathrm{PRT}} = \frac{x^2 \left|B_{nm}\right|^2}{\Gamma^2 + \left|E_n^{(0)} - E_m^{(0)}\right|^2} \tag{3.43}$$

Γ is technically found by imposing a normalization of P_{PRT}. Typically it was found that Γ follows a Fermi-Golden-Rule behavior, *i.e.* $\Gamma \sim x^2\sigma_B^2/\Delta$.

The LDoS approximation in Eq.(3.43) fails when Γ reaches the bandwidth $\Delta_b \gg \Delta$. At that point, the two separate core-tail regions merge, which is sketched in the right of Fig. (3.3). Equating the two relevant energy scales $\Gamma \sim \Delta_b$, one gets

$$1 \approx \frac{x^2\sigma_B^2}{\Delta_b^2 + \Delta^2} \longrightarrow x_{prt} \sim \frac{\Delta_b}{\sigma_B} \tag{3.44}$$

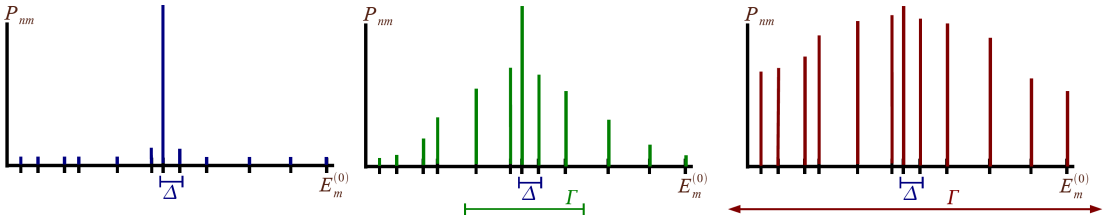

Figure (3.3): A sketch of the LDoS profile in the various regimes. On the left, the LDoS for the standard perturbative regime, $x < x_c$. In this case, only states within a mean level spacing (i.e. 'nearby') are occupied. In the middle, the LDoS for the Wigner (FGR) regime, $x_c < x < x_{prt}$. In this case, a core region with a width given by Γ is flanked on either side by smaller contributing tails. The majority of occupied states occur within the width Γ. On the right, the LDoS for the nonperturbative regime, $x > x_{prt}$. In this case, most of the states are occupied, and the distinction between the core and tail regions begins to fail. The width Γ in this case is typically larger than some finite bandwidth, Δ_b.

In practice, in order to evaluate the various perturbation limits, it was proposed in [28] to look at other moments of the LDoS. In particular, we can look at the energy dispersion and its perturbative approximations

$$\delta E = \Delta\sqrt{\sum_r r^2 P(r)} \tag{3.45}$$

$$\delta E_{\mathrm{FOPT}} = \Delta\sqrt{\sum_r r^2 P_{\mathrm{FOPT}}(r)} \tag{3.46}$$

$$\delta E_{\mathrm{PRT}} = \Delta\sqrt{\sum_r r^2 P_{\mathrm{PRT}}(r)} \tag{3.47}$$

in which $P(r)$ is the averaged LDoS lineshape discussed in the previous chapter. The point at which the perturbative approximations in Eqs.(3.46,3.47) deviate from the actual dispersion of Eq.(3.45) can also be used to quantify the perturba-

tive borders, x_c, x_{prt}. This is the approach that will be used heavily in Chapters 5 & 7.

3.4 Conclusion

We have introduced the measure of fidelity and its role in defining the stability of a system to external perturbations. A linear response approach to fidelity was shown, which gave an expression in terms of the correlator. Various decay laws were identified depending on the strength of the perturbation. The LRT analysis was shown to be parallel with the parametric LDoS analysis. A relation between fidelity and LDoS was finally established. Armed with these general results, we are now ready to analyze the fidelity decay for various models.

Chapter 4

Fidelity of Many-Body Chaos: The Bose-Hubbard Hamiltonian

...and I awoke, and faintly bouncing round the room, the echo of whomever spoke...

-Phish, Bouncing Around the Room

4.1 Physical Systems of Interest

In the past century, physics was mainly characterized by great advances in understanding the properties of one-particle systems. Recent experimental developments have drawn attention to the effects of many-particle systems, in particular to systems of interacting bosons on a lattice in which there is a competition between two mechanisms - boson-boson interactions and kinetic tunneling. The interplay between the two mechanisms is responsible for the chaotic motion. An-

alytically, relative populations/phases at each lattice site play the role of the DOF, and the total boson population and energy are the constants of motion - therefore, the chaotic condition of $2d > k$ is easily met for relatively small lattices, making bosonic lattice systems an ideal study in complex behavior.

Out of all physical realizations of bosonic lattice systems, none hold as much promise as ultra-cold bosons loaded in optical lattices [29–31]. The lengthscale that characterizes a quantum particle (whether boson or fermion) is the *deBroglie thermal wavelength*

$$\lambda_T = \sqrt{\frac{2\pi\hbar^2}{mk_BT}} \tag{4.1}$$

where m is the particle mass, T is the system temperature, and k_B is the Boltzmann constant. At high temperatures, the quantum particles can be treated as classical particles, like billard balls with a velocity and a mean separation distance of δr. As temperature is lowered, we eventually consider the particles as quantum wavepackets, with a length of λ_T. At the point where the spread of the quantum wavepacket scales as the classical mean separation, $\lambda_T \sim \delta r$ (which happens at temperature T_c), the individual particle wavefunctions begin to overlap each other, creating one large shared macroscopic wave, called the *Bose-Einstein condensate*[†] (BEC) [32]. At $T = 0$, all the particles are in the same ground state, giving a pure condensate. In order to reach the T_c regime, the system required multiple coolings. The first is laser cooling[‡], in which bosons 'shed' kinetic energy

[†]The BEC 'gas' picture presented above was first experimentally observed in gases of alkali atoms by Weiman, Cornell, & Ketterle in 1995 - earning the 2001 Nobel Prize in Physics.
[‡]The application of laser cooling in atomic boson condensation was also awarded the 1997 Nobel Prize in Physics, to Claude Cohen-Tannoudji, William Phillips, & Steven Chu.

to photons of incoming lasers [33]. This cools the gas temperature to hundreds of microkelvins, which is still above the critical point. The second cooling is an evaporative one, much like steam escaping from a hot maté, in which the particles are magnetically trapped, the potential is lowered slightly to allow the more energetic particles to escape, and the system equilibrates to a lower temperature. After applying this process several times, the system reaches the critical temperature (typically several nanokelvin) where condensate forms. The above creation of a condensate using atoms has become very popular, due to the ease of probing the condensate with optical methods, as well as the ease in creating trapping lattices with laser standing waves ("optical lattices"). Interactions between the bosons are also quite controllable optically, making BEC a viable avenue for quantum computation.

Besides ultra-cold atoms in optical lattices, other physical realizations of bosonic lattice systems abound. Phonons in lattice arrays are studied in coupled micromechanical cantilevers [34, 35], shown in Fig. (4.1a). Another phonon lattice example occurs in chemical physics where the phonons are the vibrational modes of intramolecular chemical bonds [36–41] shown in Fig. (4.1b). A last example is seen in arrays of superconducting Josephson junctions Fig. (4.1c), in which the boson is a Cooper-pairing of electrons in the superconductor [42–45].

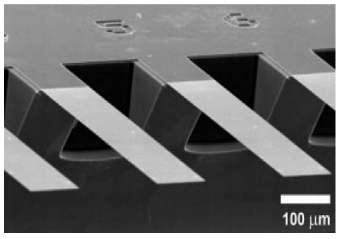

(a) An array of micro-mechanical cantilevers

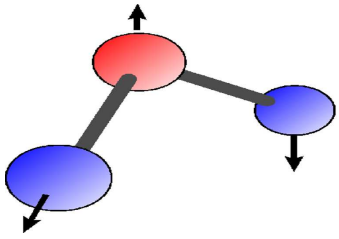

(b) Molecular bond vibrations of a molecule

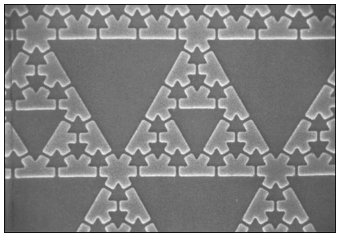

(c) An array of superconducting Josephson junctions

Figure (4.1): Three examples of interacting bosonic lattice systems. Figs. (4.1a, 4.1c) taken from [34, 44], respectively.

4.2 The Bose-Hubbard Hamiltonian (BHH)

The mathematical model that describes BEC in optical lattices - and also the boson systems presented in Fig.(4.1) - is the so-called *Bose-Hubbard Hamiltonian* [46], derived in Appendix B.3 as

$$\hat{H} = \sum_{i}^{f} \nu_i \hat{b}_i^\dagger \hat{b}_i + \frac{1}{2} \sum_{i}^{f} U_i \hat{b}_i^\dagger \hat{b}_i^\dagger \hat{b}_i \hat{b}_i - \sum_{i,j=i\pm 1}^{f} k_{ij} \hat{b}_i^\dagger \hat{b}_j \tag{4.2}$$

where f is the number of lattice sites, ν_i is the i^{th} site's potential depth, $U_i = \frac{4\pi a_s \hbar^2}{m V_{\text{eff}}}$ is the boson-boson interaction strength, and k_{ij} is the tunneling strength of a particle between next-neighbor sites (which can be viewed as the kinetic portion of the Hamiltonian). Let us consider a special case of the BHH, in which the on-site potential terms vanish $v_i = 0$, and the tunneling rates/interaction strengths are constant $k_{ij} \to k$, $U_i \to U$. In the context of the Josephson junction arrays

from Fig.(4.1c), k is given by the Josephson energy E_J, while U measures the Coulomb interaction of the charged bosons. In the context of intramolecular vibrations from Fig.(4.1b), k accounts for electromagnetic and mechanical couplings of adjacent atoms in the molecule, while U represents the anharmonic softening of the extending bonds. Using $\hat{n}_i = \hat{b}_i^\dagger \hat{b}_i$ and $[\hat{b}_i, \hat{b}_j^\dagger] = \delta_{ij}$ gives

$$\hat{H} = \frac{U}{2} \sum_i^f \hat{n}_i(\hat{n}_i - 1) - k \sum_{i,j=i\pm1}^f \hat{b}_i^\dagger \hat{b}_j \tag{4.3}$$

This equation is parametric with k, so that the second sum in the equation plays the role of a perturbation operator. For the remainder of the chapter, Eq.(4.3) is the quantum Hamiltonian considered, since it is the 'minimum' chaotic model - *i.e.* there are two constants of motion (the number of bosons and the system energy). Under a Wannier basis, the number of DOF is f - the system is thusly chaotic for $f > 2$. We shall consider the minimal case, $f = 3$, called the 'trimer'.

4.2.1 Classical Limit of the BHH

Since we are interested in investigating fidelity decay in the semiclassical limit as well, we need to identify the classical limit of Eq.(4.3). Let us start by rescaling the annihilation/creation operators as

$$\hat{c}_i = \frac{\hat{b}_i}{\sqrt{N}}, \quad \hat{c}_i^\dagger = \frac{\hat{b}_i^\dagger}{\sqrt{N}}, \quad [\hat{c}_i, \hat{c}_j^\dagger] = \frac{\delta_{ij}}{N}, \quad \hat{\tilde{n}}_i = \frac{\hat{n}_i}{N} \tag{4.4}$$

It is clear to see that in the limit of $N \to \infty$, the commutator goes to zero. One can thusly define an effective $\hbar = N^{-1}$ and identify the classical limit with the $N \to \infty$ limit. After dividing Eq.(4.3) by N and applying the above rescalings, we get

$$\mathcal{H} = \frac{\hat{H}}{N} = \frac{UN}{2} \sum_{i}^{f} \hat{\hat{n}}_i(\hat{\hat{n}}_i - 1) - k \sum_{i,j=i\pm1}^{f} \hat{c}_i^\dagger \hat{c}_j \tag{4.5}$$

Next, we want to define the following scaling parameters

$$\tilde{U} = UN, \quad \lambda = \frac{k}{\tilde{U}} \tag{4.6}$$

Treating the creation/annihilation operators as c-numbers (which is appropriate in the $N \to \infty$ limit) and using the Heisenberg relations

$$\hat{c}_j \to I_j \exp(i\phi_j), \quad \hat{c}_j^\dagger \to I_j \exp(-i\phi_j) \tag{4.7}$$

where I_j, ϕ_j are classical action-angle variables in the ranges $I_j \in [0, 1]$, $\phi_j \in [-\pi, \pi]$, one comes out with the following classical Hamiltonian

$$\tilde{\mathcal{H}} = \frac{1}{2} \sum_{i}^{3} I_i^2 - \lambda \sum_{i,j=i\pm1}^{f} \sqrt{I_i I_j} \exp[-i(\phi_i - \phi_j)] \tag{4.8}$$

with a corresponding energy observable of $\tilde{E}$. From Eq.(4.8), the evolution can then be found from the HEOM discussed in Chapter 2, for a rescaled time $t \to$

$\tilde{U}t$

$$\begin{aligned} \frac{\partial \phi_i}{\partial t} &= I_i - \lambda \sum_j \sqrt{\frac{I_j}{I_i}} \cos(\phi_j - \phi_i) \\ \frac{\partial I_j}{\partial t} &= 2\lambda \sum_i \sqrt{I_i I_j} \sin(\phi_j - \phi_i) \end{aligned} \tag{4.9}$$

Therefore, it can be seen that λ (alternatively k) controls the nonlinearity (and hence chaos) in the evolution [37, 47]. For $\lambda \to 0$, the system becomes a set of uncoupled oscillators. In the opposite limit $\lambda \to \infty$ the kinetic term dominates. Both limiting cases correspond to integrable classical dynamics. Chaos emerges instead for intermediate values of λ. One ought take note that the correct classical limit is achieved by $N \to \infty$, but at the same time keeping λ constant [1,48].

4.3 Signatures of Chaos in the BHH

4.3.1 Classical Phase Space

We start our analysis by a direct characterization of the classical phase space. In Fig.(4.2), we report representative Poincare plots resulting from the Hamiltonian, Eq.(4.8) for $\lambda = \{0.005, 0.05, 2\}$. We see that for the small and large values of λ, the phase space is integrable, while chaos appears for the intermediate value of λ-values.

Another view of the classical dynamics can be seen by considering the trajectories

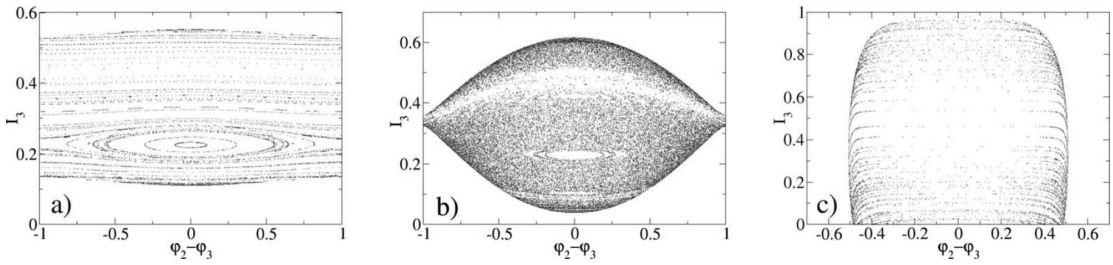

Figure (4.2): Poincaré section in the plane $\phi_1 = \phi_3$ for the classical BHH, Eq. (4.8), with the action I_3 on the y-axis and the difference $\phi_2 - \phi_3$ (in units of π) on the x-axis. The three panels correspond to $\lambda = \{0.005, 0.05, 2\}$, from left to right. The system parameters used were $\tilde{E} = 0.2, N = 230, \tilde{U} = 280, f = 3$. Figure taken from [48].

in individual sites. In Fig. (4.3), a single trajectory is plotted as $I_i \cos(\phi_i)$ vs. $I_i \sin(\phi_i)$, which gives a 'polar' image of the evolution. In this view, if all particles are contained in a single site, the trajectories all fall along the perimeter of a unit circle. For $N = 230, \tilde{U} = 280, \lambda = 0.054$, we plot the trajectories for three different energies: $\tilde{E} = 0.26$ for chaotic dynamics, $\tilde{E} = 0.06$ for a configuration close to the lower edge of the spectrum, and $\tilde{E} = 0.39$ close to the higher spectral band edge. For $\tilde{E} = 0.26$, the trajectories are seen as fairly ergodic. The lower energy trajectory behavior approaches nearly closed shells with the same radius for all three sites - an equipartitioned ground state. The higher energy trajectory approaches a single site closed shell, a phenomenon called 'self-trapping' which will be further discussed later in the chapter.

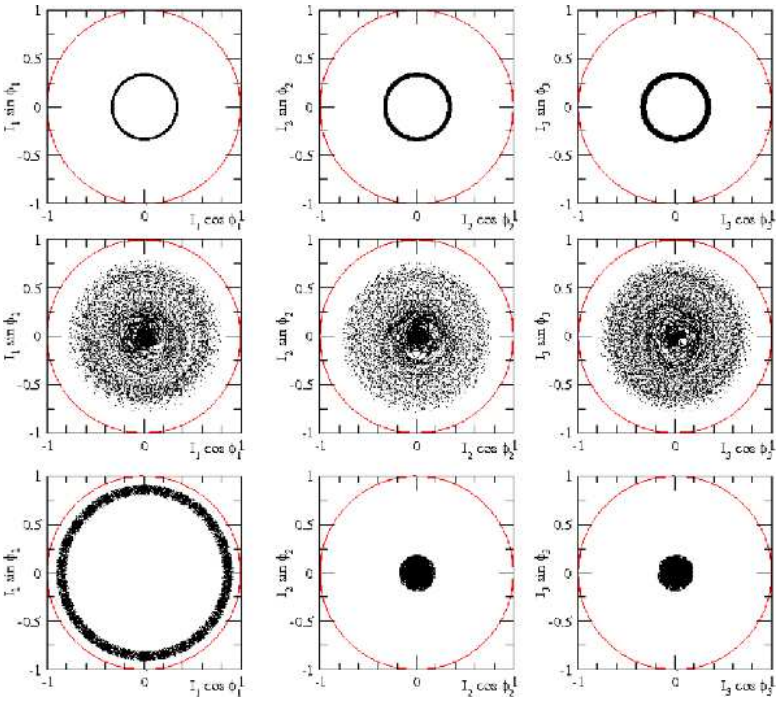

Figure (4.3): Trajectories of the BHH trimer for $N = 230, \tilde{U} = 280, \lambda = 0.053 (k = 15)$. The three columns correspond to each individual site, while the rows correspond to the three energies $\tilde{E} = 0.06, 0.26, 0.39$. The outer red circle is the limit of accessible phase space, that corresponds to all bosons in a single site.

4.3.2 Power Spectra of a Generalized Force

As discussed in Chapter 2, another measure of chaoticity is related with the structure of the power spectrum of a generalized force. In our case, we will assume that the unperturbed Hamiltonian is given by Eq.(4.8), while as perturbation we will consider a small change in the coupling term, λ. The classical fluctuator is given by

$$\begin{aligned} \mathcal{F} &= -\frac{\partial \tilde{\mathcal{H}}}{\partial \lambda} \\ &= \sum_{i,j=i\pm 1} \sqrt{I_i I_j} \exp(\phi_j - \phi_i) \end{aligned} \tag{4.10}$$

One can define a rescaled generalized force correlation which takes the form

$$\mathcal{C}(\tau) \rightarrow \frac{N^2}{\tilde{U}}\mathcal{C}(\tau) \tag{4.11}$$

and consequently we have a rescaled power spectrum of

$$\mathcal{C}(\omega) \rightarrow \frac{N^2}{\tilde{U}}\mathcal{C}(\omega) \tag{4.12}$$

Representative power spectra are shown in Fig.(4.4) for various energies. Note that as energy is increased, the power spectrum becomes more peaked, representative of an integrable system. This is consistent with the previous results of Fig.(4.3). Furthermore, based on the QCC relation about the classical power spectrum and the quantum bandprofile, Eq.(2.13), we have

$$\tilde{C}(\omega) = \frac{2\pi\tilde{U}}{\Delta N^2}\left\langle |B_{jk}|^2 \right\rangle \tag{4.13}$$

where we have used $g(E) = \Delta^{-1}$ for unfolded spectra. The comparison between the classical power spectrum and the quantum bandprofile are also reported in Fig.(4.4), in which a fair agreement is evident.

Two important features are manifest in the spectra. First, there is the presence of a finite bandwidth ω_c, as previously discussed for chaotic systems. The limits of the figure correspond to this bandwidth, which is mirrored in the banded quantum perturbation matrix's bandwidth of Δ_b, as shown in Fig. (4.5). Secondly, the spectra is not flat, but exhibit distinct structures within the bandwidth Δ_b. In

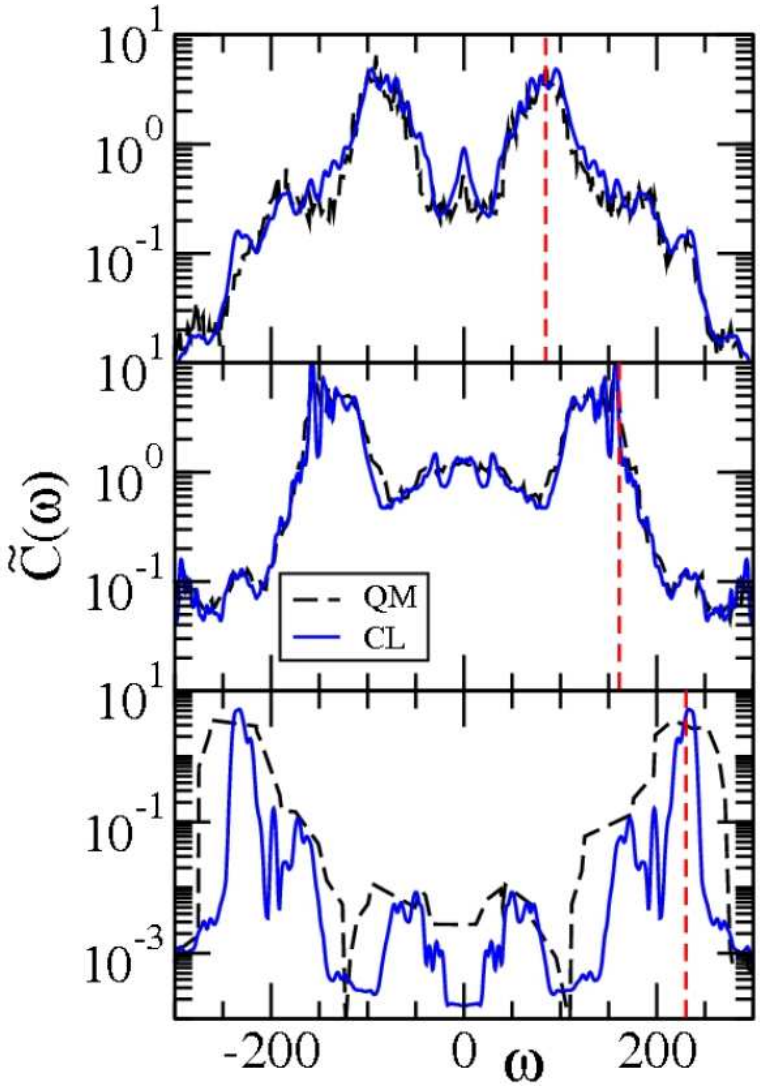

Figure (4.4): Classical correlation spectra (solid blue) and the rescaled quantum bandprofile (dashed black) for the energies $\tilde{E} = 0.06, 0.26, 0.39$, from top to bottom respectively. The limits of ω correspond to the classical bandwidth ω_c, while the vertical dashed lines correspond to the lobe position at ω_{echo}, which moves outward as the energy increases.

particular, note the appearance of side lobes in the spectra at ω_{echo}, which are marked in Fig. (4.4) by vertical dashed lines, whose position moves to higher frequencies as the energy is increased. These lobes produce oscillations in the generalized force correlations and are related to a novel behavior in the fidelity.

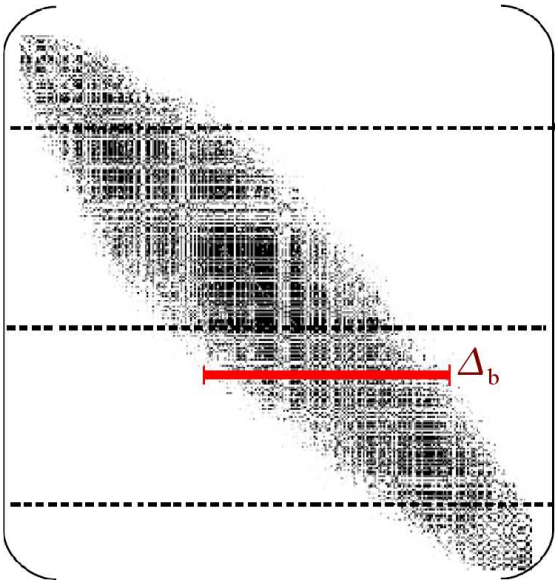

Figure (4.5): Quantum perturbation matrix structure for $\hat{B}$, of the BHH for $N = 230, \lambda = 0.053$. The dashed horizontal lines correspond to the energy index for $\tilde{E} = 0.06, 0.26, 0.39$. Note that the matrix structure is complicated, yet banded for a width of Δ_b.

4.3.3 Level Spacing Distributions

A popular measure used in quantum chaos studies is the level spacing distribution $P(s)$. Within Chapter 2, we discussed the predictions of RMT for chaotic and integrable systems, as far as this quantity is concerned. By utilizing its study, we will be able to identify λ regimes where chaotic dynamics sets in. We fit our numerical data of $P(s)$ with the Brody distribution

$$P_q(s) = (1+q)\beta s^q \exp\left(-\beta s^{1+q}\right), \tag{4.14}$$

where

$$\beta = \Gamma^{2+q}\left(\frac{2+q}{1+q}\right)$$

in which the parameter q takes values in the range $[0, 1]$. Specifically, for $q = 0$ the Brody distribution collapses to a Poissonian, while for $q = 1$ we get the GOE

result. Fig. (4.6) illustrates the resulting $P(s)$ for various values of λ for the BHH. From the fit, we are able to extract the repulsion parameter q. An overview of q vs. the control parameter λ is shown in Fig.(4.7) in which the level spacing distributions of the quantum BHH, Eq. (4.3), are fit to the Brody distribution, Eq. (4.14), for various λ.

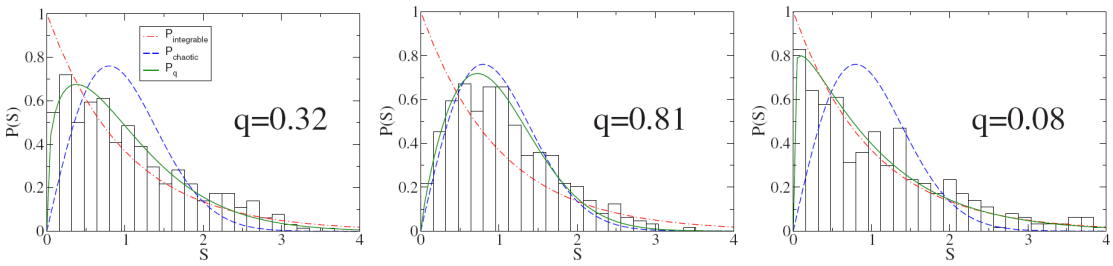

Figure (4.6): Level spacing distributions for $\lambda = 0.025, 0.05, 0.35$ ($k = 7, 14.5, 100$), from left to right. The red (dashed-dotted) curve is the Poissonian distribution (integrable), while the blue (dashed) curve is the Wigner distribution (chaotic). The green (solid) curve is the best fit of the data to the Brody distribution, Eq (4.14), with the a resulting fit parameter of $q = 0.032, 0.81, 0.08$, respectively from left to right. The numerics were performed with the following additional system parameters $\tilde{E} = 0.26, N = 230, \tilde{U} = 280$. Figure taken from [48].

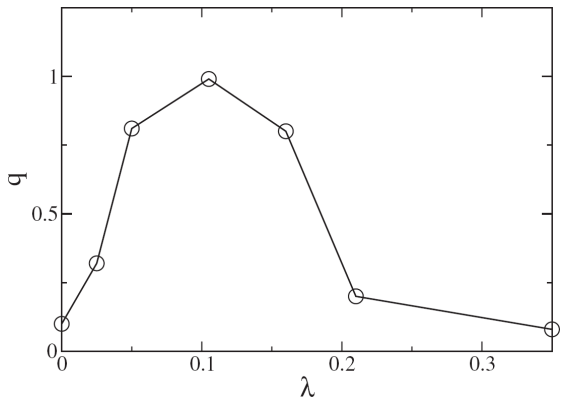

Figure (4.7): Brody fitting parameter as a function of λ. The values of $0.04 < \lambda < 0.2$ have $q \sim 1$, suggesting chaotic dynamics for these coupling strengths. Figure taken from [48].

4.4 Quantum Fidelity in the BHH

In the remainder of the chapter, we will discuss our findings on the fidelity decay of a system described by the BHH (like cold atoms in an optical lattice), that is subject to perturbations of the coupling $k \to k_0 \pm \delta k$. In the context of optical lattices, this perturbation is achieved by adjusting the intensity of the laser beams that create the lattice. The Hamiltonian of the unperturbed system is

$$\hat{H}_0 = \frac{U}{2}\sum_{i}^{3} \hat{n}_i(\hat{n}_i - 1) - k_0 \sum_{i,j=i\pm1}^{3} \hat{b}_i^\dagger \hat{b}_j \tag{4.15}$$

The fidelity is calculated with the evolutions from the two Hamiltonians $\hat{H}_{1,2} = \hat{H}_0 \pm \delta k \cdot \hat{B}$, where the perturbation is

$$\hat{B} = \sum_{i,j=i\pm1}^{3} \hat{b}_i^\dagger \hat{b}_j \tag{4.16}$$

This perturbation is similar to a change in momentum. The fidelity of such perturbations was investigated in [49], where it was found that fidelity freezes at a finite value, provided the momentum change is small enough.

As previously mentioned, we will focus on the trimer, $f = 3$. This is the minimum BHH model that contains all generic ingredients of large BHH lattice[†], so the trimer is often used as a prototype model [51–53]. The main fidelity overview is shown in Fig.(4.8), where the fidelity is a surface function of both time and

[†]This should be contrasted a recent work [50] on a kicked (non-autonomous) dimeric BEC. Without the kicking the dynamics is integrable.

various perturbation strengths δk.

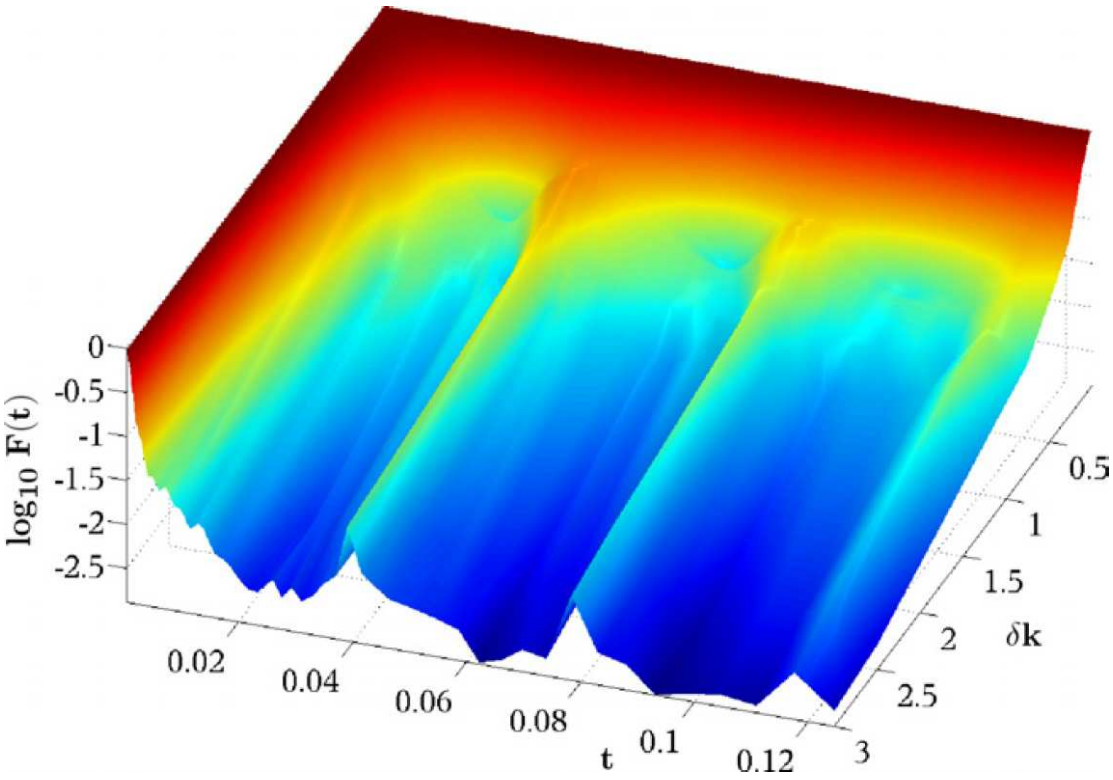

Figure (4.8): Parametric evolution of the quantum fidelity for a range of perturbation strengths δk. The initial state is taken to be an eigenstate of $\hat{H}_0$ with energy $\tilde{E} = 0.26$. The appearance of periodic revivals at multiples of t_{echo} is observed. The revivals occur at much less than the Heisenberg time, $t_H = \hbar/\Delta \sim 0.55$.

In Fig.(4.9), the middle panel shows 'slices' through Fig.(4.8) for different δk. The other two panels are likewise, but for different energies. In all figures, the striking novel behavior (in contrast to [50]) is the appearance of echoes at multiples of t_{echo}. We shall analyze the energy landscape of the perturbation operator, in order to identify t_{echo} and control echo efficiency by appropriate choice of the initial

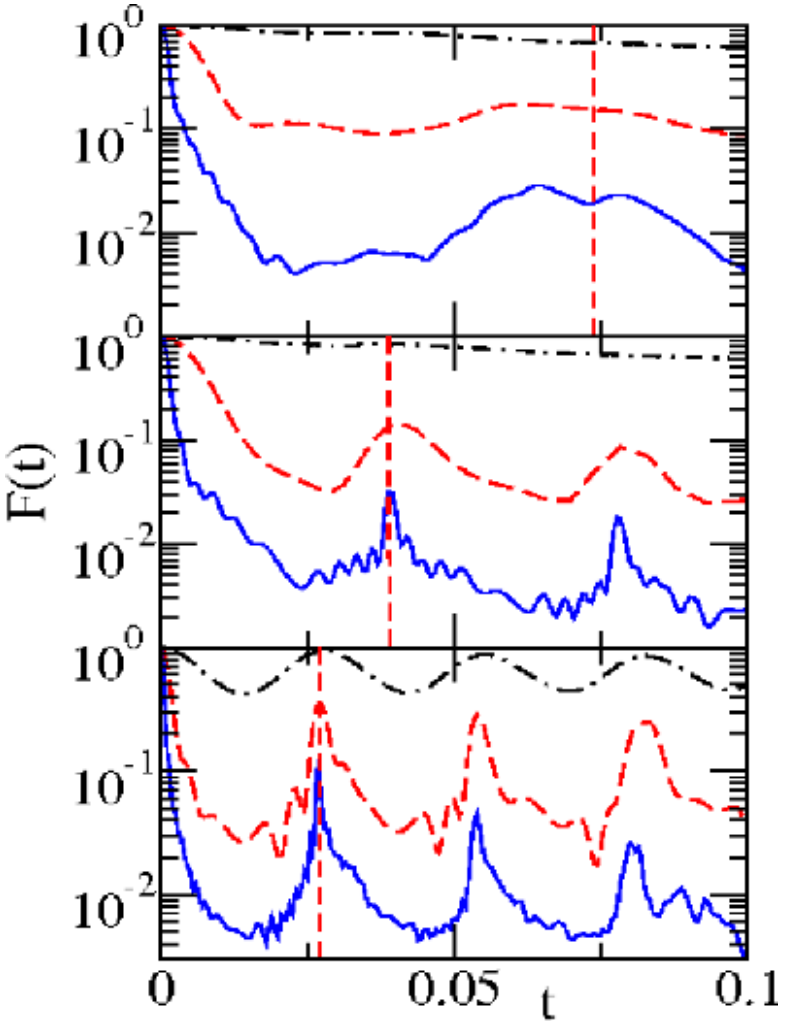

Figure (4.9): Quantum fidelities for various parameters. The three panels correspond to the energies of $\tilde{E} = 0.06, 0.26, 0.39$, from top to bottom respectively. The three curves in each panel correspond to: dash-dotted black line - standard perturbative regime, dashed red line - Wigner (FGR) regime, and solid blue line - nonperturbative regime (see following section for discussion on the three regimes). The respective numerical values are $\delta k = 0.1, 0.5, 2.5$ in the upper two panels, and $\delta k = 0.5, 2.5, 7.5$ for the lower panel. The initial preparation is an eigenstate of $\hat{H}_0$. The red dashed vertical lines correspond to t_{echo}.

preparation. We shall see for moderate perturbations δk, an 'improved' RMT modeling - which incorporates the semiclassical structures of the perturbation operator - can reproduce the echoes, while for larger perturbations we will rely on semiclassical considerations. We will show that the trajectories leading to the fidelity echoes becomes more abundant at high energies, in contrast to recent experimental results on echo spectroscopy of atoms in atom-optics billiards [54–56]

where the echoes do not survive in the strong perturbation limit. Our analysis will show this is due to self-trapping phenomena [57, 58], reflecting a generic property of interacting bosons loaded on a lattice.

4.4.1 Transient Analysis: Verification of the Three Regimes

As a quick review, recall for small perturbations in a chaotic system, we can apply the linear response approximation for fidelity seen in Chapter 3

$$F(t) \approx 1 - 2\,\delta k\, C(t) \approx \exp\left[-2\,\delta k\, C(t)\right] \tag{4.17}$$

where the integrated correlation is $C(t) = \int_0^t d\tau \int_0^t d\tau'\, \mathcal{C}(\tau - \tau')$. This implies a short-time Gaussian decay (the so-called 'Zeno' decay) of

$$F(t) \approx \exp\left[8C(0)\,(\delta k \cdot t)^2\right] \approx \exp\left[-(\gamma_Z\, t)^2\right] \tag{4.18}$$

which further evolves into one of the following two behaviors

$$\begin{aligned} F(t) &\approx \exp\left[-(\gamma_g\, t)^2\right]; \qquad \delta k < \delta k_{qm} \\ F(t) &\approx \exp\left[-\gamma_e t\right]; \quad \delta k_{qm} < \delta k < \delta k_{prt} \end{aligned} \tag{4.19}$$

depending in which regime the perturbation rests. The perturbative borders separating the above behaviors are found (via the LDoS analysis of Chapter 3 [48])

as

$$\delta k_{qm} \sim \Delta/\sigma_B \propto \frac{\tilde{U}}{N^{f/2}} \tag{4.20}$$

$$\delta k_{prt} \sim \Delta_b/\sigma_B \propto \frac{\tilde{U}}{N} \tag{4.21}$$

From Eqs.(3.17, 3.23, 4.18), we have an expectation for the decay rate's perturbation strength dependency of

$$\gamma_Z \sim \delta k^2, \quad \gamma_g \sim \delta k, \quad \gamma_e \sim \delta k^2 \tag{4.22}$$

As a first step, we wish to verify some of these dependencies. In the transient region of $t < 0.02$, well before the occurrence of the first revival, we look at the fidelity decay for varying perturbation strengths[†] in the region $\delta k > \delta k_{qm}$. We then fit the transient decay of the numerical fidelities [like those in Fig.(4.9)] to the curves in Eqs.(4.19), treating the decay rates as fitting parameters. In Fig.(4.10a), the Wigner (FGR) regime is investigated. Both the initial Zeno decay and the exponential decay recover the expectations of Eq.(4.22), as evidenced by the dashed line of slope 2.

For very strong perturbations $\delta k > \delta k_{prt}$, we enter the non-perturbative (semiclassical) regime. Identification of the non-perturbative regime with the semiclassical limit can be seen for $N \gg 1$, as $\delta k_{\rm prt} \sim \tilde{U}/N \to 0$, for a constant $\tilde{U}$ [47]. Any fixed

[†]Using the system parameters of $N = 230, \tilde{U} = 280$ gives numerical perturbative borders of $\delta k_{qm} \sim 0.08$ and $\delta k_{prt} \sim 1.22$, as well as an upper limit of $\delta k_{cl} \sim 20$. These will be the borders used throughout the remainder of the chapter.

perturbation δk, eventually yields $\delta k \gg \delta k_{\rm prt}$, for a large number of bosons. In this regime the fidelity behaves independently of the perturbative strength

$$F(t) \approx \exp\left[-\Lambda t\right]; \quad \delta k_{prt} < \delta k \tag{4.23}$$

where Λ is the maximal Lyapunov exponent associated with the underlying chaotic classical dynamics. As the perturbation strength increases into the semiclassical regime, the transient behavior changes. First, an initial exponential decay results from energy surface deformations of width δE, which is the difference between $\hat{H}_0$ and $\hat{H}_{1,2}$ - thus, $\delta E \sim \gamma_1 \sim \delta k$.

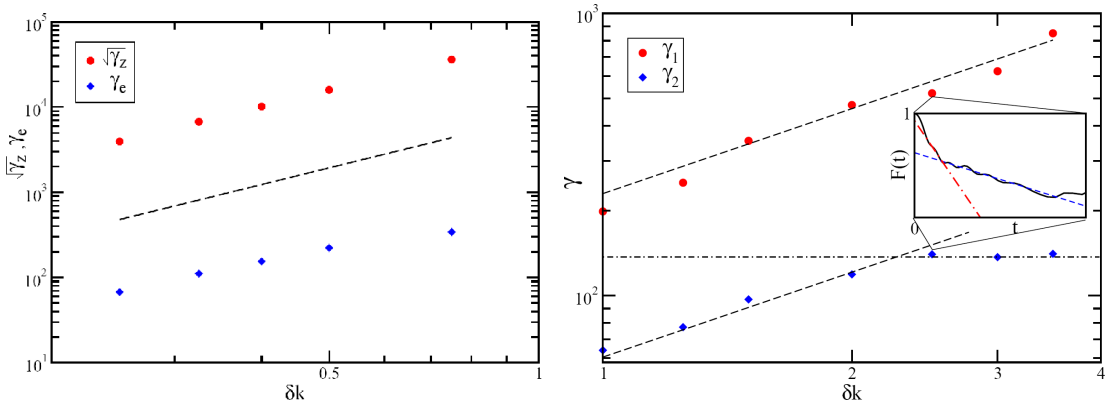

(a) Decay rates for Wigner regime, $\delta k < \delta k_{prt}$ **(b)** Decay rates for semiclassical regime, $\delta k > \delta k_{prt}$

Figure (4.10): Transient decay rates of the fidelity, for an initial eigenstate of $\hat{H}_0$, and an energy in the chaotic regime, $\tilde{E} = 0.26$. In (a), small perturbations in the Wigner regime display an initial Zeno decay (circles) followed by an exponential decay (diamonds). The dashed line shows the scaling $\propto \delta k^2$, verifying the expectation of Eq.(4.22). In (b), larger perturbations in the semiclassical regime show a rate scaling of $\propto \delta k$, followed by a second similar rate scaling, up to a classical Lyapunov rate. The inset in (b) shows a decay example for $\delta k = 2.5$.

Once the energy shell from the deformations is fully explored, a further decay rate of γ_2 is bounded by classical dynamics, with a rate given by a constant Λ. A representative decay and fit is shown in the inset of Fig.(4.10b). The scaling of $\gamma_{1,2}$ with the perturbation strength is shown in the main portion. The dashed lines again show a scaling, but now for $\gamma_{1,2} \sim \delta k$. The dotted-dashed line shows the maximal Lyapunov exponent, reached for large perturbations.

4.4.2 Fidelity Revivals

As pointed out, the interesting feature in our calculations is the appearance of echo revivals at multiples of a characteristic time, t_{echo} [see Figs.(4.8, 4.9)]. In order to gain some insight, we return to the perturbation matrix $\hat{B}$ which generates the dynamics. In Figs.(4.4), the band-profile (dashed line) is not flat, but exhibits pronounced structures within the bandwidth Δ_b. Additionally, there exist sidebands whose position ω_{echo} increases as we increase the energy $\tilde{E}$. As a result the correlator in the linear response approximation, Eq.(4.17), oscillates. This leads to strong fidelity echoes at the multiples of the characteristic time, $t_{echo} = 2\pi/\omega_{echo}$. These echoes are different from the standard mesoscopic echoes at the Heisenberg time $t_H = \Delta^{-1}$, seen in quantum systems with chaotic classical dynamics [59–62]. The revivals are related instead to non-universal structures which dominate the band-profile of the perturbation matrix and are the fingerprints of the lattice confinement.

The revivals can additionally gain understanding from the linear response, where

the LDoS core[†] has a width of Γ. For times $\leq \Gamma^{-1}$ the core is largely preserved, and the fidelity will display revivals at the point when the spectral sidelobes have gained a phase of 2π. The revival 'efficiency' (the height of the peak) is also observed to increase as the energy is increased - a point we will return to in the context of self-trapping.

4.4.3 Classical Fidelity

To further understand the origin of the echoes observed for the BHH model, in $\delta k > \delta k_{prt}$, we will employ semiclassical considerations. In the nonperturbative (semiclassical) regime, a comparison is shown in Fig.(4.11) between the quantum calculations and the classical fidelity

$$F_{cl}(t) = \int_{\Omega} dqdp\, \varrho_{-\delta k}(q,p;t)\, \varrho_{+\delta k}(q,p;t) \tag{4.24}$$

where $\varrho_{\pm\delta k}$ is the classical density function evolved under $\hat{H}(k_0 \pm \delta k)$, and the integration is performed over the complete phase space Ω. The quantum and classical calculations agree quite well, as far as the echoes are concerned, although for small times a discrepancy in the decay is observed between $F(t)$ and $F_{cl}(t)$.

[†]An excellent review of LDoS analysis of the BHH is given in [48].

4.4.4 Self-Trapping

The classical trajectories that contribute to the ensemble average of the fidelity are those that - after evolving forward in time with $\tilde{\mathcal{H}}_1$ and then backwards in time with $\tilde{\mathcal{H}}_2$ - return to the neighborhood of their initial position. Since $\tilde{\mathcal{H}}_{1,2}$ differ in the coupling between nearby wells, those classical trajectories that do not jump between wells will not feel the difference in the coupling terms. Therefore they retrace their forward propagation backwards in time, causing the action integral to vanish. These trajectories thus give a perfect contribution to the revival signal. Such trajectories are associated with energies at the upper edge of the quantum spectrum, as seen in Fig.(4.3) for $\tilde{E} = 0.39$, in which the radius can be viewed as the number of bosons in a given well. This phenomenon is known as "self-trapping" [57, 63, 64].

Self-trapping dynamics are largely integrable, in that the only term that strongly participates in the Hamiltonian is the onsite interactions - bosons that do not tunnel from a lattice site simply do not feel any perturbation to the lattice. The classical fidelity's transient decay for integrable systems no longer follows the Lyapunov exponential transient decay seen for chaotic systems. Rather the classical decay behaves in a power law fashion [65]

$$F_{cl}(t) \sim t^{-d_{eff}} \tag{4.25}$$

in which d_{eff} is the effective dimension of the system. In the case of the trimer

BHH model, Eq.(4.8), we have a six-dimensional phase space with two constants of motion (the total number of particles N and the energy $\tilde{E}$), thus $d_{eff} = 2$. However, in the high energy regime, the dynamics are largely dictated by self-trapping phenomena, leading to localization of particles in one site. In this case, the effective dimensionality of the system described by Eq.(4.8) becomes $d_{eff} = 1$.

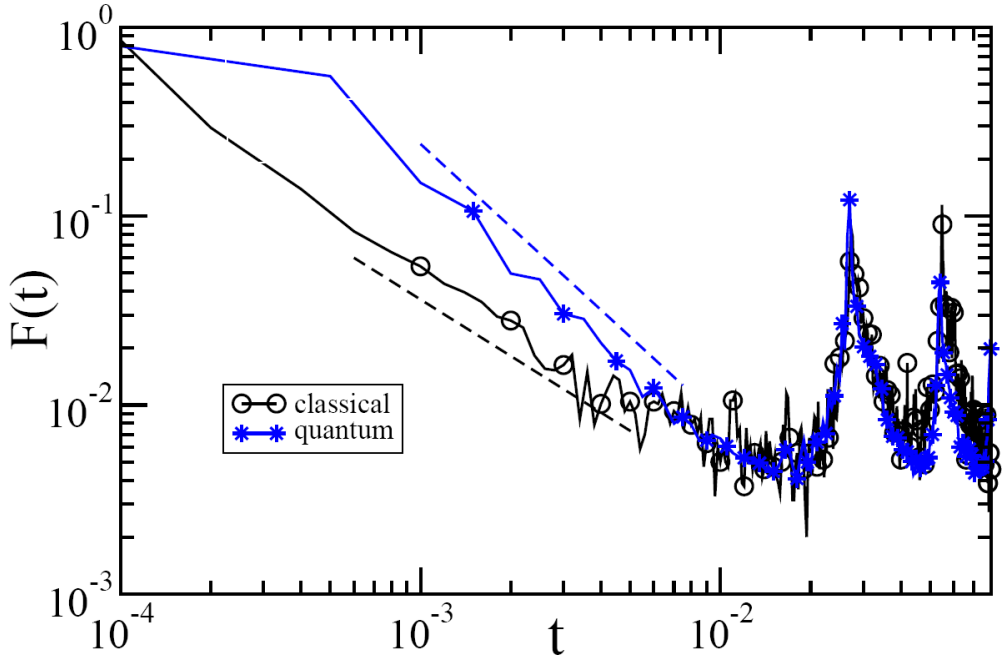

Figure (4.11): For a self-trapping energy regime (here $\tilde{E} = 0.39$), a power law fit on the transient decay for both quantum and classical fidelities. The dashed lines correspond to the best fits, with $t^{-1.46}$ (upper line), and $t^{-0.99}$ (lower line)

The quantum fidelity, on the other hand, behaves in an anomalous fashion [66],

decaying faster than the classical fidelity as

$$F(t) \sim t^{-3d_{eff}/2} \tag{4.26}$$

For the trimer, the transient decay in the self-trapping energy regime (upper spectral edge) should then classically behave as $F_{cl}(t) \sim t^{-1}$, and as $F(t) \sim t^{-1.5}$ in the quantum realm. This is verified in Fig. (4.11), in which a power law fit of the classical/quantum transient decays is performed, and presented as dashed lines (offset from the decays for visual clarity). The fitting parameter (power exponent) displays $F(t) \sim t^{-1.46}$ and $F_{cl}(t) \sim t^{-0.99}$, indeed verifying the expectations in Eqs.(4.25,4.26).

As the energy is increased, the revival efficiency also becomes much stronger, to the point that one may see complete revivals (efficiency of ~ 1). This is shown in the upper panel of Fig. (4.12), in which an almost complete revival is displayed for the quantum case. The discrepancy between the quantum and classical fidelties is due to a limited number of numerical averagings. The lower panel displays the normalized classical occupation (percentage of bosons) in the first lattice site, corresponding to the action variable $I_1(t)$. The effect of self-trapping is clearly seen then - very small periodic fluctuations in the self-trapped occupation have the same periodicity as the revivals.

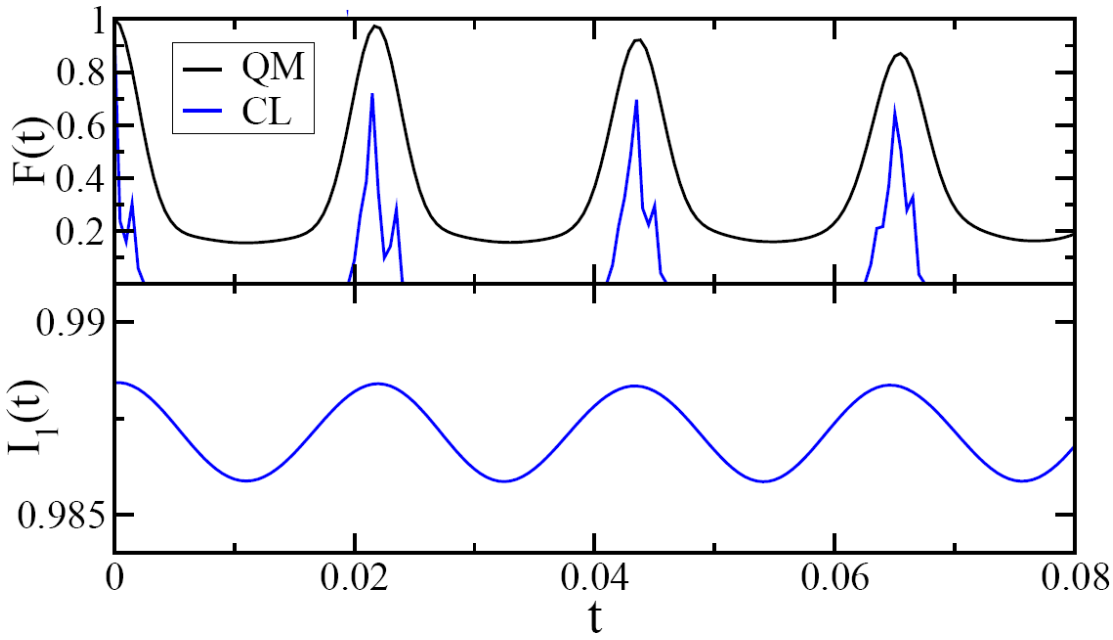

Figure (4.12): In the upper panel, fidelity in the strong self-trapping regime $\tilde{E} = 0.5$, for semiclassical perturbations of $\delta k = 7.5$. The mismatch between quantum and classical is due to low number of averagings; regardless, the strength of the echo efficiency can still be seen. In the lower panel, the occupation of the first site is shown to periodically fluctuate over time, with a periodicity matching that of the fidelity revivals.

4.5 Initial States & Bandstructure in the BHH

4.5.1 Initial States

The existence of revivals raises the question whether they are related to a specific initial state. In Fig.(4.13), the initial state is taken as either an eigenstate of $\hat{H}_0$ with energy $\tilde{E}$, or a Gaussian superposition of eigenstates centered on $\tilde{E}$ with a

width of σ_G^2. For large widths of the Gaussian state, such that the participating eigenstates of H_0 span an energy window in which the bandprofile of $\hat{B}$ is not constant, echo-efficiency is suppressed due to destructive interferences resulting from states located at parts of the spectrum where the band-structure varies. For small widths of the Gaussian state, the fidelity revivals last for $\delta k \leq \delta k_{prt}$, shown in the left panel of Fig.(4.13), in agreement with band-structure as a cause for revivals.

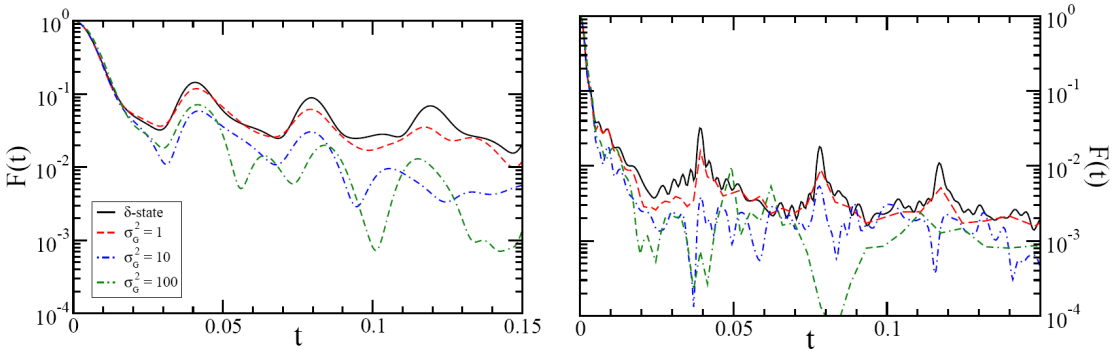

Figure (4.13): The fidelity for $\tilde{E} = 0.26$ for eigenstates of $\hat{H}_0$ (black line), and a Gaussian superposition of eigenstates centered around $\tilde{E} = 0.26$ for three widths $\sigma_G^2 = 1$ (red dashed), $\sigma_G^2 = 10$ (blue dashed-dotted), and $\sigma_G^2 = 100$ (green dotted-double dashed). It is seen that the revival efficiency is decreased for both the perturbative regime (left panel), and much more so for the semiclassical regime (right panel).

Larger widths display the destructive interference that destroys revivals. In the semi-classical regime, $\delta k > \delta k_{\rm prt}$, the revival efficiency is much more sensitive to the initial preparation, and the interference effect becomes much more pronounced, as shown in the right panel of Fig.(4.13).

4.5.2 Bandstructure

The importance of the structural bandprofile seen in Fig. (4.4), for the development of revivals is investigated by evaluating the fidelity decay $F(t)$ using an improved RMT (IRMT) model [27, 28, 67].

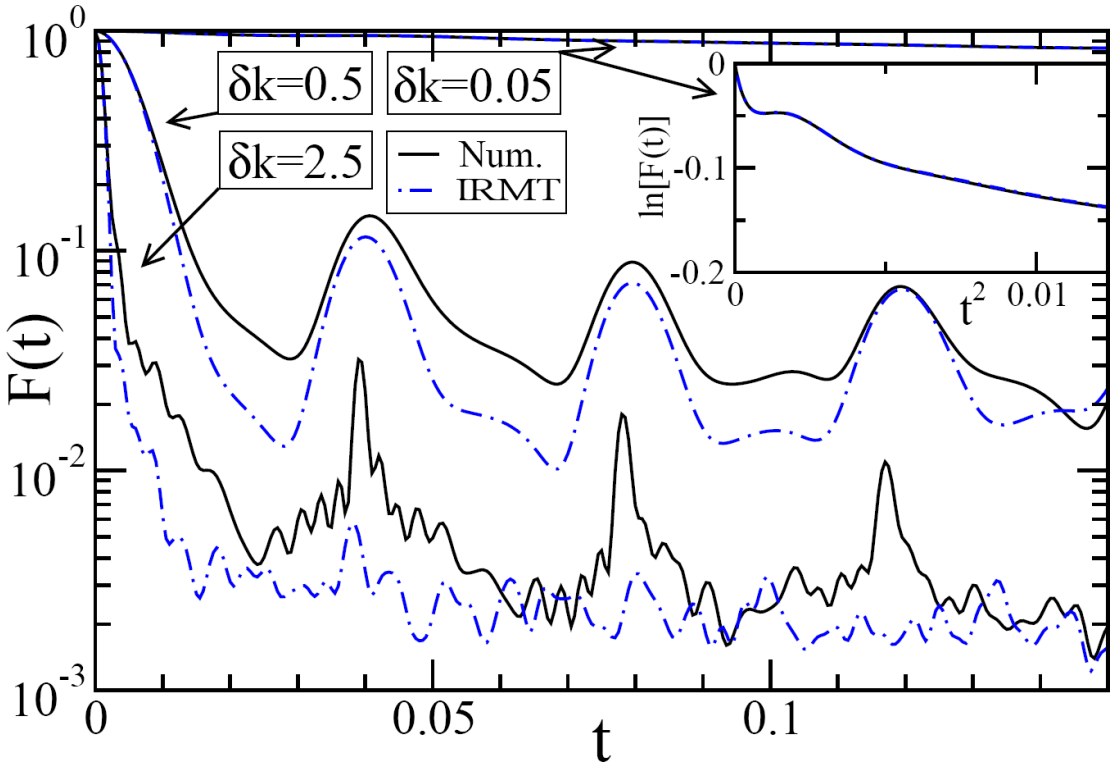

Figure (4.14): Comparison between the BHH fidelity (solid line) and that of an Improved Random Matrix Theory (IRMT) model which maintains the same bandstructure as the BHH fidelity (dotted-dashed line). The inset and upper curve are for the perturbative regime ($\delta k = 0.05$), the middle curve is for the Wigner regime ($\delta k = 0.5$), and the lower curve is for the semiclassical regime ($\delta k = 2.5$). It is seen that the IRMT model indistinguishably mimics the standard perturbative regime, and is somewhat similar to the Wigner regime - especially in the reproduction of the fidelity revivals. However, the IRMT model fails to accurately coincide with the semiclassical regime.

In contrast to the traditional Gaussian RMT models discussed in Chapter 3, where the bandprofile is constant within the bandwidth, the IRMT model maintains the same bandstructure as the BHH - however, the randomness is placed on the signs of the elements, in order to address (*i.e.* break) the correlations seen in linear response theory. In Fig.(4.14) the results are presented. An agreement with the BHH fidelity for both the perturbative regime and the Wigner regime is evident. However, the improved RMT modeling cannot describe the quantum results in the semiclassical regime. Here the revivals are related to higher-order correlations, beyond the autocorrelation function $C(\tau)$ that determines the bandprofile.

4.6 Experimental Observation of Fidelity Revival

As a closing, it is always nice for a theoretician to think experimentally. Experimental research by Nir Davidson's group at the Weizmann Institute probed stability and correlations of bosons [54, 56] within a single optical well via microwave spectroscopy. In particular, they load ^{85}Rb atoms into an 'optical wedge', formed by two crossed and slightly detuned laser sheets, as shown in the left column of Fig. (4.15). The atoms are confined in the wedge by gravity and a dipole interaction (inversely proportional to the detuning) with the lasers. The dynamics of the system are controlled by the wedge angle - a narrower angle results in 'less' chaos, as shown by the appearance of stable islands in a Poincaré section, the middle column of Fig. (4.15).

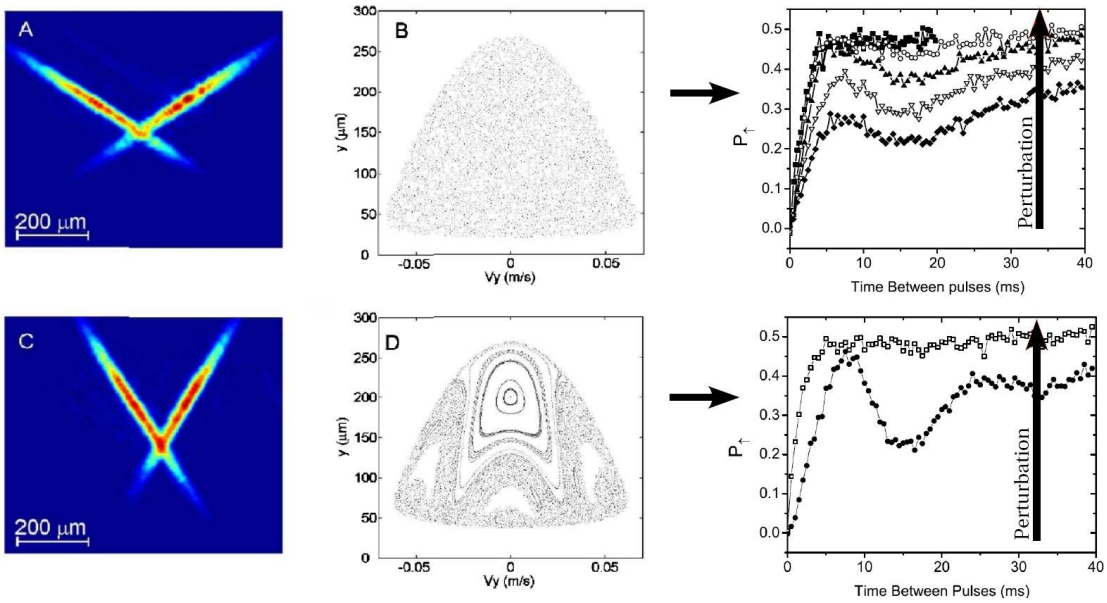

Figure (4.15): An experimental version of fidelity for bosons in an optical well. The two rows correspond to two different angles in the light wedge trap (CCD imaged in the left column), which controls the chaos of the system (middle column). A series of microwave pulses forces the upper Zeeman state to fluoresce, and the populations can then be measured over time (right column). The fidelity of the system is related to the Zeeman occupation by $F(t) = 1 - 2P_{\uparrow}(t)$. Revivals (dips in $P_{\uparrow}$) are observed, and are stronger in the less chaotic system. Increasing the perturbation strength results in decreasing the revivals.

The rubidium atoms can be in one of two hyperfine Zeeman states ($|\uparrow\rangle, |\downarrow\rangle$) and are initially prepared in the $|\downarrow\rangle$ state. A microwave pulse first places the atoms into a coherent superposition of the Zeeman states, and after the system is allowed to interact with the dipole and gravitational potentials, a series of microwave pulses forces the $|\uparrow\rangle$ states to fluoresce, which is easily detected at different times, and the occupation of the $|\uparrow\rangle$ states is measured, $P_{\uparrow}(t)$. The perturbation to the system is done by changing the detuning between the sheets, which affects the dipole

potential only.

The resulting occupation can be related to the fidelity as $F(t) = 1 - 2P_{\uparrow}(t)$, and is shown in the right column of Fig. (4.15). The behavior of the fidelity revivals [dips in $P_{\uparrow}(t)$] opposes that seen in this chapter twofold: by increasing the chaos the revival efficiency is lowered, and stronger perturbations attenuate the revival efficiency. However, it should be noted that this experimental system is for 'hot' atoms ($T = 20\mu K$ as opposed to $\sim 100nK$), so there is no Bose-Einstein condensation - therefore there is no nonlinear boson-boson interactions, and the system Hamiltonian is very different from the BHH. Regardless, it is a start to an experimental realization of fidelity for the BHH, provided multiple coupled optical wedges can be made and the system can be cooled to condensate temperatures.

4.7 Conclusion

In this chapter, the fidelity of a trimeric Bose-Hubbard Hamiltonian has been addressed, and a novel feature observed in the form of fidelity revivals at a period of t_{echo}, which is related to positions of sidelobes at ω_{echo} in the bandprofiles. By varying the energies and initial states, it has been shown that the echo efficiency can be engineered. For small perturbations an improved random matrix model can reproduce these revivals, while at large perturbations in the semiclassical limit, the classical fidelity can be used. For energies at the upper edge of the band,

trajectories trapped within a site become more prevalent, and self-trapping occurs, giving very high efficiency in the fidelity revival. For lesser energies, the revival behavior is somewhat counterintuitive, but can be understood from linear response theory, Eq. (3.12) - in that more chaos yields faster decays in the correlations, thereby increasing the fidelity. Additionally from LRT, an increase in perturbation strength *increases* the revival - in contrast to previous experimental work with hot atoms in a single chaotic trap. Lastly, while we have only discussed the trimer, as it is the 'minimum' chaos model, our findings in this chapter (fidelity revivals related to bandprofile sidelobes, bandprofile structure, self-trapping phenomena, and initial preparations) are expected to hold as well for larger lattices, $f > 3$. It is our hope that the theoretical studies of this chapter can further be used to engineer coherences within real, experimental physical systems.

Chapter 5

Probing Anderson Localization via Fidelity: Modeling

Here we are, trapped in the amber of the moment.

-Kurt Vonnegut, Slaughterhouse 5

In this chapter we investigate theoretically the wave interference phenomenon of Anderson localization by analyzing the echo dynamics due to small perturbations, *i.e.* the fidelity. We use a theoretical approach based on random matrix theory that has effectively modeled localized systems. Specifically, within the standard perturbative regime we show for localized modes a novel fidelity decay behavior, in which the inverse participation number that characterizes the localization appears directly in the fidelity's decay rate - an obvious difference from the Gaussian decay expected for diffusive or chaotic systems. While the scope of this chapter is largely theoretical, an experimental verification of our theoretical results is presented

in the following chapter, for a quasi-1D microwave cavity filled with randomly distributed scatterers.

This chapter is presented in the following manner. We will first discuss the phenomenon of Anderson localization, and then describe recent experimental evidence of the phenomenon. The Hamiltonian used to model Anderson localization is presented to motivate two pertinent measures: the characteristic localization length and the inverse participation number. We shall follow this with a discussion of a particular random matrix that captures both the previous two measures and the statistical properties of localized systems. An analytical derivation is then given for the fidelity of localized modes, within both perturbative regimes, using the statistical properties of the proposed random matrix. We conclude the chapter by a comparison of numerical fidelity calculations using RMT to both our new analytical result and the traditional Gaussian decay.

5.1 Anderson Localization

In a 1958 seminal paper [68], Phillip Anderson introduced a perturbative approach to electron transport in a crystalline lattice, in which the uncoupled sites of the lattice are the 'unperturbed' system, and the coupling between sites was treated as the perturbation. He then introduced a disordered arrangement of the uncoupled sites, and showed for large values of the ratio of the on-site disorder strength and the coupling strength, the return probability of the electron Bloch wave from a

given initial site converges to a non-zero value. This conclusion was in contrast with the (naive) classical (diffusive) picture which was assuming that a particle in a random potential will perform a random walk and therefore its survival probability will decay to zero, in a fashion $\propto t^{-\frac{1}{2}}$. Such a picture gave an Ohmic decay[†] for the conductance, while Anderson's calculations indicated that conductance decays exponentially fast with the system size. This unexpected, exponential halt of propagation was later termed *Anderson localization* and during the last half of the century, has become one of the most fascinating subjects, with applications to various branches of physics [69]. Anderson localization was originally discussed in the frame of electron propagation, although at the beginning of the 70s it was realized that Anderson localization is a phenomenon based on destructive wave interferences [70]. As such, it ought to be observable in any system of a wave nature, irrespective if the wave system is classical or quantum. It turned out, in fact, that Anderson localization within electronic systems is extremely difficult to observe, due to electron-electron or electron-phonon interactions which cause the waves to decohere quickly. A much more promising experimental avenue in observation of Anderson localization is via photonic systems. Optical localization is governed by the Ioffe-Regel criterion [71]

$$\frac{\lambda}{l_m} \sim 1 \tag{5.1}$$

[†]As a reminder, Ohmic conductance decay is $\sigma \sim L^{-1}$, where σ is the conductance (inverse resistance), and L is the system length (wire length).

in which a mean free path of l_m (*i.e.* the average distance between two scattering events) is on the same order of the radiation wavelength, λ. The precursor to complete Anderson localization is termed weak localization, and is governed by the condition $\lambda/l_m \ll 1$. Weak localization is illustrated in Fig.(5.1). Optical weak localization is accompanied by an enhanced backscattering of light, but nevertheless, weak localization is a perturbative effect to the classical diffusive picture. In the Anderson localized regime, there is an exponential decrease in the conductance as the sample thickness increases. The medium therefore effectively undergoes a phase transition, passing from the macroscopically diffusive regime to the localized regime. Localization can therefore be characterized by two quantities - the disorder strength (present in l_m), and the wavelength.

Localization remained largely theoretical for several years. It was shown to exist for all disordered one-dimensional (1D) systems, and also within 2D systems, in which a single parameter scaling theory [72] was developed; the single parameter being a dimensionless conductance (the Thouless conductance) of

$$g(N) = \delta E_{Th}/\Delta, \tag{5.2}$$

dependent on the system size, N. Above, Δ is the mean level spacing, and the variable δE_{Th} is the *Thouless energy* - defined as the geometric mean of energy level fluctuations that occur when boundary conditions are changed between periodic & anti-periodic. The scaling of this parameter then was found to have a

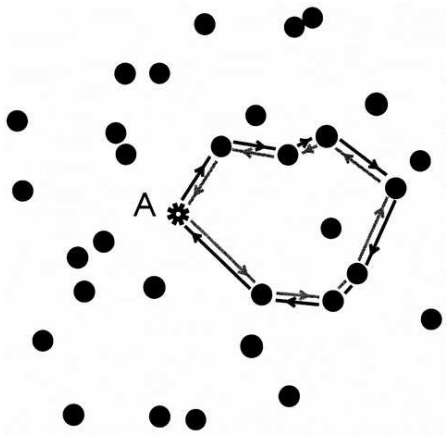

Figure (5.1): Weak localization due to multiple scattering. A wave source at point A is placed in a field of random scatterers, represented by black circles. The wave propagates along random paths, of which many may return to the initial point A. For a given propagation path, there are actually two opposing directions which the propagation can travel along, shown by the arrows in the paths. The phases of the wave gained during the propagation is the same for both directions - therefore the two directions constructively interfere to give a higher probability of the wave at A, as opposed to random paths that are dispersed throughout the sample. This effectively lowers the mean free path of the wave. With the addition of more scatterers, these closed paths 'tighten up' - and one can observe the wave eventually becoming trapped within the scatterers. This occurs where the separation between the scatterers is much less than the wavelength, $\lambda/l_m \ll 1$.

differential behavior of

$$\frac{d\ln g}{d\ln N} = \beta(g) \tag{5.3}$$

In $d > 2$ systems, the above scaling theory allows localization above some critical disorder strength - leading to a metal-insulator phase transition and critical states [73]. This case will be discussed further in Chapter 7, but here we shall limit the discussion to localized and diffusive systems that are strictly 1D/quasi-1D.

The wave nature of localization has drawn interest in the past two decades, par-

ticularly its application to classical waves. Despite enormous efforts by various research groups in measuring Anderson localization, it took nearly 40 years to observe localization phenomena beyond any doubt. A decisive step done was the use of classical wave systems, such as optics and microwave experiments, which allow a detailed study of the Anderson localization, undisturbed by the previously-mentioned interaction effects that plague electron propagation. Initial experiments in observing photon localization [74] faced the problem of separating localization from absorption, which acts as an additional source of exponential decay in electromagnetic wave propagation. A solution to the absorption problem was proposed [75–77] in the study of the relative size of fluctuations of certain transmission quantities. Clear evidence of localization in a 'quasi-1D'[†] microwave waveguide[‡] with randomly distributed dielectric or metallic spheres was found [75–77]. This powerful approach however does not allow a transport view from dynamical perspectives, nor does it make a direct contact with the original ideas of Anderson theory, which suggest probing localization by means of the sensitivity of the system properties against small perturbations [78]. It was this suggestion that led our focus to the sensitivity of wave dynamics to external perturbations, *i.e.* fidelity, as a possible localization probe.

[†]'Quasi-1D' systems are two or three dimensional systems in which only one of the dimensions (width, length, height) is larger than the wavelength, and therefore wave propagation is confined along the largest dimension.

[‡]A similar microwave waveguide system will be used in the next chapter.

5.2 Recent Experiments on Anderson Localization

Figs. (5.2-5.4) display three representative experimental localized observations in classical systems. In Fig. (5.2), a disordered system is created [79] by brazing together into a long cylindrical geometry metal spheres that are randomly arranged, seen inset. The cylinder is then lowered into a tank of water. A small ultrasonic transducer is placed at one end of the cylinder, and it excites the media with acoustic waves of a given frequency. At the other end of the sample, a miniature hydrophone (smaller than the acoustic wavelengths) scans across the sample, measuring the intensity of the transmitted acoustic wave. The main portion of the subfigure shows the scans for different frequencies, one above the Ioffe-Regel criterion on the left (*i.e.* > 1), and one below the criterion (< 1) on the right. For the frequency above the criterion, the acoustic wavefront is seen to diffuse across the transverse directions of the sample; such a spread and diffuse wave is called *extended*, or *delocalized*. For the frequency below the criterion, sharp peaks are observed in the intensity of the acoustic wavefront, yielding a *localized* wave - this is especially apparent if one notes the colormap scaling between the two cases. Because the observation is seen in the transverse wavefront and the longitudinal length is orders of magnitude larger than the wavelength such an observation is called *transverse localization*.

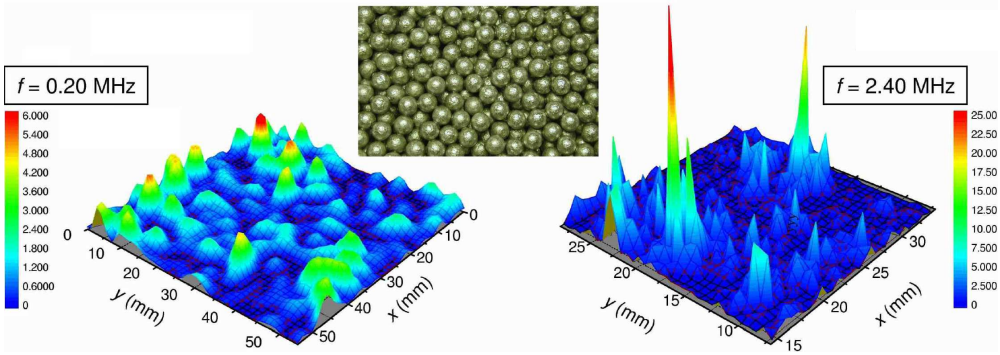

Figure (5.2): Anderson localization in an acoustic system. An acoustic disordered system created by brazed metal spheres, inset, is placed into a water tank. Acoustic waves are excited by an ultrasonic transducer at one end, and the transmitted intensities are measured by a hydrophone at the other. For a frequency below the Ioffe-Regel criterion, a diffusive wave is seen in the left. For frequencies above the criterion, localization is observed on the right. Images taken from [79].

Another experiment [80] that observes transverse localization is seen in Fig. (5.3). In this system, the mechanics are optical. A photorefractive crystal of SBN:60 ($Sr_{0.6}Ba_{0.4}Nb_2O_6$) acts as the medium. An interference pattern between three lasers is mapped into a photorefractive hexagonal lattice within the crystal via optical induction, shown on the left. Disorder can be controlled by passing one of the interfering lasers through a speckle plate. An incident laser at one end of the crystal propagates and spreads through the lattice. The transmitted light is then imaged with a CCD camera. For an ordered crystal, the light propagates throughout the crystal, and the hexagonal pattern is seen in the transmitted light, shown in the middle portion of the subfigure. However, for strong disorder, a localization of the transmitted light is seen in the right portion of the figure.

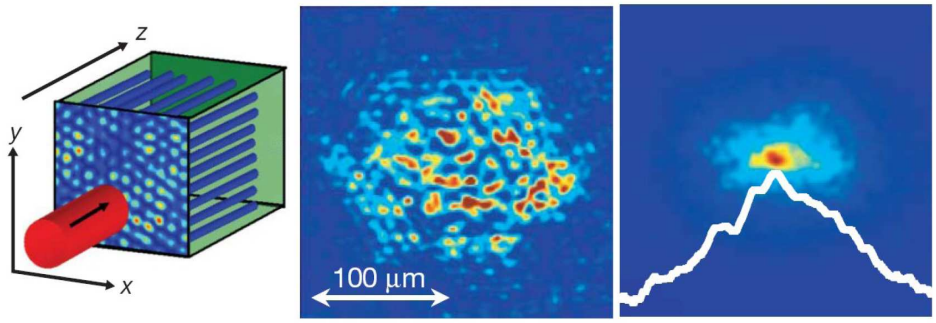

Figure (5.3): Anderson localization in an optical system. An optical hexagonal lattice is created by optical induction of a laser interference into a SBN:60 photorefractive crystal, on the left. Disorder is controlled by passing one of the inducing lasers through a speckle plate. An incident laser (the red cylinder on the left) propagates and is imaged by a CCD camera on the other end of the crystal. An ordered crystal results in diffused light that shows the hexagonal crystal structure, in the middle. For stronger disorder, the transmitted light is localized, shown in the right. The white line represent a logarithm of a horizontal cut through the center, and clearly displays an exponential envelope (see next section). The color scaling goes from blue to red, for minimum to maximum. Images taken from [80].

A third experiment [81] that observes localization is strongly related to the system from the previous chapter. In this case, we have an optical lattice formed, but disorder is created in the lattice in a similar fashion to the past experiment - one of the lasers is passed through a speckle plate. A Bose-Einstein condensate of alkali atoms is formed and trapped at a single site at time $t = 0$. The density of the BEC can then be imaged, and is shown in the upper portion of Fig.(5.4).

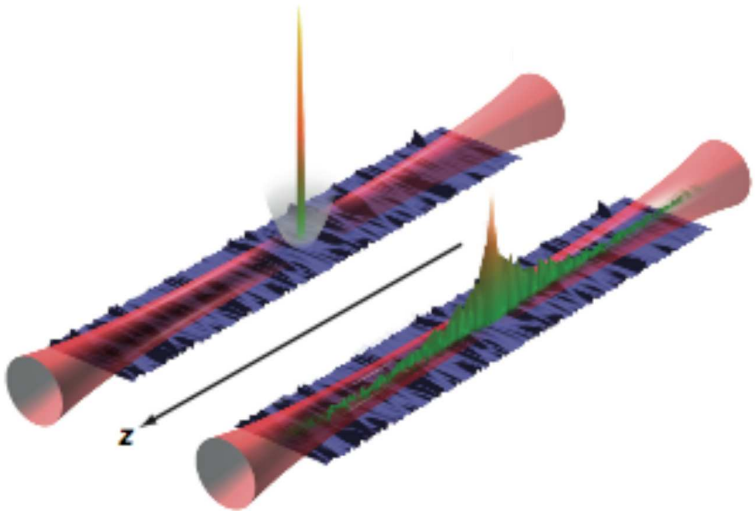

Figure (5.4): Anderson localization in an atomic matter wave system. An optical lattice is formed by two counter-propagating lasers. Disorder is introduced by passing one laser through a speckle pattern. A BEC is loaded and trapped at a single site and its density is measured, upper figure. The magnetic trap is turned off in the z-direction, and the BEC is allowed to propagate in the lattice. The disorder present in the lattice allows the density to spread, but keeps majority of the BEC trapped at the initial site. Figure taken from [81].

At $t > 0$, the magnetic trap in the longitudinal (z) direction is turned off, and the BEC is allowed to expand across the lattice. The density does spread, but the majority of the condensate stays localized by the disorder. This experiment is pathological from the other two, in that a second mechanism of trapping is present in the nonlinear interactions of the bosons, which opens new and exciting directions of research. However, Anderson localization is still observed for very weak boson-boson interactions.

5.3 Modeling Localization

The standard model in solid state physics that describes electron transport on a disordered lattice is the *Anderson tight-binding model*. It involves - apart from a coupling term between neighboring lattice sites - an on-site random potential. The corresponding Hamiltonian is

$$\hat{H} = \sum_{n=1}^{N} \epsilon_n |n\rangle \langle n| + k \sum_{\substack{n=1 \\ m=n\pm 1}}^{N} (|n\rangle \langle m|) \tag{5.4}$$

where $|n\rangle$ is the Wannier basis state localized at the n^{th} site, N is the number of sites, k is the tunneling probability to the neighboring sites, and ϵ_n is the onsite disorder, typically drawn from a uniform distribution of $[-\frac{W}{2}, \frac{W}{2}]$.

5.3.1 An RMT Approach: The Banded Random Matrix

A way to model quasi-1D disordered systems with b propagating channels is provided by random matrix theory modeling. In the early 90s, it was shown [82] that *Banded Random Matrices (BRM)* can be mapped exactly to the 1D non-linear σ model, which is the appropriate field theoretical model describing quasi-1D disordered systems. Within BRM, elements are drawn from a Gaussian sequence that

is subject to a zero mean, but a variance of

$$\left\langle |H_{nm}|^2 \right\rangle = \begin{cases} 1 + \delta_{nm}, & |n-m| \leq b \\ 0, & |n-m| > b \end{cases} \tag{5.5}$$

The BRM is then very similar to the standard GOE matrix (Chapter 2), but only across a 'band' in the matrix, characterized by the width parameter b - elements outside of the band are zero. The parameter b corresponds to the number of channels in a quasi-1D wire geometry.

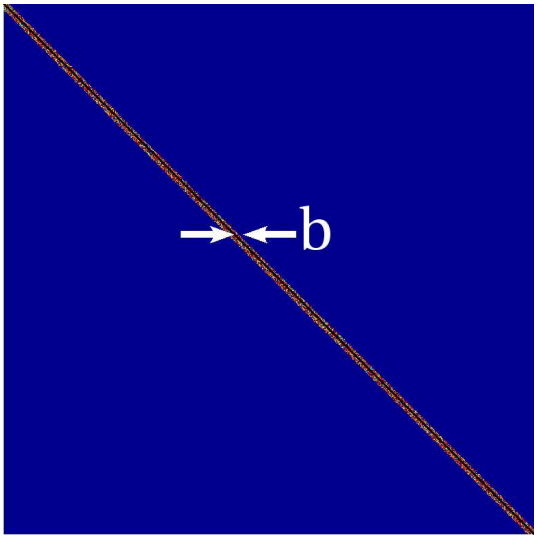

(a) Banded Random Matrix, $N = 1000, b = 10$.

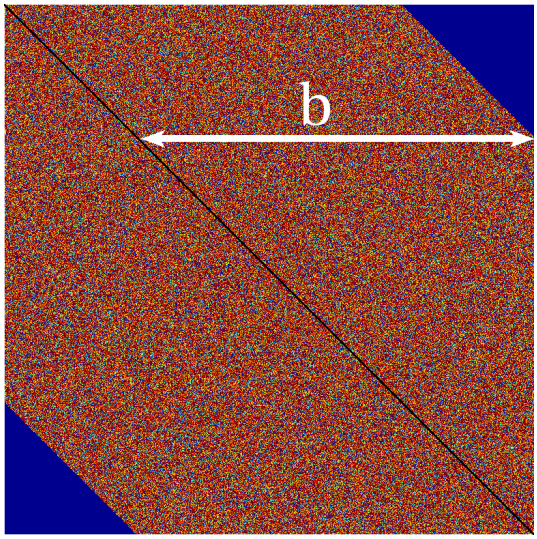

(b) Banded Random Matrix, $N = 1000, b = 750$.

Figure (5.5): Absolute value of the elements of two banded random matrices, with the color ranging from blue (zero) to red. The elements all within a given distance (bandwidth, b) from the diagonal (black) follow a Gaussian distribution. All elements outside of the band are zero.

Alternatively, b can be considered to be the previously mentioned mean free path, l_m. If $b \geq N$, the system is said to be in the *ballistic regime* - which gives a GOE limit to the BRM model. The idea of a banded matrix is illustrated by Fig. (5.5).

The localization properties of the eigenfunctions were investigated both analytically [83–85] and numerically [86–91]. It was specifically found that for a finite N-dimensional sample with $b < N$, the localization properties of the wavefunctions are determined by the parameter

$$\Lambda = b^2/N \tag{5.6}$$

In the case of $\Lambda \ll 1$, the eigenvectors associated with the Hamiltonian, Eq.(5.4), show on average an exponential decay around some central site n_0, *i.e.*

$$\left\langle |\psi_n|^2 \right\rangle = \exp\left(-\frac{|n-n_0|}{l_\infty(E)}\right) \tag{5.7}$$

where $l_\infty(E)$ is the width of the exponential, called the *localization length*. It is used to quantify the degree of localization of the system, and is energy-dependent. Within the BRM, the localization length was calculated [89]

$$l_\infty(E) = \frac{2}{3}\left[1 - \left(\frac{E}{\sqrt{8b}}\right)^2\right] b^2 \sim b^2 \tag{5.8}$$

In the opposite limit of $\Lambda \gg 1$, the wavefunctions are extended throughout the

sample. This case corresponds to a delocalized (diffusive) system. The transition from one limit to the other was found [87] to be controlled by the parameter Λ. The analysis was performed either by studying the scaling properties of various moments of the wavefunctions or by probing the scaling properties of scattering characteristics, like the delay time (see Appendix A). In the former case (localized), the most popular of these moments is the *inverse participation number (IPN)*. For a discrete system

$$P_2 = \sum_{n=1}^{N} |\psi_n|^4 \tag{5.9}$$

The IPN gives an estimation of the inverse "effective volume" that a wavefunction occupies. For the two limits, the IPN behaves as

$$P_2 \sim \begin{cases} N^{-d}, & \Lambda \gg 1 \\ l_\infty^{-1}, & \Lambda \ll 1 \end{cases} \tag{5.10}$$

The two eigenstates from the BRMs in Fig.(5.5) are shown in Fig. (5.6). The case of $\Lambda \gg 1$ indeed displays a diffusive wavefunction on the right. The case is checked by plotting the expectation from IPN (for $d = 1$) of $\psi_n \sim 1/\sqrt{N}$ in the dashed line. The 'localized' case on the left exhibits the trademark signature of Anderson localization - the exponential envelope, appearing as a straight line on a semilogarithmic scale. A best fit to Eq. (5.7) gives a localization length of ~ 8.5, plotted in the dashed lines. Therefore, BRMs in the above limits are good models for localization/delocalization.

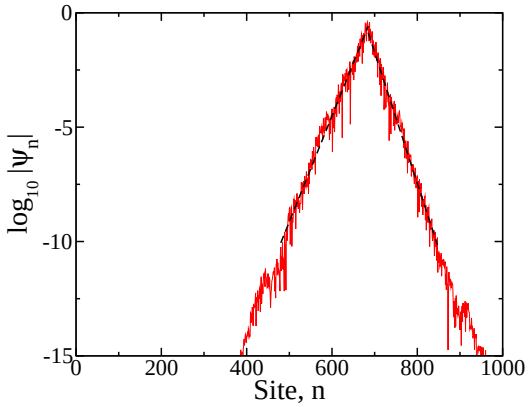

(a) Eigenstate in the limit $\Lambda \ll 1$ (localized), for $N = 1000, b = 10$.

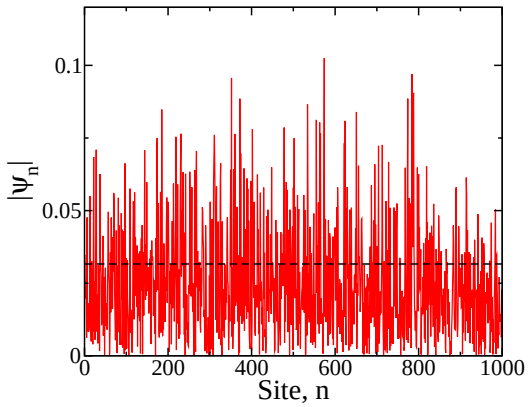

(b) Eigenstate in the limit $\Lambda \gg 1$ (diffusive), for $N = 1000, b = 750$.

Figure (5.6): Eigenstates of the BRMs in Fig.(5.5). The diffusive limit on the right displays an eigenstate in red. The IPN expectation of $|\psi_n| \sim 1/\sqrt{N}$ is plotted as a dashed line. The localized limit on the left displays a localized eigenstate. In this case, localization manifests as an exponential envelope with a rate given by the inverse localization length. To best fit, the dashed lines show an exponential behavior with a localization length of ~ 8.5.

The importance of the scaling parameter Λ was also recognized in the framework of level statistics. For $\Lambda \gg 1$ (diffusive), one gets a GOE type of level statistics, while for $\Lambda \ll 1$ (localized), one recovers an uncorrelated Poissonian spectrum - which is characteristic of systems in Anderson localization [87]. The level statistics for BRMs are verified within Fig. (5.7), for the two limits. Poissonian distributions are indeed observed in the localized limit, while Wignerian statistics are observed in the diffusive limit.

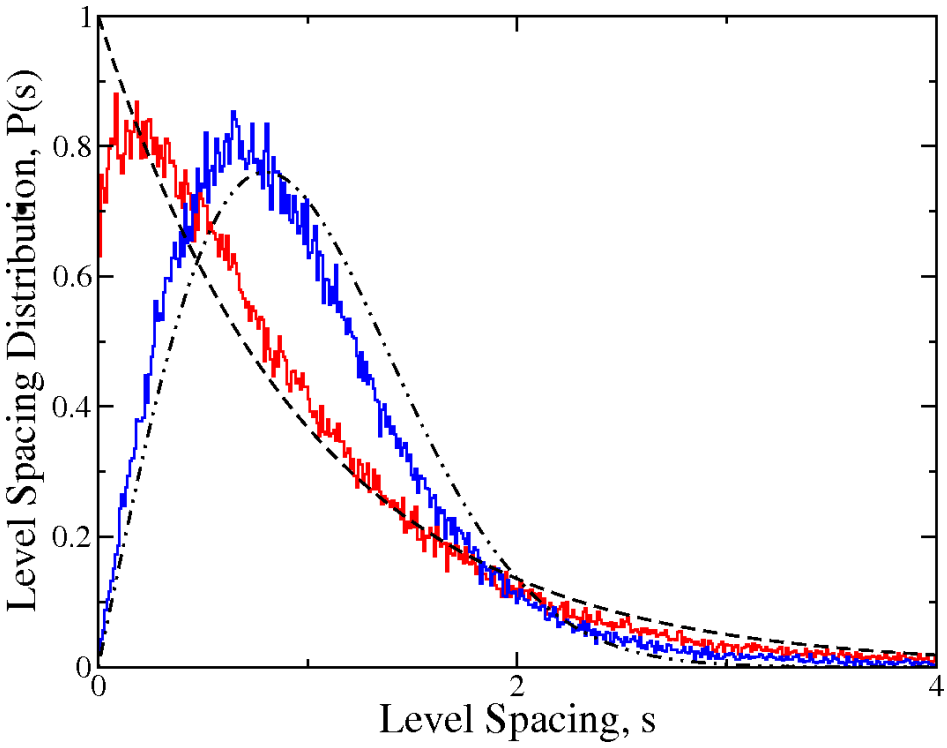

Figure (5.7): The level spacing distribution for two Banded Random Matrices, $N = 2500$, $b = 5$ (localized limit - red), $b = 750$ (diffusive limit - blue). The dotted-dashed line is the Wignerian GOE distribution from Eq. (2.28), which the diffusive limit approaches. The dotted line is the Poissonian distribution, which the localized limit approaches.

5.4 Fidelity in the BRM

We will now turn to the theoretical calculation of the fidelity decay in the framework of a BRM model. As a reminder, the fidelity is formally defined as

$$F(t) = |f(t)|^2 = |\langle\psi_0| \exp(-iH_0 t/\hbar) \exp(iH_\lambda t/\hbar) |\psi_0\rangle|^2 \tag{5.11}$$

where $f(t)$ is the fidelity amplitude and $|\psi_0\rangle$ is a generic initial state. $H_\lambda = H_0 + \lambda V$ is a one-parameter family of Hamiltonians; H_0 is an unperturbed Hamiltonian and a perturbation (of strength λ)[†] is represented by λV , where $\left\langle |V_{nm}|^2 \right\rangle = 1$. The fidelity was further evaluated using a RMT modeling for H_0 and V. For the diffusive limit ($\Lambda \gg 1$), H_0 and V are modeled by GOE matrices. In the localized limit ($\Lambda \ll 1$), H_0 and V are modeled with BRMs with a bandwidth of b. Below, we present the outcome of our theoretical calculations for the two limiting cases.

5.4.1 The Diffusive Limit ($\Lambda \gg 1$)

The level statistics within the extended limit closely follow those seen in full GOE matrices, as Fig. (5.7) showed. Therefore, the fidelity in the extended limit can be approximated by the standard GOE fidelity seen in Eq.(3.28). As a reminder, the GOE result is

$$F(t) \sim \exp\left(-(2\pi\lambda)^2 \left[\frac{t^2}{\nu} + \frac{t}{2} + \int_0^t d\tau \int_0^\tau d\tau' b_2(\tau')\right]\right) \tag{5.12}$$

Fig. (5.8) shows the numerical fidelity for $N = 1000, b = 75$ as circles. The solid line displays the best fit of the data to Eq.(5.12), and a good match is seen in the region of interest $t < t_H$.

[†]Note that previous chapters, we've used x and δk for the perturbation strength. Here, we will use λ to represent the perturbation strength.

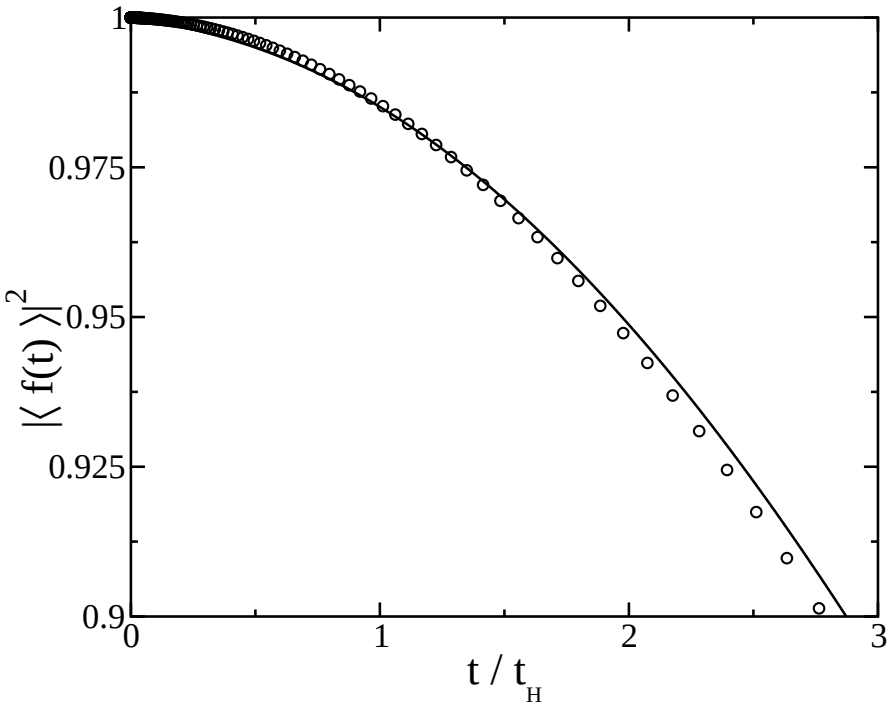

Figure (5.8): The numerical fidelity (circles) vs. the analytical linear response approximation (solid line), in the standard perturbative regime. The system parameters are $N = 1000, b = 750, \lambda = 0.001$. There is an additional ensemble averaging over 100 realizations of V. A good match is seen between the numerics and the linear response approximation of Eq.(5.12), within the region $t < t_H$.

5.4.2 The Localized Limit ($\Lambda \ll 1$)

In Chapter 3 [see discussion of Eq.(3.36)] we have derived an expression for the fidelity amplitude which reads

$$f(t) = \sum_{n,m,k} c_n^* c_k T_{mk}^* T_{nm} \exp[i\omega_{mn} t] \tag{5.13}$$

where $T_{nm} = \langle n^{(0)}|m\rangle$ is the LDoS amplitude, $\omega_{mn} = (E_m - E_n^{(0)})/\hbar$, and c_k is the initial state expansion coefficient in the unperturbed basis, $c_k = \langle \psi_0|k^{(0)}\rangle$. Taking an ensemble average yields

$$\begin{aligned} \langle f(t)\rangle &= \left\langle \sum_{n,m,k} c_n^* c_k T_{mk}^* T_{nm} \exp[i\omega_{mn}t] \right\rangle \\ &\approx \sum_{n,m,k} \langle c_n^* c_k\rangle \langle T_{mk}^* T_{nm}\rangle \exp[i\langle\omega_{mn}\rangle t] \end{aligned} \tag{5.14}$$

in which the above distributive property of the average comes from a RMT conjecture that eigenstates and eigenenergies are statistically independent (uncorrelated). Firstly, let us discuss the expansion coefficients

$$c_n^* c_k = \langle \psi_0|n^{(0)}\rangle \langle k^{(0)}|\psi_0\rangle = \left(\sum_i \psi_{0,i} n_i^{(0)}\right) \cdot \left(\sum_j \psi_{0,j} k_j^{(0)}\right) = \sum_{i,j} \psi_{0,i}\psi_{0,j} n_i^{(0)} k_j^{(0)} \tag{5.15}$$

Under the ensemble average, we get

$$\langle c_n^* c_k\rangle \approx \sum_{i,j} \langle \psi_{0,i}\psi_{0,j}\rangle \left\langle n_i^{(0)} k_j^{(0)}\right\rangle \tag{5.16}$$

where $\psi_{0,i}$ is the i^{th} component of the initial wavefunction in a Wannier basis, and $n_j^{(0)}$ is the j^{th} component of the n^{th} eigenstate of $\hat{H}_0$, in the Wannier basis. For localized eigenstates of $\hat{H}_0$, the average overlap between the localized states is fairly negligible, unless the two eigenstates are either (a) the same eigenstate ($i = j$), or (b) have their localized peak within the localization length of another

eigenstate. This yields for the second average

$$\left\langle n_i^{(0)} k_j^{(0)} \right\rangle = \delta_{n,k}\delta_{i,j} l_\infty^{-1} \delta(i \leq l_\infty) \tag{5.17}$$

Placing this back into the expansion coefficient average contracts the sum as

$$\begin{aligned} \langle c_n^* c_k \rangle &\approx \sum_{i,j} \langle \psi_{0,i}\psi_{0,j} \rangle \, \delta_{n,k}\delta_{i,j} l_\infty^{-1} \delta(i \leq l_\infty) \approx \frac{\delta_{n,k}}{l_\infty} \sum_{j \leq l_\infty} |\psi_0, j|^2 \\ &\approx \sigma \delta_{n,k} \end{aligned} \tag{5.18}$$

where in the last step we use the notation $\sigma = l_\infty^{-1} \sum_{j \leq l_\infty} |\psi_0, j|^2$. We substitute this result back into the average fidelity amplitude, to eventually get

$$\begin{aligned} \langle f(t) \rangle &\approx \sigma \sum_{n,m,k} \delta_{n,k} \langle T_{mk}^* T_{nm} \exp[i\omega_{mn} t] \rangle \\ &\approx \sigma \sum_{n,m} \langle P_{nm} \rangle \exp[i \langle \omega_{mn} \rangle t] \end{aligned} \tag{5.19}$$

where $P_{nm} = |T_{mn}|^2$ is the LDoS kernel of Eq.(3.30). The fidelity amplitude then reads

$$\langle f(t) \rangle \approx \sum_{n,m} \langle P_{nm} \rangle \exp[i \langle \omega_{mn} \rangle t] \tag{5.20}$$

We will refer to this as the *localized fidelity*. We now proceed by evaluating Eq.(5.20) for various perturbation regimes. We have incorporated the analysis of the evaluation of the various perturbation limits within Appendix B.4, for clarity. The methodology used is an LDoS analysis of Chapter 3.

Localized Fidelity in the Standard Perturbative Regime

For small perturbations, the LDoS kernel is delta-like, in that only levels within a mean level spacing apart mix. Numerically, we calculate the LDoS kernel - shown as the black line within Fig.(5.9) - for $N = 1000, b = 10, \lambda = 0.001$, and compare it to the FOPT approximation of the Eq.(3.41), beautifully matching in red. The mean level spacing is on the order of the screen pixel. For such small perturbations, numerics follow expectation that the LDoS is delta-like. Using a

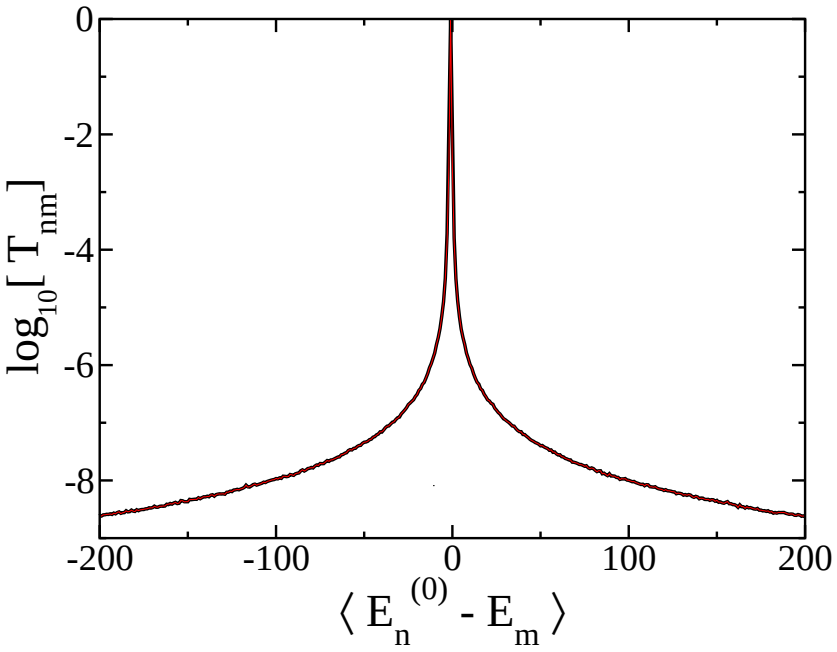

Figure (5.9): LDoS kernel for $N = 1000, b = 10, \lambda = 0.001$ (standard perturbative regime). The black line is the numerical LDoS kernel, while the red line is the FOPT approximation. The mean level spacing is on the order of a pixel.

delta approximation, Eq.(5.20) contracts across m to yield

$$\begin{aligned} f(\tau = t/\hbar) &\approx \sum_n \exp\left[i(E_n - E_n^{(0)})\tau\right] \\ &\approx \sum_n \exp[i\lambda\nu_n\tau] \end{aligned} \tag{5.21}$$

in which we have used the definition of the *level velocity*[†]

$$\nu_n = \frac{(E_n - E_n^{(0)})}{\lambda} \tag{5.22}$$

Turning the sum into a weighted integral over level velocities one gets

$$f(\tilde{\tau} = \lambda\tau) \approx \int_0^\infty P(\nu) d\nu \ \exp(i\nu\tilde{\tau}) \tag{5.23}$$

in which $P(\nu)$ is the level velocity probability distribution function (LVPDF).

The LVPDF has been studied thoroughly using both RMT [92] and field-theoretical techniques [93]. In the case of a BRM the LVPDF - illustrated in Fig. (5.10) - was found to be [92]

$$P(\eta) = \frac{\pi}{6} \frac{\coth\left[\frac{\pi\eta}{\sqrt{6}}\right] - \sqrt{6}}{\sinh^2\left[\frac{\pi\eta}{\sqrt{6}}\right]} \tag{5.24}$$

where $\eta = \nu/\sigma_\nu$ is the variance-rescaled level velocity. Furthermore, it has been shown that the variance of the level velocity within the localized limit is equivalent to the root of the IPN and the bandwidth, $\sigma_\nu = \sqrt{P_2} = b^{-1}$.

Taking the fourier transform of Eq. (5.24) yields the following result for the fidelity amplitude

$$f(t) = (\alpha t)^2 \operatorname{csch}(\alpha t) \tag{5.25}$$

[†]The term 'level velocity' comes from a Pechukas-Yukawa approach to level dynamics, in which the parametric variable is treated as 'time'. The parametric evolution of the levels can then be interpreted in the 'standard' context of velocites, accelerations (called 'curvatures' in context of level dynamics), and forces within the system.

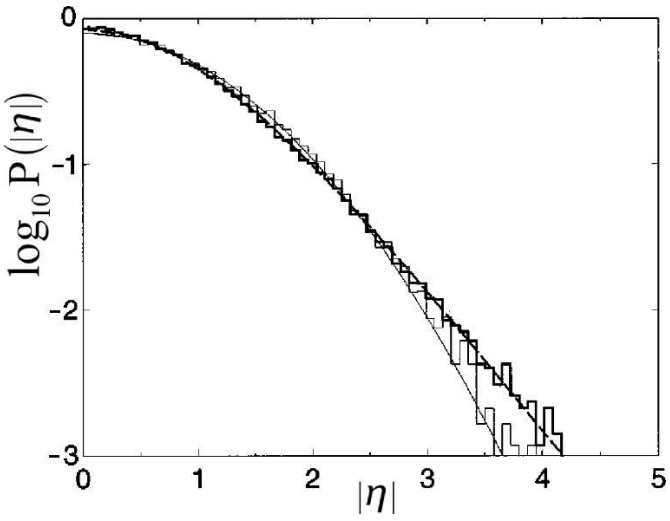

Figure (5.10): The probability distribution function for the absolute level velocities (LVPDF) of two BRMs, one in the localized limit (thick histogram) and one in the extended limit (thin histogram). The extended limit LVPDF is shown to follow the Wignerian statistics (thin dashed line) of Eq.(2.28). The localized limit LVPDF is shown to follow the localized statistics (thick dashed line) of Eq.(5.24). Figure taken from [92].

in which α contains all the rescaling variables used

$$\alpha(\lambda) = \lambda\sqrt{1.5P_2} \tag{5.26}$$

The fidelity is then calculated numerically, and fit to the two Eqs.(5.12,5.25). The results for various b values (all for $\Lambda \ll 1$) are shown in Fig. (5.11). The fitting parameter α is extracted, and compared to the $\sqrt{P_2}$ found directly from the eigenstates of $\hat{H}_1$. It is seen that the novel result of Eq.(5.25) better fits the numerical data than the full GOE result of Eq.(5.12). Additionally, the $\sqrt{P_2}$-dependence in the fit parameter α is verified, suggesting Eq.(5.25) as the model to use for localized fidelity in the standard perturbative regime.

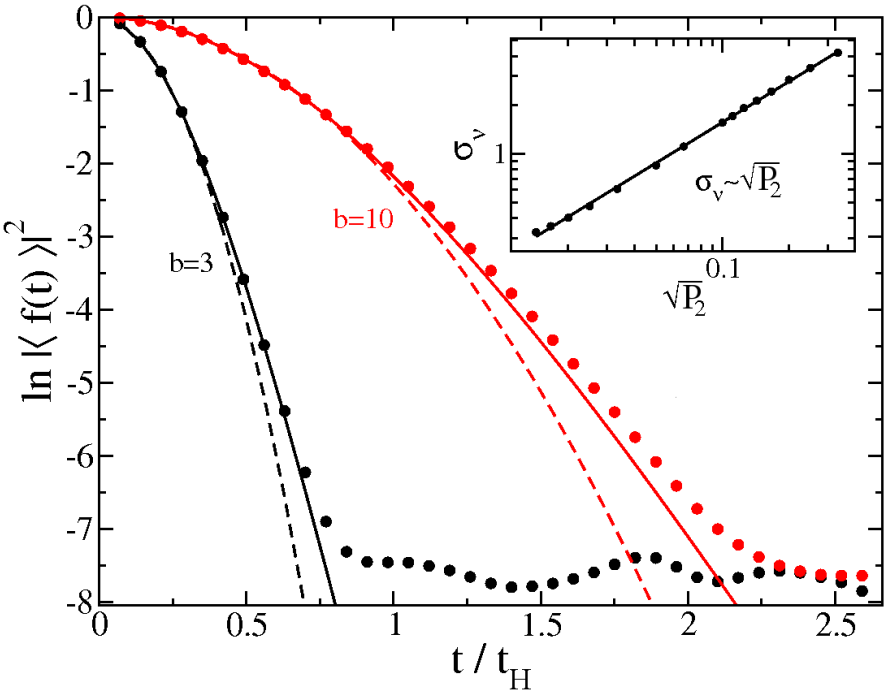

Figure (5.11): The numerical fidelity from Eq.(5.13) for $N = 1000, \lambda = 0.001$ (standard perturbative regime) is plotted for two different localized bandwidths, $b = 3$ (red), 10 (black). The numerical results are the circles, the solid lines are best fits to Eq.(5.25), and the dashed lines are the best fits to Eq.(5.12). A better fit is observed for Eq.(5.25). Inset: The variance parameter σ_ν is extracted from the fitting parameter α for different localized bandwidths, and plotted against $\sqrt{P_2}$, calculated directly from the eigenstates. The linear relation $\sigma_\nu = \sqrt{P_2}$ for localized eigenstates is verified - the straight line is a best linear fit.

Localized Fidelity in the Wigner (FGR) Regime

In the Wigner (FGR) regime, mixing occurs beyond neighboring levels out to some bandwidth Γ, yielding a LDoS kernel that is Lorentzian-like, Eq.(3.43). We numerically calculate the LDoS for the Wigner (FGR) regime, and present the

results in Fig.(5.12).

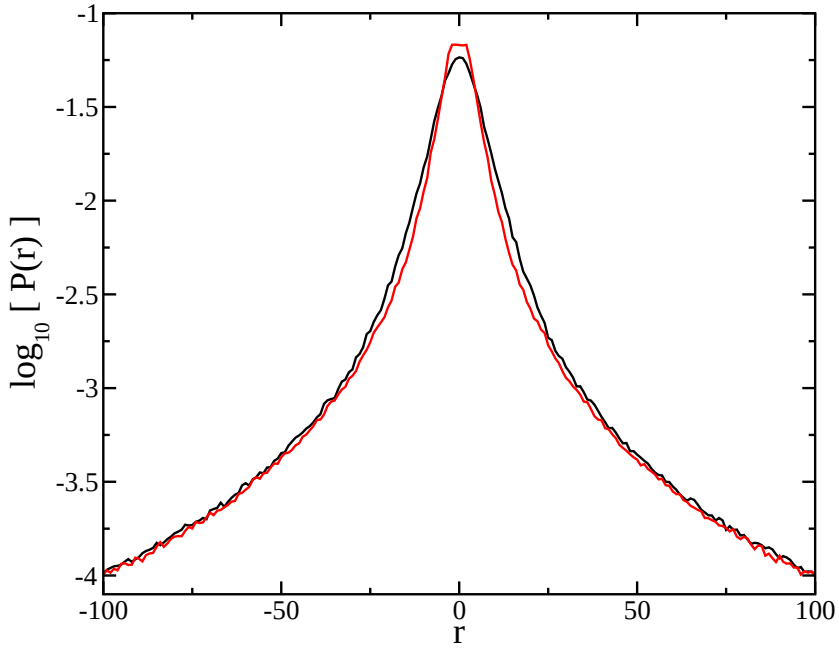

Figure (5.12): LDoS kernel for $N = 1000, b = 10, \lambda = 0.1$ [Wigner (FGR) regime]. The black line is the numerical LDoS kernel, while the red line is the PRT approximation. Both are Lorentzian curves of width Γ, found from normalization of the PRT approximation. The variable $r = \left\langle E_n^{(0)} - E_m \right\rangle / \Delta$ is used. In order to get a scale, the mean level spacing is on the order of a major tickmark width.

Further analysis of the fidelity in Eq.(5.20) gives

$$\langle f(t) \rangle \approx \sum_r P(r) \exp\left[ir\tilde{\tau}\right] \tag{5.27}$$

in which $\tilde{\tau} = \Delta t/\hbar = t/t_H$ and $r = \langle E_m - E_n^0 \rangle / (\hbar\Delta)$. For the Lorentzian line-

shape of $P(r)$, a Fourier transform will yield

$$\langle f(\tilde{\tau} = t/t_H)\rangle \approx \exp\left[-\Gamma\tilde{\tau}\right] \tag{5.28}$$

The numerical fidelity in the Wigner (FGR) regime is shown in Fig.(5.13) as the black line. For times $t > t_H$, a long exponential decay is observed.. The red line in Fig.(5.13) is a best fit of the numerical fidelity to the exponential result of Eq.(5.28).

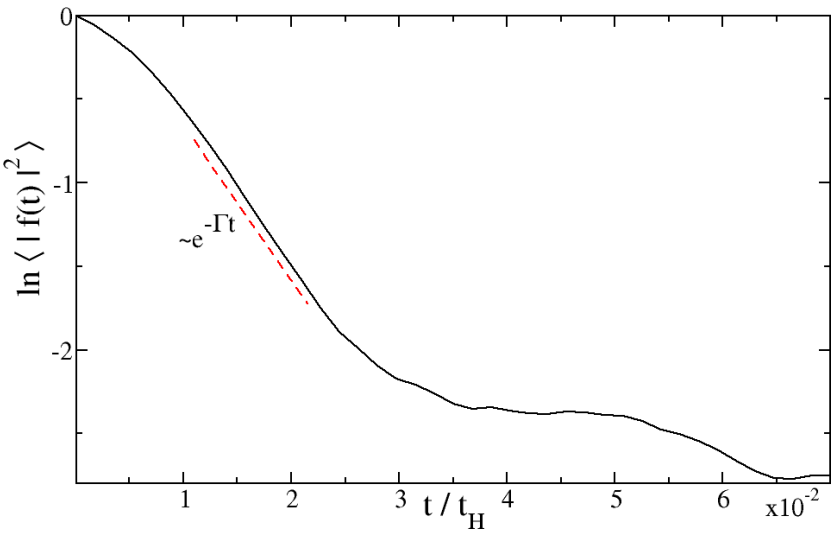

Figure (5.13): The numerical fidelity from Eq. (5.13) for $N = 1000, \lambda = 0.1$ [Wigner (FGR) regime] is plotted for the localized bandwidth of $b = 10$ (black). The red line is a best fit to Eq.(5.28). The fit is offset slightly to the left of its range.

5.5 Conclusion

In summary, we have utilized banded random matrices as models for diffusive states ($\Lambda \gg 1$) and as models for localized states ($\Lambda \ll 1$). Analytical calculations with appropriate approximations yield a novel fidelity decay for localized systems in the standard perturbative regime, seen in Eq.(5.11), and the usual exponential decay in the Wigner (FGR) regime. Numerical calculations using banded random matrices verify our analytical findings - in the next chapter, experimental data from a laboratory will be used to verify the same analytical findings.

Chapter 6

Probing Anderson Localization via Fidelity: Experiment

> *It doesn't matter how beautiful your theory is, it doesn't matter how smart you are. If it doesn't agree with experiment, it's wrong.*
>
> -Richard Feynman

In this chapter, we wish to test the theoretical results that were derived in the previous chapter - as far as the behavior of fidelity decay in disordered media, versus experimental measurements with disordered microwave cavities. In order to perform the comparison, we must introduce a new notion of fidelity,termed *scattering fidelity*, which shows however the same temporal behavior as the fidelity discussed in the previous chapters. The structure of the chapter is as follows: within the first section, we will discuss the experimental microwave setup. In the next section, we will discuss the characterization of diffusive vs. localized frequency regimes, via transport measurements. We will then present the measure

of scattering fidelity, in which we will also briefly discuss how scattering fidelity addresses the issue of absorption. Finally, we present the experimental scattering measurements for both the diffusive and localized frequency regimes, and compare to the theoretical results in the previous chapter. A connection is made between the theory and experiment via a scaling analysis of the dependency of decay rates on perturbative strengths, a point on which we will conclude the chapter.

6.1 Experimental Setup

Fig.(6.1) is a photograph of the microwave cavity that we have used in our experiments. It is a rectangular waveguide made of brass with brass bars at two ends closing the waveguide, with dimensions of 8 mm height, 10 cm width, and 100 cm long. One of the short wall-lengths is allowed to move, and a shift in the wall will play the role of a perturbation in this system. The moving wall and its driving motor mechanism is seen in the lower portion of Fig.(6.1). The cavity is filled with 186 brass cylinders with radius 5 mm. The brass cylinders are arranged in a random fashion - transparency film showing cylinder locations for a particular random realization can be seen taped to the side of the cavity in Fig.(6.1). The microwave TE modes that are excited in the cavity are transverse, and their wavelengths are such that the cylinders can be viewed as point scatterers. In additon the wavelengths are such that the cavity height and width are negligible, so that the cavity is considered to be quasi-one-dimensional (quasi-1D).

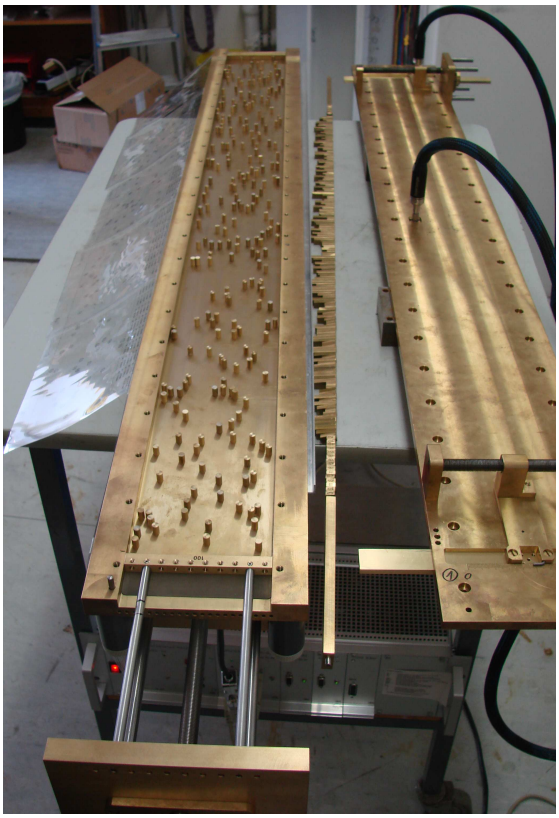

Figure (6.1): Photograph of the experimental microwave cavity filled with random scatterers. The top plate of the cavity can be seen at the right side, rotated by 180°. The point scatterers can be seen as small brass cylinders, randomly arranged inside the cavity. Transparency film taped to the left of the cavity help guide the setup of the cylinder random arrangement. One of the short walls is moveable, controlled by a stepper motor that is not pictured. The worm-gear mechanical control of the short wall can be seen on the lower section of the photograph. The small metal rackmount box on the lower shelf of the figure is the RS-232 computer control interface of the stepper motor. The metal bar of scatterers running up the center was for a separate experiment, and should be disregarded in this photograph.

The cavity is closed by a top plate that is screwed into place. Two BNC connections couple two microwave antennae into the cavity, one close to moving short wall (the "perturbed" antenna, denoted by index 1) and the other deep within the scatterers (the "bulk" antenna, denoted by index 2). Note that in Fig.(6.1), the top plate can be seen at the right side, rotated by 180°. Fig.(6.2) shows a side view of the top plate, in which one antenna can be seen protruding below. The bottom of the figure is roughly where the bottom of the cavity is located. The white coating over the antenna is a polymer transparent to microwaves whose purpose is to keeps the antenna aligned and protected.

Figure (6.2): A sideview of the top plate illustrating the depth of the antenna into the cavity. The bottom of the figure roughly corresponds to the bottom of the cavity. The white coating on the antenna is a thick, microwave-transparent polymer that that serves as protection and alignment for the antenna.

The beauty of an experimental microwave system is the combination of both source and detection present in a device developed for electrical network analysis in radio frequencies. The device is called a *vector network analyzer* (VNA), and is pictured in Fig.(6.3). Here, we use a commercial version of a VNA, the Agilent 8720ES, which can be controlled by a PC computer via a GPIB cable. The VNA consists of multiple BNC ports ("channels" in previous parlance) that a microwave cable can attach, seen in the lower portion of the image. After securing the top plate, we run cables from two channels of the VNA to the two antennae coupled to the inside of our cavity. The VNA then allows us to send in microwaves with a given frequency along a channel that emit from a given antenna into the cavity as plane waves. The Agilent 8720ES can send and receive frequencies of $3 - 12$ GHz at a 100 kHz resolution. The wave scatters about the cavity and quickly reaches a steady-state, at which point we measure the phase and magnitude at the two antenna positions. With the phase and magnitude, we can easily find the

two reflections $S_{11}(E), S_{22}(E)$ and the two transmissions $S_{12}(E)$, $S_{21}(E)$. The reflections/transmissions can be seen in Fig.(6.3) plotted as normalized impedences (Smith charts) in the Agilent LCD output. The resulting S-matrix elements are then ran back via the GPIB cable to the PC computer for digital storage and analysis.

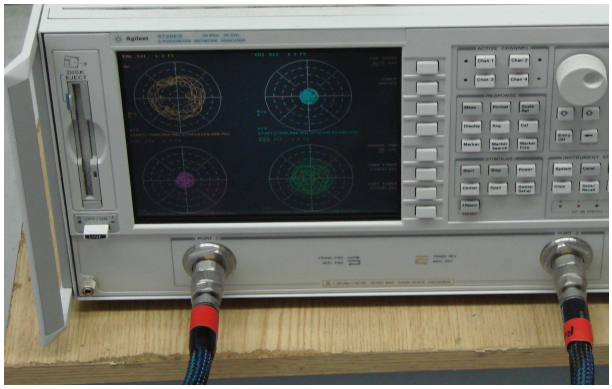

Figure (6.3): The Agilent 8720ES, a commercial vector network analyzer (VNA). Two microwave ports with cables running to the antennae are seen in the lower portion, and the resulting transmissions/reflections are plotted as impedence Smith charts in the VNA's LCD output, seen in the left. Not pictured is the GPIB data/control cable that transmits the scattering matrix elements to a PC computer for storage and analysis.

The perturbation that is applied to the system takes place by a shift in position of one of the shorter walls. This is controlled by the stepper-motor/worm-gear mechanical assembly that attaches to the lower wall within Fig.(6.1). For a given random ensemble, the wall is shifted by increments of $\delta w = 0.2\,\text{mm}$, up to a maximum wall shift of $w = 18.0\,\text{mm}$. We will later characterize the perturbation strength λ in relation to a dimensionless wallshift $w/\delta w$. Lastly, the whole experiment - including control of the stepper motor to shift the wall and the frequency

control/S-matrix measurement of the Agilent VNA - is automated by a C++ interface, custom built by Ulrich Kuhl. This results in a tidy experimental package in which one sets up an arrangement of scatterers, attaches the antennae, enters step size and frequency, and then hits 'Run' to start the process. A given realization takes roughly 16 hours to complete a scan through the frequency regime $3-12$ GHz at 100 kHz resolution. This was repeated for 15 different arrangements of the 186 scatterers, and the resulting raw data was processed using ITT's "IDL" programming language.

6.2 Diffusive & Localized Frequency Regimes: Transport Measures

6.2.1 Normalized Transmission Variances

First experiments showing photon localization [74] had the problem of separating localization from absorption, which can be another source of exponential decay of a propagating electromagnetic wave. Recall from the Ioffe-Regel criterion that the localization length is energy-dependent, and thus changes with the incoming frequency. How then to determine localization in an absorptive system? A solution to this problem was given by Chabanov & Genack [75–77] where they proposed to study the relative size of fluctuations of transmissions, in order to find signatures of localization. They found clear evidence of localization in a quasi-

one-dimensional (1D) microwave waveguide with randomly distributed dielectric or metallic spheres. The relative size of the transmission fluctuations is captured by the average variance of the normalized transmission, defined as $\sigma^2_{\tilde{T}} = \left\langle \mathrm{var}(\tilde{T}) \right\rangle$. Chabanov & Genack showed that a theoretical threshold between localized and diffusive fluctuations exists for multiple channels at the value $\sigma^2_{\tilde{T}} \sim 7/3$. We shall therefore follow a similar argument, and look for frequency regimes in which $\sigma^2_{\tilde{T}} > 7/3$. Our results are shown in Fig.(6.4). Since our experiment does not

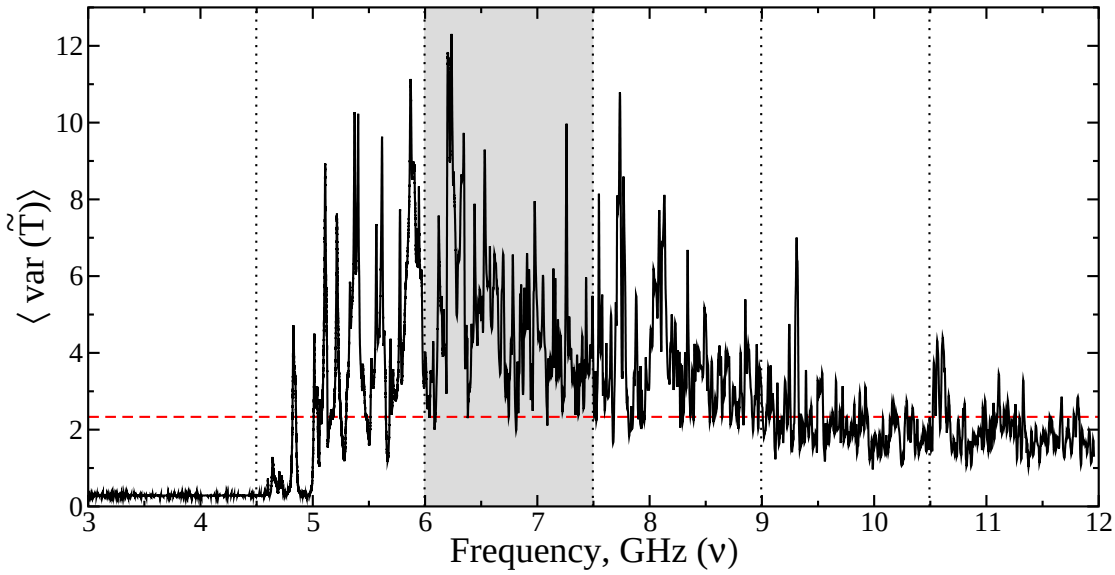

Figure (6.4): Average variance of the normalized transmission, $\sigma^2_{\tilde{T}}$, as a function of microwave frequency. The red dashed line denotes the theoretical threshold of 7/3. Frequencies with an average variance above this threshold are considered localized, while those below are considered diffusive. The vertical dotted lines correspond to frequencies at which a new mode is made available in the system, the smaller numbers in each mode window corresponds to the number of available modes. A localized frequency window is then observed for frequencies in $6.0 - 7.5$ GHz (highlighted in grey), and a diffusive window is observed for frequencies in $10.5 - 12.0$ GHz.

probe the total transmission but just one component of the scattering matrix,

we expect localization whenever $\sigma^2_{\tilde{T}}$ exceeds the critical value of 7/3. We find in Fig.(6.4) that this condition is satisfied approximately in the frequency window 5.59 GHz. Above 9 GHz the waveguide modes are diffusive, while below 5.5 GHz the values of the variances are error prone, as S_{21} is below the precision of the VNA ($|S_{21}| < 10^{-6}$). In the delocalized regime random matrix theory predictions are applicable [94], yielding a value of

$$\sigma^2_{\tilde{\mathrm{T}}} \approx \frac{(2N+1)^2}{N(2N+3)} - 1 \tag{6.1}$$

where N is the number of open channels. In the limit $N \gg 1$, the variance approaches the value $\sigma^2_{\tilde{\mathrm{T}}} \sim 1$, in agreement with our experimental data for the high frequency regime. We shall henceforth then limit our calculations to two windows, a 'localized frequency window' of 6.0-7.5 GHz, which is grey highlighted in Fig.(6.4), and an 'diffusive frequency window' of 10.5-12.0 GHz.

6.2.2 Normalized Transmission Distributions

One of the results from the transmission fluctuations is that the normalized transmission should follow Rayleigh-like distributions in the diffusive frequency window, and then broaden out to log-normal distribution behavior in the localized frequency window [95–97]. The log-normal distribution is defined as

$$P(\tilde{\mathrm{T}}) = \frac{1}{\tilde{\mathrm{T}}\sigma_{\tilde{\mathrm{T}}}\sqrt{2\pi}} \exp\left[-\frac{(\ln(\tilde{\mathrm{T}}) - \left\langle \ln(\tilde{\mathrm{T}}) \right\rangle)^2}{2\sigma^2_{\tilde{\mathrm{T}}}}\right] \tag{6.2}$$

As a secondary check that our wavefunctions are indeed localized, we look at the normalized transmission distributions. The distribution is presented (black line) in Fig.(6.5), along with a best fit of the peak region to Eq.(6.2) presented in red. An agreement is seen, and therefore we are confident the wavefunctions in the frequency regime $6.0 - 7.5$ GHz are indeed localized.

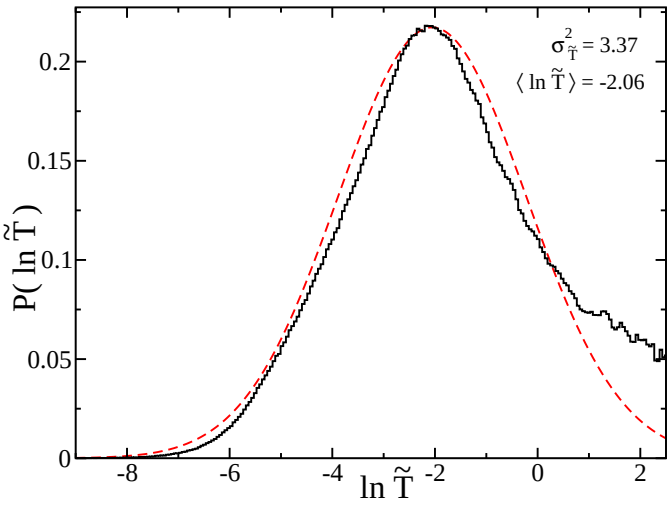

Figure (6.5): Distribution of the normalized transmissions. The black line is the actual transmission distribution from the experiment, while the red line is a best fit to the log-normal distribution of Eq.(6.2). The fit parameter $\sigma^2_{\tilde{T}}$ is calculated as 3.37, which is above the threshold value of 7/3.

6.3 Scattering Fidelity: *Intus Mundus Veris*

6.3.1 The Scattering Matrix

We now have a thorough theoretical understanding of the fidelity behavior in the localized limit for both perturbative regimes. Ultimately, science also dictates all theoretical knowledge must be empirically tested. In the past, much research was done on classical microwave cavities, whose application to wave chaos was

pioneered by Hans-Jürgen Stöckmann & Ulrich Kuhl [15, 98, 99]. The cavities are typically flat, with parallel sides, but with chaotic boundaries (examples include Sinai billard shapes and more recently, mushroom shapes). For microwave frequencies of $\nu < \nu_{cutoff} = \frac{c}{2h}$ where h is the height of the cavity, the cavity appears quasi-one-dimensional - as a reminder, quasi-1D means that the width of the cavity is smaller that its length. For the frequencies below the cutoff, the Helmholtz equation dictating the classical electromagnetic waves is equivalent to a quantum mechanical Schrödinger equation

$$\bigtriangledown^2\psi(x,y) + E(\nu)\psi(x,y) = 0; \quad E(\nu) = \left(\frac{2\pi\nu}{c}\right)^2 \tag{6.3}$$

where Dirchlet boundary conditions are applied at the walls of the cavity.

However, the theoretical quantum definition of fidelity requires the unitary evolution operators, $\hat{U}_{0,1}(t)$. Is there an analog for evolution in the classical Helmholtz wave picture? The answer comes from nuclear physics, in which an incident wave flux, Φ_i, is scattered into an outgoing wave flux, Φ_f. The classical *cross-section* is defined as

$$\frac{d\sigma}{d\Omega} = \frac{\frac{\Phi_f}{\Phi_i}dS}{d\Omega} \tag{6.4}$$

in which $dS, d\Omega$ are infintestimal units of surface and angle respectively. A surface integration over the flux ratio then gives the *integrated cross-section*, σ. The integrated cross-section can be related to the forward scattering wave amplitude

by the *optical theorem* which reads

$$\sigma(E) = |1 - S(E)|^2 \tag{6.5}$$

in which the measure $S(E)$ is the forward scattering wave amplitude. If multiple incoming and outgoing locations (*scattering channels*) are considered, the cross-section and scattering wave amplitude becomes a matrix $\sigma_{ab}(E), S_{ab}(E)$ whose row/column indices correspond to the incoming/outgoing channels, respectively. We can then write

$$|\psi_{out}\rangle = \hat{S}(E)\,|\psi_{in}\rangle \tag{6.6}$$

The matrix $\hat{S}(E)$, called *the scattering matrix* (or S-matrix), can be seen as a form of evolution, in that it takes an steady-state incoming wave and propagates it to a steady-state outgoing wave.

6.3.2 Scattering Fidelity

What is the role then of the perturbation in the S-matrix? Consider a scattering system that can be perturbed in a controlled fashion - the perturbation will give a change to the S-matrix. We will denote an unperturbed S-matrix element as $S^0_{ab}(E)$, and a perturbed element as $S^\lambda_{ab}(E)$. We are ultimately interested in the correlations of the S-matrix, defined as

$$C[S^{0*}_{ab}, S^\lambda_{cd}](E) = \left\langle S^{0*}_{ab}(E), S^\lambda_{cd}(E + dE)\right\rangle - \left\langle S^{0*}_{ab}(E)\right\rangle \left\langle S^\lambda_{cd}(E + dE)\right\rangle \tag{6.7}$$

where the brackets denote an average over a small energy window and/or an average over ensembles. The S-matrix solves a steady-state solution for a given E. However, fidelity is correlations in time, NOT in energy. We can simply take a fourier transform to change the S-matrix correlations into a time correlation

$$C[S^{0*}_{ab}, S^{\lambda}_{cd}](t) = \int_{\Re} dE \exp(2\pi i E t) C[S^{0*}_{ab}, S^{\lambda}_{cd}](E) \tag{6.8}$$

From the convolution theorem then, this is proportional to the individual S-matrix transforms

$$S^{0,\lambda}_{ab}(t) = \int_{\Re} \exp(2\pi i E t) S^{0,\lambda}_{ab}(E) \tag{6.9}$$

which can then be viewed as a scattering evolution operator. The time cross-correlation can be written as

$$C[S^{0*}_{ab}, S^{\lambda}_{cd}](t) \approx \left\langle S^{0*}_{ab}(t) S^{\lambda}_{cd}(t) \right\rangle \tag{6.10}$$

In the absence of a perturbation $\lambda = 0$, we want to have a constant cross-correlation. However, the above cross-correlation yields an autocorrelation, in the absence of a perturbation. Therefore, it is often normalized by the two auto-correlations. This normalized cross-correlation is defined as the *scattering fidelity*

$$f_{ab}(t) = \frac{\left\langle S^{0*}_{ab}(t) S^{\lambda}_{cd}](t) \right\rangle}{\sqrt{\left\langle \left| S^{0}_{ab}(t) \right|^2 \right\rangle \cdot \left\langle \left| S^{\lambda}_{ab}(t) \right|^2 \right\rangle}} \tag{6.11}$$

A nice comparison then is seen between the scattering fidelity and the quantum fidelity, if one makes the comparison $\hat{S}^{0,\lambda}(t) \Leftrightarrow \hat{U}_{0,1}(t)$, but what happens though if there is a large number of scattering channels?

6.3.3 The Role of Absorption

In the past experimental motivations for localization, Figs.(5.2-5.4), one of the main issues that always arises with experimental wave systems is the idea of *absorption*, in which the 'norm' of the measured wave is not conserved. In order to assure norm conservation, perhaps the unaccounted-for norm leaks into a large number of unknown scattering channels (absorbing channels). We say the system is 'open' and then look for resonances with the case of a closed system - i.e. no absorbing channels. The S-matrix for open systems has a *Weidenmüller form* [100]

$$\hat{S}(E) \approx 1 - 2\pi i \hat{W}^{\dagger} \frac{1}{E - \hat{H}_{eff}} \hat{W}; \quad \hat{H}_{eff} = \hat{H}_{int} - \frac{i}{2} \hat{W} \hat{W}^{\dagger} \tag{6.12}$$

in which $\hat{H}_{int}$ is the internal Hamiltonian that describes the closed scattering system and W is a matrix that couples N incoming/outgoing wavefunctions in from / out to M scattering channels. The perturbation then is apparent in this form in the internal Hamiltonian - for unperturbed systems $\hat{H}_{int} = \hat{H}_0$, and for perturbed systems $\hat{H}_{int} = \hat{H}_0 + \lambda \hat{V}$. The utility of Eq.(6.12) is it takes an $N \times N$ internal system and couples it to M channels.

Typically in microwave experiments [99], the known scattering channels are *an-*

tennae that feed microwave signals into the system from an external source. If the diameter of the antennae is much smaller than the wavelength of the incoming and outgoing waves, then each antenna can then be represented as a scattering channel, and then the components of the coupling matrix $\hat{W}$ are just proportional to the wavefunction at the antenna position

$$W_{jk} \propto \psi_j(\mathbf{r}_a) \tag{6.13}$$

The average of the reflections (diagonal terms in $\hat{S}(E)$) can then be written in terms of the coupling matrix

$$\langle S_{aa}(E)\rangle = \frac{1-\kappa_a}{1+\kappa_a}; \quad \kappa_a = \frac{\pi}{2\Delta}\left|W_{ja}^2\right| \tag{6.14}$$

and the transmission coefficients ($T_a = \sum_{b\neq a}|S_{ab}|^2$) can also be written in terms of the reaction κ_a

$$T_a = \frac{4\kappa_a}{(1+\kappa_a)^2} \tag{6.15}$$

We can now apply the Breit-Wigner approximation, which states that if the coupling strengths are low enough, the operator $\hat{W}\hat{W}^\dagger$ can be placed into a scalar form, Γ, which measures the width of the open system's resonances. This allows us to write the average resonant width in terms of the coupling elements

$$\langle\Gamma\rangle \approx \sum_{k=1}^{M}\left|W_{jk}^2\right| = \frac{2\Delta}{\pi}\sum_{a=1}^{M}\kappa_a \tag{6.16}$$

The resonant widths are therefore obtained from the reflections. In the limit of many channels all of equivalent coupling strength, Ericson showed that the cross-sectional correlations decay in an exponential fashion, with a rate given by the transmissions

$$\Gamma_C = \frac{\Delta}{2\pi} \sum_{k=1}^{M} T_k \tag{6.17}$$

Ideally, $\langle \Gamma \rangle = \Gamma_C$. This happens in the limit where $\sum_{k=1}^{M} T_k \ll 1$. For a large number of absorbing channels (say Q) that is much larger than the number of antennae (say A), we only need to account then for the absorbing channels in the Ericson correlation decay, so that

$$T_W = \sum_{k=A+1}^{Q} T_k \tag{6.18}$$

In the limit that $Q \to \infty$ and $\max(T_{k>A}) \to 0$, we can then simply map from correlations in an open absorbing scattering system to those in a closed system by the relation

$$\left\langle S_{ab}^{\lambda,0}(t) S_{nm}^{\lambda,0}(t) \right\rangle \to \exp(-T_W t) \left\langle S_{\alpha\beta}^{\lambda,0}(t) S_{\nu,\mu}^{\lambda,0}(t) \right\rangle \tag{6.19}$$

in which the indices range as $\{a, b, n, m\} \in [1, M]$ and $\{\alpha, \beta, \nu, \mu\} \in [1, A]$. Therefore, the effect of absorption is to introduce a decay in the correlations with a constant rate. Since the scattering fidelity definition involves a cross-correlation divided by root-squared autocorrelations, the constant decay rate on both correlations will simply divide out - making scattering fidelity a very powerful tool in

the study of open systems. In this Breit-Wigner approximation, the scattering fidelity of Eq.(6.11) is then fully equivalent with the quantum mechanical definition of fidelity seen in previous chapters.

6.4 Experimental Scattering Fidelity - Diffusive Frequency Window

In [61, 101], the scattering fidelity was investigated for chaotic cavities, and compared to the known GOE LRT result of Eq.(5.12). A representative figure of the findings is presented in Fig.(6.6). The chaotic cavity is a quasi-1D microwave cavity with large brass inserts inserted to make the boundary non-analytic, shown in the inset of Fig.(6.6). "X" in the figure denotes where the antennae were located. The perturbation used is also similar to ours, in that one of the walls is shifted. Different boundary realizations are obtained by moving the lower semicircular insert. The scattering matrix is measured with an experimental VNA setup identical to our own, and the correlations of the fidelity transformed scattering matrix elements are numerically found. The scattering fidelity amplitude, Eq.(6.11), for a given boundary realization is then calculated and averaged over the different boundary realizations. The main part of Fig.(6.6) shows the resulting experimental scattering fidelity for the reflection from the right antenna. A good agreement is seen with the theoretical LRT fidelity of Eq.(5.12), the orange line.

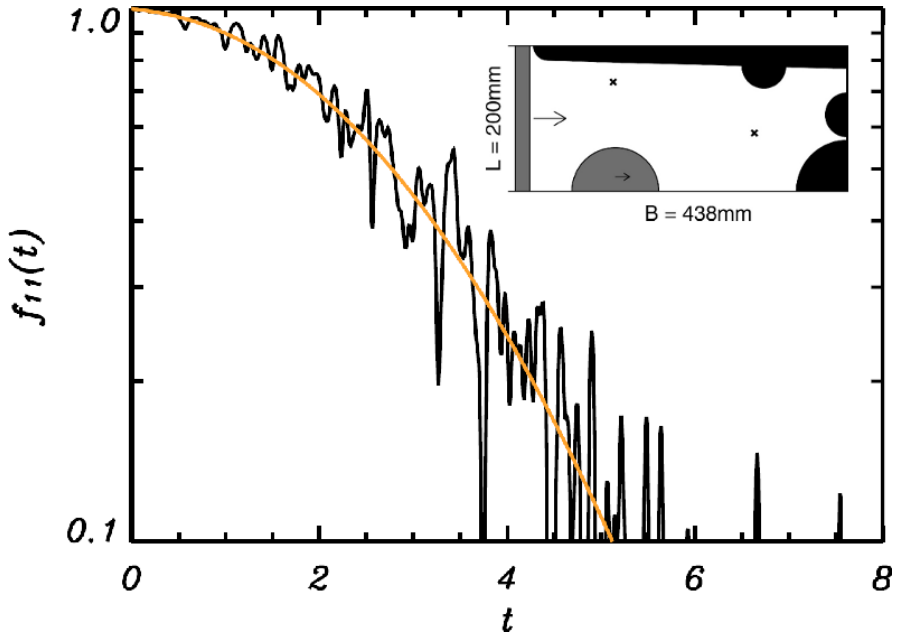

Figure (6.6): Inset: A chaotic microwave cavity formed by non-analytic brass inserts in the cavity. X denotes antennae positions. The perturbation to the system is small shifts in the left wall. Different boundary realizations are obtained by changing the position of the lower insert. Main Figure: The experimental scattering fidelity (black line) from the reflections of the right antenna, compared to the LRT expectation of Eq.(5.12). A nice agreement is seen. Figure taken from [101].

The perturbation is geometric in nature (changing size of cavity), so we can use geometric considerations to build the perturbation. Geometrically, the matrix element of the perturbation is [26, 102]

$$(H_1)_{nm} = w \int_0^L dy \ \bigtriangledown_\perp \psi_n(y) \cdot \bigtriangledown_\perp \psi_m(y) \tag{6.20}$$

Since $\lambda^2 = \langle (H_1)^2_{nm} \rangle$, we can now use a Berry conjecture of random plane wave superposition. Close to a straight boundary wall with Dirchlet conditions, the

correlations that result in taking an average over the above matrix are Bessel in nature. Integration of the Bessel correlations yield

$$\lambda^2 = \left\langle (H_1)^2_{nm} \right\rangle = \frac{4k^2w^2L}{A^2}\frac{8}{3\pi} \tag{6.21}$$

The approximation of the correlations going to Bessel functions is ultimately semi-classical in nature, therefore the approximation for λ above works very well for high wavenumbers. For $\Delta \sim 1$, the area can be set to $A = 4\pi$ to yield

$$\lambda^2 = \frac{2L}{3\pi^3}k^3w^2 = \frac{16L}{3c^3}\nu^3w^2 \tag{6.22}$$

It is important to note then that $\lambda \sim w$ is the expectation we are looking for.

What do we mean 'the expectation we are looking for'? For our scattering system, we repeat the same calculations as was done for chaotic cavities. In the diffusive frequency window, the expectation is that the scattering fidelity should behave similarly to that seen in chaotic systems. Performing the calculation, we look at the fidelity resulting from the bulk antenna reflections, $S_{22}(E)$. The main purpose for this rests in the simple fact that antenna #1 is too close to the shifting wall - the perturbation appears locally to this antenna, and therefore the strength is much stronger. This results in fidelity decays that are extremely fast - most of the wallshifts gave immediate decays for $S_{11}(E)$. In Fig.(6.7), we present one such respective scattering fidelity decay, for $S_{22}(E)$. The points represent the actual scattering fidelity, while the straight line is the best fit of the numerical data to

Eq.(5.12), with the variable λ treated as a free fitting parameter. All fitting was done in the standard perturbative regime for $t < t_H$.

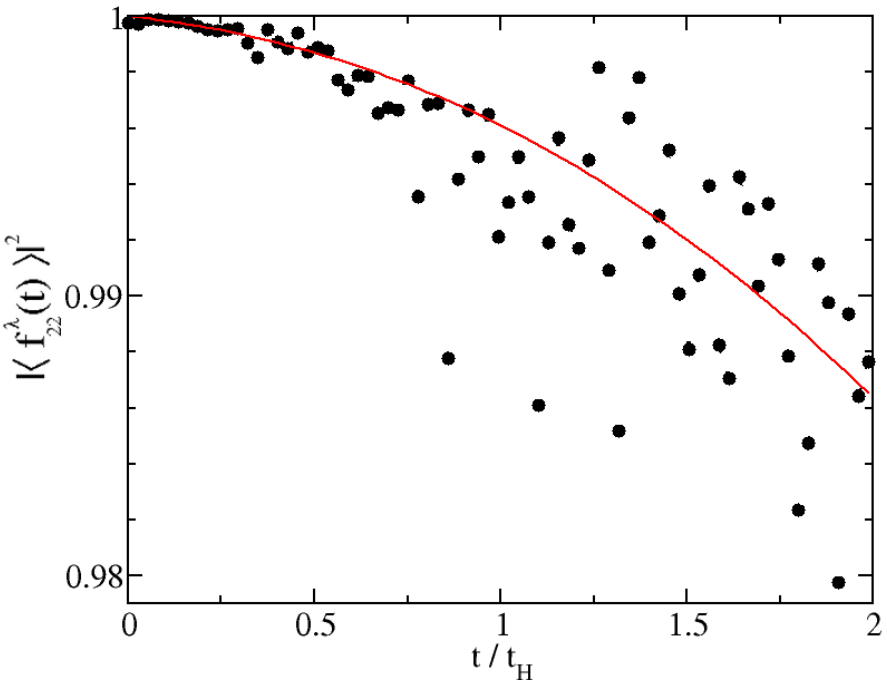

Figure (6.7): A typical fidelity decay in the diffusive frequency window of $10.5 - 12$ GHz. The dimensionless wallshift is $w/\delta w = 2$. The solid line is a best fit of the data to Eq.(5.12). The resulting fit parameter λ is compared against $w/\delta w$ in Fig.(6.8) in order to verify the scaling of Eq.(6.22).

We then perform this fitting procedure for a variety of wallshifts w. We want to compare the free fitting parameter λ to the wallshift w. This is seen in Fig.(6.8), in which the scaling relation of $\lambda \sim w^{\eta}$ is fit. A power law of $\eta \sim 1.0 \pm 0.05$ is found, confirming 'the expectation we are looking for'. It is important to note that the scaling of the free-fit parameters with the wallshift is what verifies whether a given model for the fidelity decay is correct.

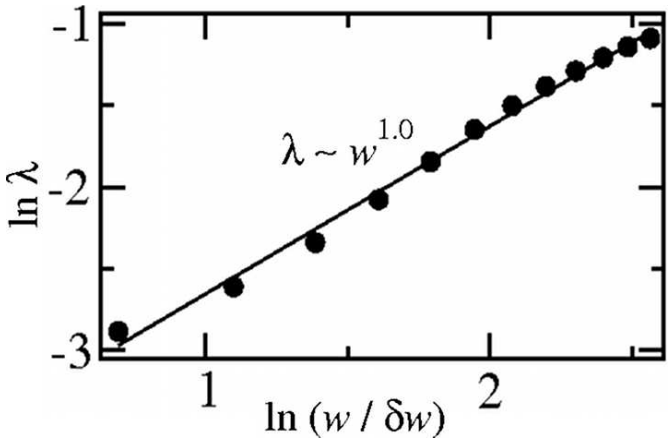

Figure (6.8): Within the diffusive frequency window, the scaling of the free-fit parameter λ of Eq.(5.12) with the dimensionless wallshift $w/\delta w$. The dots represent the extracted data. The solid line is the best fit to a power law relation $\lambda \sim w^{\eta}$. A power of $\eta = 1.0 \pm 0.05$ is found, confirming the validity of Eq.(5.12).

6.5 Experimental Scattering Fidelity - Localized Frequency Window

6.5.1 Standard Perturbative Regime

Within the standard perturbative regime, the theoretical expectation for waves in the localized frequency window ($6.0 - 7.5$ GHz) is the novel fidelity decay found in Eq.(5.25). Within this equation, the free-fitting parameter of $\alpha \propto \sqrt{P_2} w$ gives us the expectation that $\alpha \sim w$. We have fit the experimental data of scattering fidelity in this frequency window to both predictions of the extended and the localized fidelity decay law, treating λ as a free-fit parameter. A representative

experimental fidelity curve and the fits are shown in Fig.(6.9), in which the points represent experimental data, the solid line is the localized best fit of Eq.(5.25), and the dashed line is the diffusive best fit of Eq.(5.12). The wallshift of the perturbation in Fig.(6.9) yields from Eq.(6.22) of $\lambda \sim 0.115$.

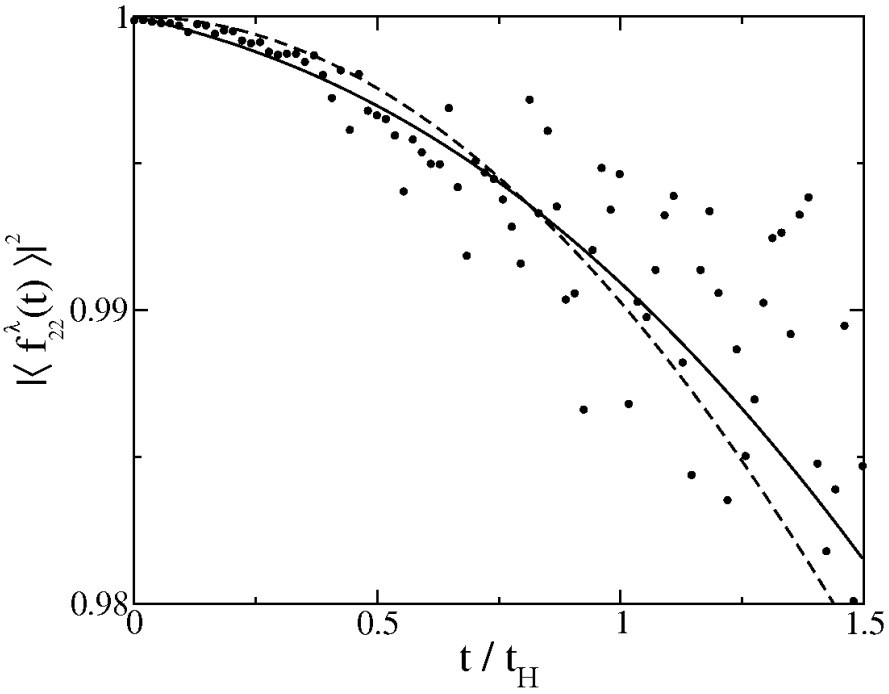

Figure (6.9): A typical fidelity decay for the standard perturbative regime in a localized frequency window. The points are the experimental data. The solid line represents a best fit to the localized fidelity of Eq.(5.25), while the dashed line represents a best fit to the diffusive fidelity of Eq.(5.12). A better fit to the localized fidelity is observed.

The result is clear - the localized fidelity of Eq.(5.25) fits much better than the diffusive fidelity of Eq.(5.12). This can further be quantified in the scaling of the free-fit parameters. Whichever free-fit parameter (α for the localized model and

λ for the diffusive model) best scales as $\sim w$ ultimately tells us which model is the best. The scaling analysis is performed in Fig.(6.10), in which the free-fit parameters are plotted against the dimensionless wallshift, $w/\delta w$, and then fit to a power law of $\alpha, \lambda \sim w^{\eta}$. Within the figure the squares correspond to α and the circles correspond to λ. Using the localized fidelity of Eq.(5.25), a scaling of $\eta = 0.92 \pm 0.05$ was obtained. For the case of the diffusive fidelity of Eq.(5.12), a scaling of $\eta = 1.9 \pm 0.05$ was obtained. Since the localized fidelity gave a better scaling, it is the proper model to use for fidelity in the localized frequency window.

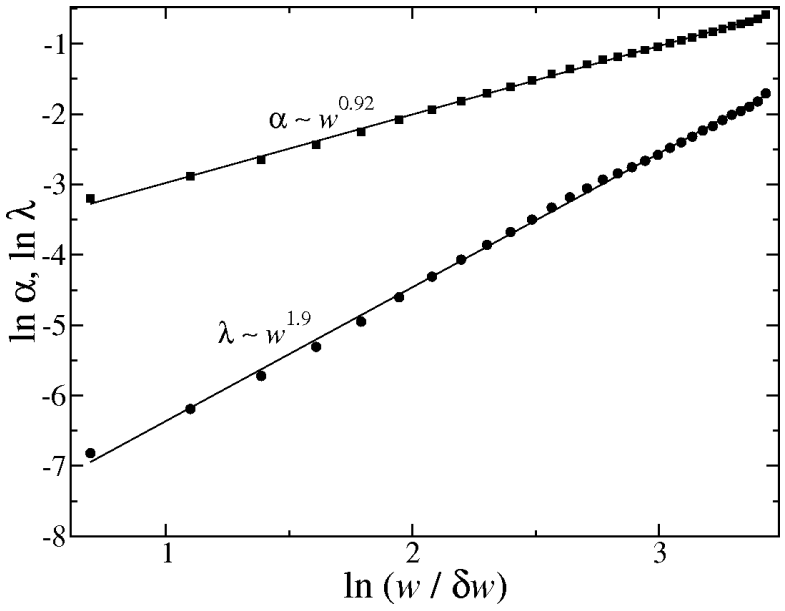

Figure (6.10): Scaling analysis of the fitting parameters within the localized frequency window. The squares denote the α parameter from Eq.(5.25) while the circles denote the λ parameter from Eq.(5.12). The straight lines indicate a power law fit to $\alpha, \lambda \sim w^{\eta}$. The α then scale properly as $\eta = 0.92 \pm 0.05$, suggesting Eq.(5.25) as the correct fit. The failure of the λ parameter to scale as $\sim w$ (scales as $\eta = 1.9 \pm 0.05$) additionally shows Eq.(5.25) as the better description of fidelity decay in localized scattering systems.

To close this regime, an emphasis on the relation $\alpha \propto w\sqrt{P_2}$ can not be overstated; this relation dictates that the slope of the straight line in Fig.(6.10) may therefore be used to extract out the inverse participation number, in the event the state is localized.

6.5.2 Wigner (FGR) Regime

Within the Wigner (FGR) Regime, the fidelity within the localized window has a theoretical expectation of Eq.(5.28). The 'crossover' between the standard perturbative and Wigner regimes was observed where the fidelity decay of Eq.(5.25) began to fail to capture the decay behavior, typically occurring at wallshifts with the chaotic perturbation strength from Eq.(6.22) of $\lambda \sim 1$. The region $t_H/2 < t < 4t_H$ was then fit to the exponential decay of Eq.(5.28), with the decay rate of γ[†] as the fitting parameter. A typical fidelity decay in this regime is shown in Fig.(6.11), in which the points are the experimental data, the blue curve is the best fit to Eq.(5.12), which now clearly fails to capture the fidelity decay. The red line is the exponential fit of Eq.(5.28). The wallshift of this perturbation yields from Eq.(6.22) $\lambda \sim 2.218$.

[†]Note that in Eq.(5.28) the decay rate is Γ. Here, we use the lower case γ.

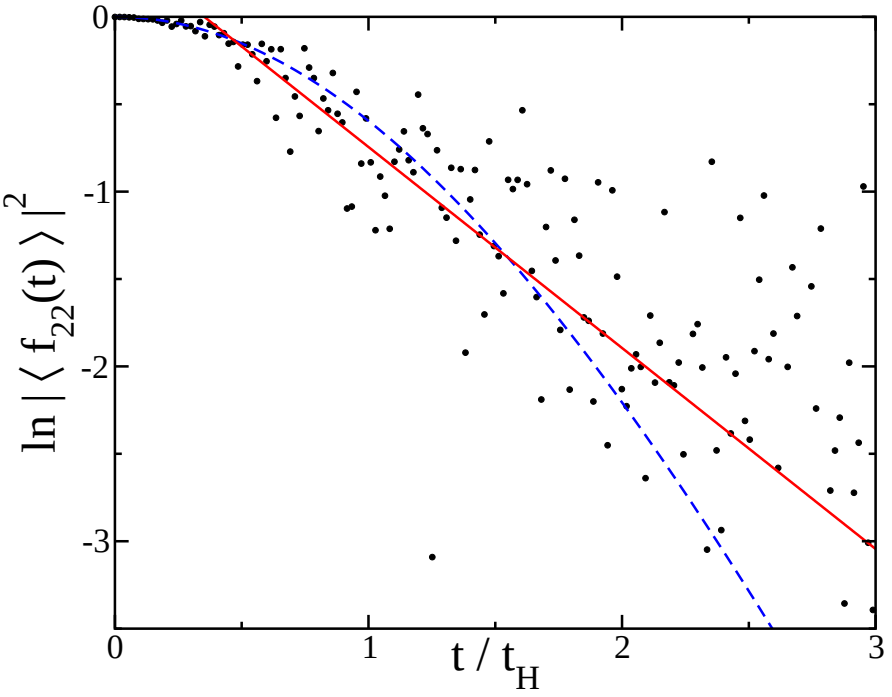

Figure (6.11): A typical fidelity decay for the Wigner (FGR) regime in a localized frequency window. The points are the experimental data. The dashed blue line represents a best fit to the diffusive fidelity of Eq.(5.12), which now clearly fails to capture the fidelity decay. The red line represents a best fit to the exponential decay of Eq.(5.28), which captures the decay behavior nicely.

The fitting is performed for several different wallshifts, and the free-fit parameter γ is then plotted against the dimensionless wallshift $(w/\delta w)$ in Fig.(6.12). A power law scaling of $\gamma \sim w^{\eta}$ is then extracted, and a power of $\eta = 2.3 \pm 0.05$ is found. As opposed to α, λ in the standard perturbative regime, the theoretical scaling expectation in the Wigner (FGR) regime was found to be $\gamma \sim w^2$ (see Appendix B.4). Therefore, we also capture the correct decay behavior in the localized frequency window for the Wigner (FGR) regime.

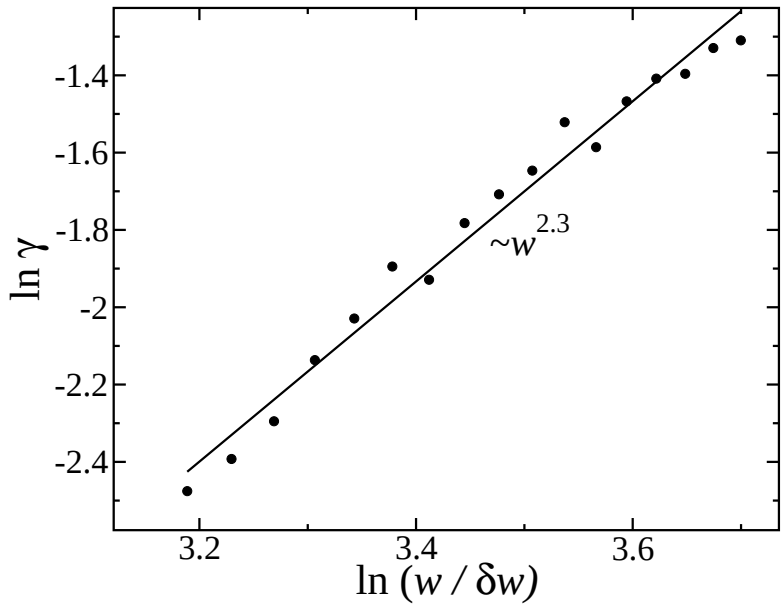

Figure (6.12): Scaling analysis of the exponential fitting parameter γ from Eq.(5.28), for localized fidelity in the Wigner (FGR) regime. The circles denote the γ parameter. The straight line indicates a power law fit to $\gamma \sim\sim w^{\eta}$, with a power of $\eta = 2.3 \pm 0.05$. The experimental data then captures the correct scaling of $\sim w^2$.

6.6 Conclusion

In summary, a microwave cavity scattering system was proposed as an experimental approach, and the idea of an experimental correlation from measured scattering matrices was presented in the scattering fidelity. The frequencies that corresponded to localized and diffusive states were characterized by the transmission statistics. The experimental scattering fidelity was then found for frequencies in both the localized and diffusive frequency windows. Scattering fidelity within

the diffusive frequency window was shown to reproduce the standard LRT result of Eq.(5.12). Scattering fidelity within the localized frequency window was shown to fit to both Eqs.(5.25, 5.12), however, scaling analysis suggests both the failure of Eq.(5.12) and the validity of Eq.(5.25). A similar scaling analysis was also used to experimentally verify our localized theoretical model within the Wigner (FGR) regime. We are confident that fidelity in the standard perturbative regime can then be used as a probe to determine localization and its extent.

Chapter 7

Fidelity at Criticality: Wigner Lorentzian Random Model

Beyond a critical point within a finite space, freedom diminishes as numbers increase...

-Frank Herbert, Dune

In the past chapter, we addressed fidelity in the context of probing only localized or extended states. But what about the 'in-between' area where states are neither extended or localized, but exhibit a multifractal character? Such a system is said to be at a critical Anderson *metal-insulator transition* (MIT). The goal of this chapter is to use fidelity to probe transport in these systems that are critical. Examples of physical systems which display critical Anderson MIT behavior include three-dimensional disordered lattices [69], two-dimensional low temperature electron gases in strong electromagnetic fields (quantum Hall effect) [103] one-dimensional quasi-periodic lattice systems (Harper and Fibonacci

models) [104, 105], and kicked rotor systems with a logarithmic potential singularity [106, 107].

Our main finding is that the fidelity of a critical system, within the non-perturbative regime, exhibits a novel power-law decay of

$$F(t) \sim t^{-D_2} \tag{7.1}$$

where D_2 is the effective fractal dimension that the critical wavefunctions span. We will arrive at this conclusion in the following manner: in the first section, we discuss in detail the Anderson MIT through two important physical examples and introduce the geometrical measures of D_2. We shall then go on and discuss an RMT model (the power banded random matrix) applicable to critical systems. From this RMT model, we calculate both the fidelity and its linear response approximation within the three regimes. Within the non-perturbative regime, we observe the above power-law decay, in which we conclude the chapter with a heuristic argument to explain such behavior.

7.1 Anderson Metal-Insulator Transition

In many different physical systems, the idea of a phase transition is present. A 'phase', in the physical sense, is a thermodynamic state in which properties (like density, particle velocities, etc.) are uniform throughout the system. Usually introduced via 'states of matter', in which there are solid/liquid/gas/plasma phases,

phase transitions are ubiquitous. Examples include evaporation (liquid → gas), condensation (gas→liquid), melt (solid→liquid), freeze (liquid→solid), ionization (gas→plasma), recombination (plasma→gas),sublimation (solid→gas), and deposition (gas→solid). The transition is characterized by a change in the thermodynamic conjugate variables (entropy, temperature, pressure, volume, etc.), and falls into one of three categorical behaviors (first-order, second-order, and infinite-order), based on divergences in the derivatives of the thermodynamic free energy with respect to a conjugate variable.

Transitions are not exclusive only to 'state of matter' phases. A popular pedagogical and well-understood example is the phase change from ferromagnetism to paramagnetism, modeled by the Ising spin model. Technologically, phase transitions between crystalline-amorphous phases are responsible for rewritable optical media, such as CD/DVD/BD-RW. In fact, another type of phase transition has already been presented in the introduction of Chapter 4 with condensation of bosons from classical particles to a quantum matter-wave (BEC). Within this chapter, we extend the idea of a phase transition to the transport properties of wave systems. Specifically, in the previous chapter we discussed the transition from localized to diffusive waves as the disorder decreases. Our discussion was confined to quasi-one dimensional disordered media, where this transition is smooth and is parametrized by a single scaling parameter, which is the ratio of the localization length to the system size. A much more interesting scenario take place in higher dimensional cases ($d > 2$) where the transition from a metallic (diffusive) to an insulating (localized) phase is not anymore smooth, but rather

is characterized by a divergence of the correlation (localization) length at a critical point. This second order phase transition is termed *Anderson metal-insulator transtion (MIT)* and is driven either by a change of the disorder strength, W or by the energy of the system.

At the critical point of the Anderson MIT, the eigenstates strongly fluctuate at all scales, displaying a self-similar structure, which is illustrated in Fig. (7.1).

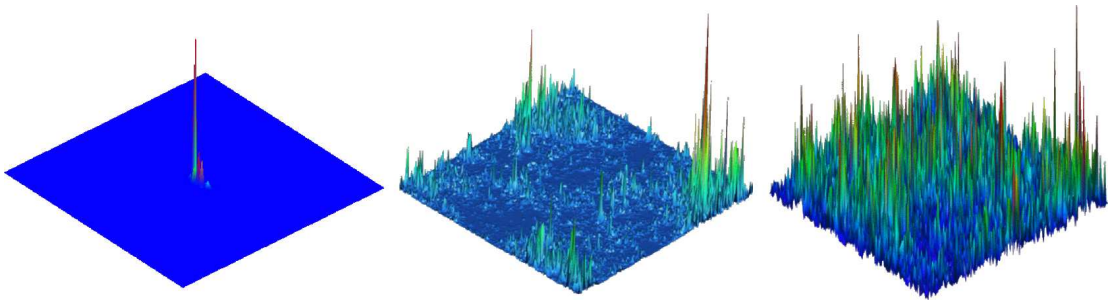

Figure (7.1): Eigenstates (in 2D) for an Anderson metal-insulator transition. The left image is the eigenstate for a strongly disordered lattice, and is localized. The right figure is the eigenstate in the metallic regime, and is extended throughout the space. The middle image is the eigenstate at the critical point, and it exhibits a self-similar structure, in that the fluctuations seen are present at any scale of this image. Image taken from [108].

The order parameters appear as *critical exponents* in the various system observables, like the correlation lengthscale in the eigenstates, $\xi(E)$ (*i.e.* the localization lengths) and the DC conductivity, $\sigma(E)$, both of which behave as

$$\xi(E) \propto (E_c - E)^{-\nu}, \tag{7.2}$$

$$\sigma(E) \propto (E - E_c)^{s} \tag{7.3}$$

where the two exponents are related to each other via the scaling $s = \nu(d-2)$ [73]. At the critical point $E = E_c$, the localization length diverges, yielding an infinite lengthscale.

7.1.1 Geometry of the MIT

Additionally at the critical point, 'single-fractal' dimensional analysis methods, such as the box-counting method (see Appendix B.5) fail because the fluctuations are so strong and exist at any scale. Specifically, the failure is that the Minkowski-Bouligand dimension (the 'single-fractal' dimension) equals the system dimension ($D = d$), therefore the parameter D is not enough to characterize the fluctuations. Rather, higher moments of the eigenstates

$$P_q = \int_V d\mathbf{r} \, |\psi(\mathbf{r})|^{2q} \tag{7.4}$$

are needed to describe the fluctuations. At criticality, the average moments behave as $\langle P_q \rangle = L^d \langle |\psi(\mathbf{r})|^{2q} \rangle \sim L^{-\tau_q}$. The set of all τ_q's can then be related to a (possibly infinite) set of non-zero fractal dimensions D_q^ψ where $q = 0, 1, 2, \ldots$,

$$\tau_q = D_q^\psi (q-1) \tag{7.5}$$

of which only one is the Minkowski-Bouligand dimension ($q = 0$). In particular, if one considers the second wavefunction moment ($q = 2$),

$$P_2 \sim L^{-D_2^\psi}, \tag{7.6}$$

where D_2^ψ is called the *correlation dimension* and P_2 is more popularly known as the inverse participation number (IPN), seen in the previous chapter. The correlation dimension behaves as $D_2^\psi = d$ for an extended state, and $D_2^\psi = 0$ for a localized state. The IPN can then be seen to be an inverse 'effective volume' of the wavefunction, spanning D_2^ψ. This idea of requiring multiple dimensions D_q^ψ to describe the system is called 'multi-fractality' and is essential to systems at criticality. Typically D_q^ψ is defined by the eigenstates (via the IPN), but it can also be defined by the energy levels. Looking at the variance in the level counting function $N(E)$ in a large window (with respect to Δ, the mean level spacing), it was found that $(\delta N)^2 \propto \chi \langle N \rangle$. The value χ is the *spectral compressibility*, and it yields a dependence $\chi = (d - D_2^\psi)/2d$ [73]. The correlation dimension may also manifest itself in a variety of other physical observables; for example, the conductance distribution [109, 110], wave-packet spreading [111], the spatial dispersion of the diffusion coefficient [112–114] and the scaling of Wigner delay times [115]. The last example in particular is interesting, and further discussion of it is presented in Appendix A..

7.1.2 Physical Systems at MIT

We present the physical case of the quantum Hall effect[†] (QHE) as a motivation. In Fig.(7.2), a low-temperature electron enters a region permeated with strong constant magnetic field, whose strength (B) can be varied. If no magnetic potential is present, the electron moves ballistically through the region. As the magnetic potential increases, a Lorentz force acts on the electron, forcing it into a quantized cyclotronic motion. For a large number of electrons, a current exists in both the straight, ballistic direction (red path) and in the direction of the Lorentz force (green path), assuming an injection velocity of $\mathbf{v} \propto \hat{x}$. The resistivity (inverse conductivity) is measured along both the transverse/longitudinal directions, yielding ρ_{xy} and ρ_{xx}. As the magnetic field changes a discrete behavior is observed for both resistivities - this is presented in Fig.(7.3).

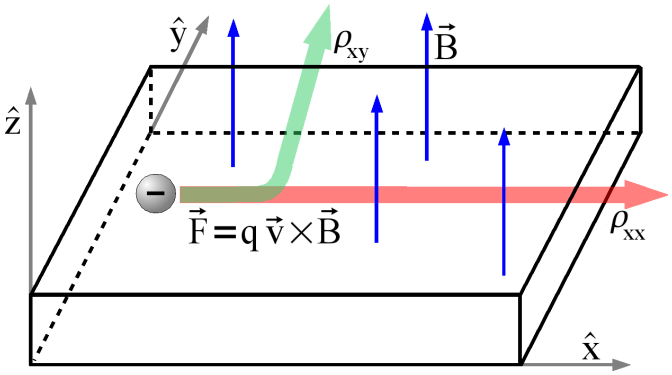

Figure (7.2): Due to the Lorentz force, a low-temperature two-dimensional electron gas (2DEG) undergoes Landau quantization (cyclotron orbits) in the presence of a constant magnetic field. The resistance in both the transverse (red) and longitudinal (green) directions can be measured.

[†]The importance of the Quantum Hall Effect can not be understated, both as an example of a critical system, and in setting a new resistance measure standard, in the form of the flux quantum, $\Phi_0 = \hbar/(2e)$. This importance was recognized by two Nobel prizes [116]: one in 1985 to van Klitzing for the discovery of integer QHE, and one in 1988 to Tsui & Stormer for the discovery of fractional QHE.

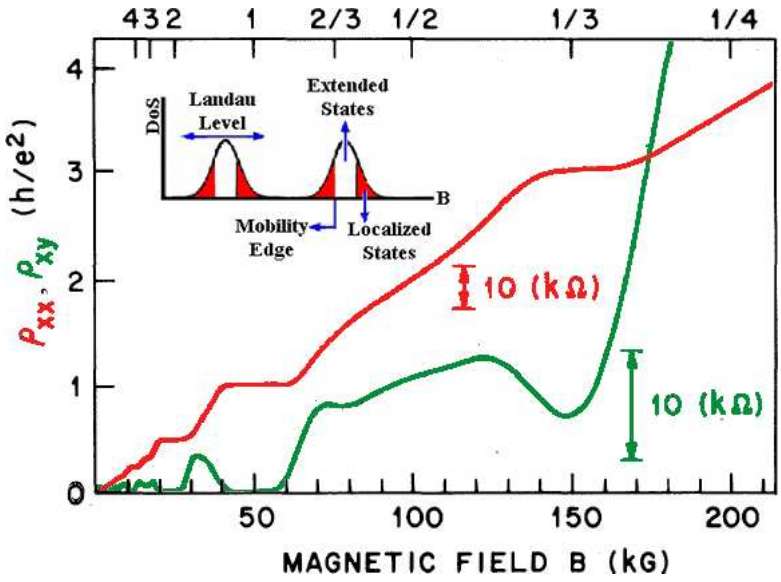

Figure (7.3): Transverse/Longitudinal Resistances measured in the 2DEG. The discreteness in the resistance is directly due to the Landau quantization. The inset shows what happens at higher magnetic field strengths, at which point the resistance quantization becomes fractional, as dictated by the fractional relations shown in the top axis. This is due to the density of states containing critical states at a mobility edge - when the field strength hits a mobility edge, fractional subplateaus are observed in the resistance. The scale for the two different resistances is shown next to their respective data, and are both scale and data are colored respectively to the previous subfigure. Image based on figure from [117].

For weaker fields, the discreteness is integerized (the 'integer' QHE), while at higher field strengths, the discreteness becomes fractional (the 'fractional' QHE). The discreteness is understood through the B-dependent quantized levels (*Landau levels*) that the electron may occupy. The Landau levels are manifested in the density of states (DoS) - varying the magnetic field is akin to sweeping the Fermi energy across the Landau levels in the DoS. When the Fermi energy is pinned between two Landau levels, no further states are available for occupation, halting

any electron transport. This is the case for the integer QHE. At higher field strengths, *mobility edges* develop - in that the tails of the DoS contain localized states, and the core contains extended states. Critical states occur only at the mobility edge, which sweeping across with the Fermi energy gives the fractional subplateaus in the resistivity. The self-similarity in critical behavior becomes evident when one considers the energy spectra as the magnetic field strength varies. At critical values, the spectra itself becomes self-similar - popularized [118] via the *Hofstadter butterfly*, which is shown in Fig.(7.4). It is these critical states that now attracts our interest.

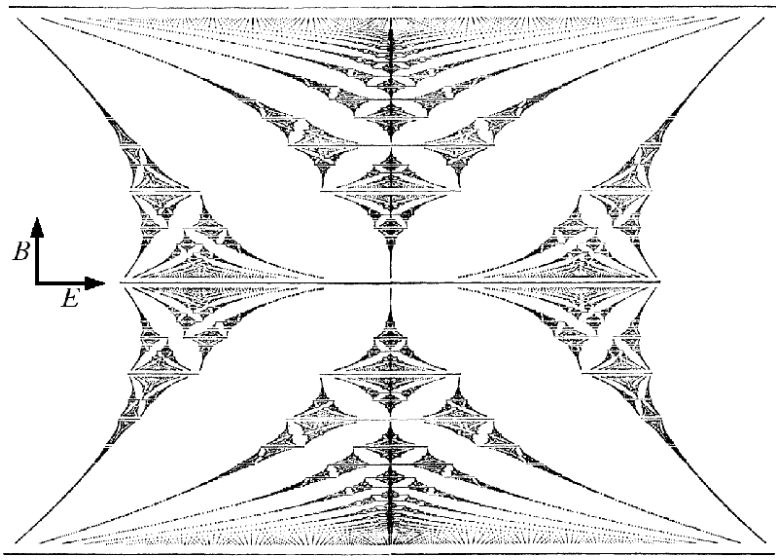

Figure (7.4): The beauty of the Hofstadter butterfly. The horizontal axis contains the energy spectra, while the vertical axis is the field strength. At the fractional subplateau values in the previous figure, the spectra becomes a self-similar (fractal) structure. Image taken from [118].

As an additional example of a physical system exhibiting critical behavior, consider one-dimensional quasi-periodic lattice systems. In particular we focus on the Harper model [104, 119], which is a tight-binding Hamiltonian with the following

discrete onsite potential

$$V_n = 2\cos(2\pi n\alpha) \tag{7.7}$$

where the parameter α plays the role of the order parameter, much as the magnetic field strength does in the QHE - in fact the equivalence is $\alpha = a^2 eB/(2\pi\hbar)$, where a is the lattice spacing. Such a lattice system is critical when the value α takes on irrational fractions, akin to the fractions seen in QHE, Fig.(7.3). The potential in Eq.(7.7) can be experimentally realized in a one-dimensional microwave cavity [105], as shown in Fig.(7.5a)

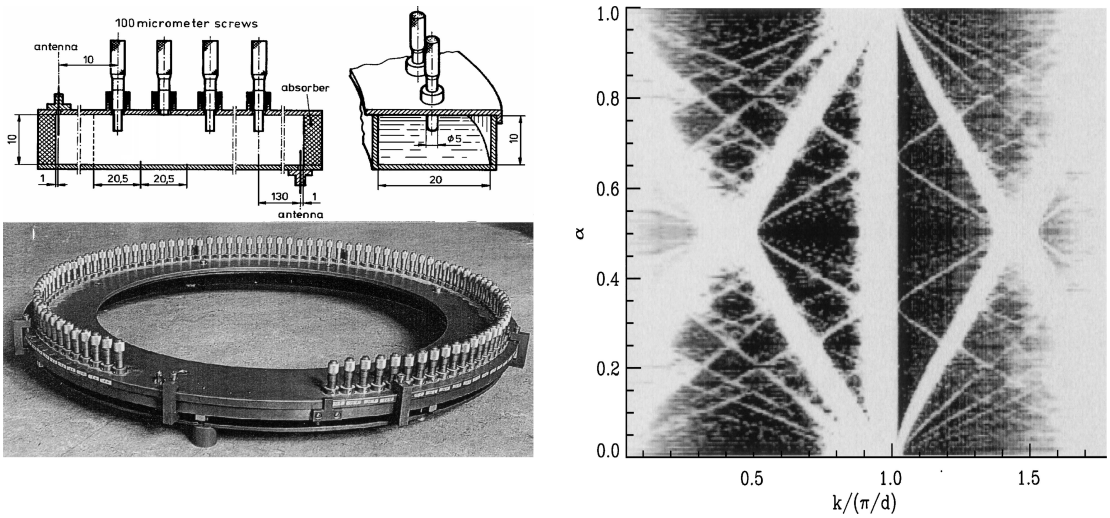

(a) An experimental 1D microwave cavity

(b) Spectra from the microwave experiment, showing a Hofstadter butterfly

Figure (7.5): An experimental 1D microwave cavity is shown in the left, in which the scattering posts are arranged quasiperiodically, according to Eq.(7.8). A single antenna is placed at one end of the cavity, while the other end contains an absorber. The energy spectra are then measured (via a network analyzer) for different values of α, and display a Hofstadter butterfly pattern, shown in the right. Figures taken from [105].

in which the scattering post penetration depth into cavity, l_n, is arranged as

$$l_n = \begin{cases} l_0, & \cos(2\pi n\alpha) > 0 \\ 0, & \cos(2\pi n\alpha) \leq 0 \end{cases} \tag{7.8}$$

where $l_0 = 3\,\text{mm}$. The spectra are then measured and the Hofstadter butterfly is reproduced, as shown in Fig.(7.5b).

7.2 Modeling Critical Systems

Recent advances in random matrix theory allow us to model the statistical properties of critical systems. A new RMT ensemble[†] goes by the name of *power-law banded matrices (PBRM)*, which are similar to traditional GOE in that the matrix elements are given by a Gaussian distribution with a zero mean, but are distinguished from traditional GOE via a variance of

$$\sigma_{nm}^2 = \frac{1}{1 + \left(\frac{|n-m|}{b}\right)^{2\alpha}} \tag{7.9}$$

For $\alpha = 1$ the ensemble shows all the characteristics of a system at a MIT, like wavefunction fractality and anomalous transport [120–122]. The continuous parameter b denotes an effective bandwidth and gives a *line of critical points* in the range $b \in (0, \infty)$. The role of b is really to control how multifractal the eigen-

[†]We will limit our discussion here to the time-reversal case only.

states are. In fact, its bounds give behaviors similar to those seen in non-critical Anderson transitions in high and low dimensional systems: for $b \ll 1$, the multifractality is 'weak', and corresponds to small deviations from two-dimensional Anderson transitions ($2+\epsilon$ models). On the other end, $b \gg 1$, the eigenfunctions fluctuate quite strongly as for Anderson transitions in which $d \gg 1$. Both limits can be placed into a field-theoretical (nonlinear σ) model, and an analytical form for the correlation dimension is found [123]

$$D_2^{\psi} = \begin{cases} \frac{4\Gamma(3/2)}{\sqrt{\pi}\Gamma(1)} b, & b \ll 1 \\ 1 - \frac{2}{2\pi b}, & b \gg 1 \end{cases} \tag{7.10}$$

Besides eigenstate correlations, field-theoretical analytics also give approximations on other observable correlations, in particular correlations in the fluctuating density of states $\rho(E)$. For example, the two-level cluster function introduced in Eq.(2.21) has been shown [124] to have for $b \ll 1$ the form

$$Y_2(s) = \mathrm{erfc}\left(\frac{|s|}{\sqrt{\pi} b} - \delta(s)\right) \tag{7.11}$$

where s is the energy normalized by the mean level spacing, and $\mathrm{erfc}(x) = 2/\sqrt{\pi} \cdot \int_x^{\infty} \exp(-t^2) dt$. The two-level correlations can further be related to the spectral compressibility

$$\chi \simeq \begin{cases} 1 - 4b, & b \ll 1 \\ \frac{1}{2\pi b}, & b \gg 1 \end{cases} \tag{7.12}$$

and also be applied to local density of states (LDoS), in which case correlations scales with the dimension D_q^{μ}. The two-level ($q = 2$) correlation, results in $D_q^{\mu} = D_2^{\psi}/d$, but since the WLRM is one-dimensional, we have $D_2^{\psi} = D_2^{\mu} = D_2$. Regardless of the correlation taken, for any within the WLRM, there is always a dependence on the parameter b. Therefore, we shall focus on the 'simplest' correlation measure, the IPN, and its associated correlation dimension of $D_2(b)$.

7.3 Fidelity at Criticality

In the chapter's remainder, we analyze the fidelity decay for systems at criticality. Our mathematical modeling is based on the PBRM ensemble. Specifically, we define [120, 121, 125, 126] the following model

$$\hat{H} = \hat{H}_0 + x \cdot \hat{B} \tag{7.13}$$

where both $\hat{H}_0$ and $\hat{B}$ are taken from a PBRM ensemble with $\alpha = 1$ and the same b. Hereafter, we will refer to this model as the Wigner Lorentzian Random Matrix (WLRM) model. The forward and backward Hamiltonians used for the calculation of fidelity are

$$\hat{H}_f = \hat{H}(x), \quad \hat{H}_b = \hat{H}(-x) \tag{7.14}$$

We operate in the basis of a diagonalized $\hat{H}_0$. In this basis, the perturbation matrix $\hat{B}$ is x-invariant [126], *i.e.* it preserves the same Lorentzian power-law shape from Eq.(7.9), while its critical properties (like the multifractal dimension D_2^{ψ}) remain unchanged. For the numerical evaluation of the fidelity, we have used two types of initial conditions for $|\psi_0\rangle$: an eigenstate of $\hat{H}_0$ (ES) and a generic random state (RS). In both cases, the results are qualitatively the same. Therefore, we will not distinguish between them. In our numerical experiments we used matrices of size varying from $L = 1000$ to $L = 5000$. We have additionally performed an averaging over different initial states and realizations of the perturbation matrix $\hat{B}$ (typically more than 1000).

An overview of the temporal behavior of the fidelity,$F(t)$, for three representative perturbation strengths is shown in Fig.(7.6). Using the Wigner Lorentzian random matrix (WLRM) ensemble, we find that there also the three regimes: the standard perturbative regime where the decay is Gaussian ($x < x_c$), the Wigner (FGR) regime where the decay is exponential ($x_c < x < x_{prt}$), and the nonperturbative regime ($x > x_{prt}$) where an initial Gaussian decay (Zeno decay) is followed by a **power-law**. The latter decay is novel and reflects the critical nature. of the system. Specifically, we found that

$$F(t) \sim \frac{1}{t^{D_2^{\mu}}} \tag{7.15}$$

where [127] $D_2^{\mu} = D_2^{\psi} = d$ is the correlation dimension of the local density of states (LDOS), while D_2^{ψ} is the correlation dimension of the critical eigenstates,

and d is the actual dimensionality of the system.

7.3.1 Linear Response Theory within the Two Perturbative Regimes

The linear response result of Eq. (3.12) reads for the model of Eq.(7.9) as

$$\langle F(t)\rangle \approx 1-(2x)^2\mathcal{C}(t) \approx \exp\left[-4x^2\mathcal{C}(t)\right] \tag{7.16}$$

The correlator is found from analytical integrations[†] of the correlation terms in a Born series expansion, substituting in the WLRM variance ($\alpha = 1$) of Eq. (7.9)

$$\mathcal{C}(t) = \int_0^t d\tau_1 \int_0^{\tau_1} d\tau_2 \sum_n |c_n|^2 \tilde{C}_n(\tau_1-\tau_2) - 2P_2t^2 \tag{7.17}$$

where

$$\tilde{C}_n(t-t') = 2\left(1+\sum_\gamma \sigma_{n\gamma}^2 \cos\left[(E_\gamma^{(0)}-E_n^{(0)})(t-t')\right]\right);\ P_2 = \sum_n |c_n|^4 \tag{7.18}$$

$E_j^{(0)}$ is the j^{th} eigenvalue of $\hat{H}_0$, and P_2 is the IPN of the initial state preparation. The LRT approximation using this correlation is plotted in Fig. (7.6) as solid lines, and captures the decays of the two upper panels (perturbative regimes) nicely.

[†]Our calculation of Eqs.(7.16-7.17) is applicable for perturbation strengths $x < x_{prt}$, where x_{prt} is calculated in Appendix B.7 and the correlator is calculated in Appendix B.6. The border x_{prt} defines the limits of validity of infinite order perturbation theory.

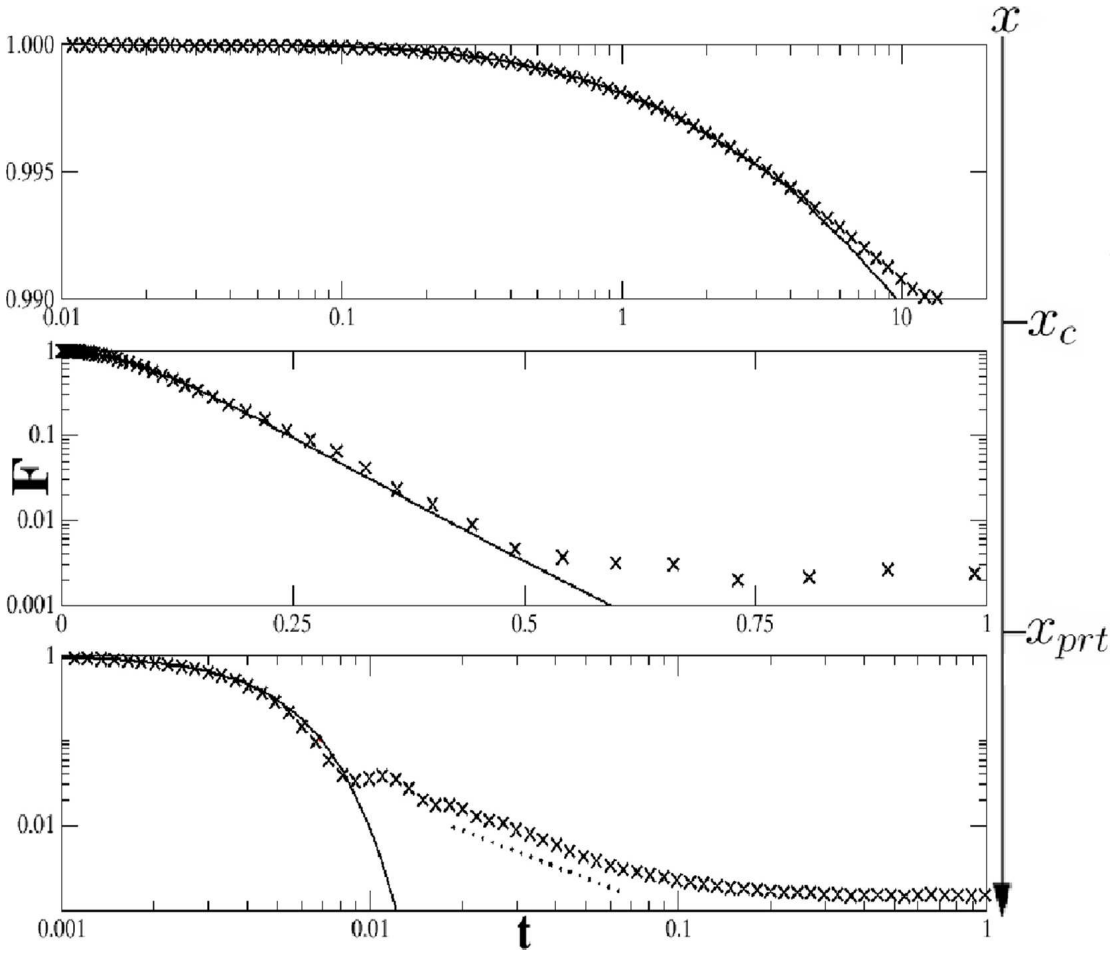

Figure (7.6): Critical Fidelity in three regimes for an initial ES, with system parameters of $L = 1000$, $b = 10$. The top panel is for $x = 0.01$, the standard perturbative regime. The middle panel is for $x = 0.8$, the Wigner(FGR) regime. The bottom panel is for $x = 20$, the non-perturbative regime. The regime boundaries in this simulation are $x_c = 0.59$ and $x_{prt} = 1.58$. In all panels, the solid lines are the analytic LRT results, Eq.(7.16). The crosses are the data from numerical simulations. The dotted line in the non-perturbative regime is drawn to illustrate the novel power-law behavior in the fidelity.

7.3.2 Non-perturbative Regime

For $x > x_{prt}$, LRT fails to reproduce the fidelity decay. Our expectation based on the discussion of Chapter 3 is that we will have an initial Gaussian decay for very short times (the quantum Zeno effect, so $t < t_Z \sim x^{-1}$) followed by an exponential decay with a rate independent of the perturbation strength. However, for critical systems modeled by WLRM, the fidelity decay behaves quite differently. The initial Zeno Gaussian decay remains applicable, as can be seen by the initial match with the LRT approximation in the lower panel of Fig. (7.6), but a novel power-law decay is observed to follow. The power-law decay is observed to be independent of x, but maintains a dependence on b, as illustrated in the left panel of Fig. (7.7). This comes as no suprise, since if an initial state is chosen to be an eigenfunction of either $H_{1,2}$, the fidelity collapses to the calculation of the survival probability (see relevant discussion in Chapter 3). The survival probability for critical systems has been shown [111] to decay as

$$P(t) \sim t^{-D_2^{\mu}} \tag{7.19}$$

For WLRM, the system is one-dimensional, so $D_2^{\psi} = D_2^{\mu} = D_2(b)$. Motivated by this, we first take an integrated time average of the fidelity, in order to smooth the statistical fluctuations seen in the left of Fig. (7.7)

$$F_I(t) = t^{-1} \int_0^t F(\tau) d\tau \tag{7.20}$$

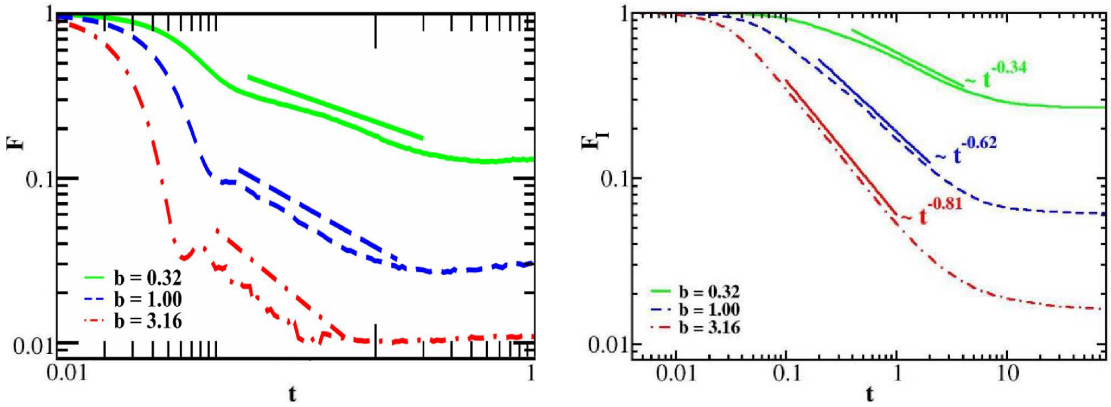

(a) Critical fidelity, non-perturbative regime. **(b)** Integrated time average of critical fidelity.

Figure (7.7): The left panel is the fidelity in the non-perturbative regime for $L = 5000$. The right panel is the integrated time average of the fidelity, for $L = 1000$. The initial state is ES in both, and the perturbation strength is $x = 5$. The different curves in each plot correspond to different bandwidths, $b = 0.32, 1, 3.16$, respectively the solid, dashed, dot-dashed lines. In both, a novel power-law decay is seen after an initial Gaussian decay, of which the straight lines are power-law best fits. Within the integrated time average, the power-law decays are much more observable, with the best-fit parameter of γ in Eq. (7.21).

The integrated time average can be seen to strengthen the power-law portion of the decay, as seen in the right panel of Fig. (7.7). A power-law of

$$F(t), F_I(t) \propto t^{-\gamma} \tag{7.21}$$

is fit to the numerical data and the parameter γ is extracted - actual numerical values for γ are shown in Fig. (7.7).

Since the survival probability shows a power-law exponent given by D_2, it is natural to question whether the fidelity - regardless of initial state - will also

display similar behavior. The fitting parameter γ is extracted for a variety of b for both initial HS and ES, and compared to the average D_2^{ψ} calculated numerically, via Eq. (7.6), for the eigenfunctions of $H_{1,2}$.

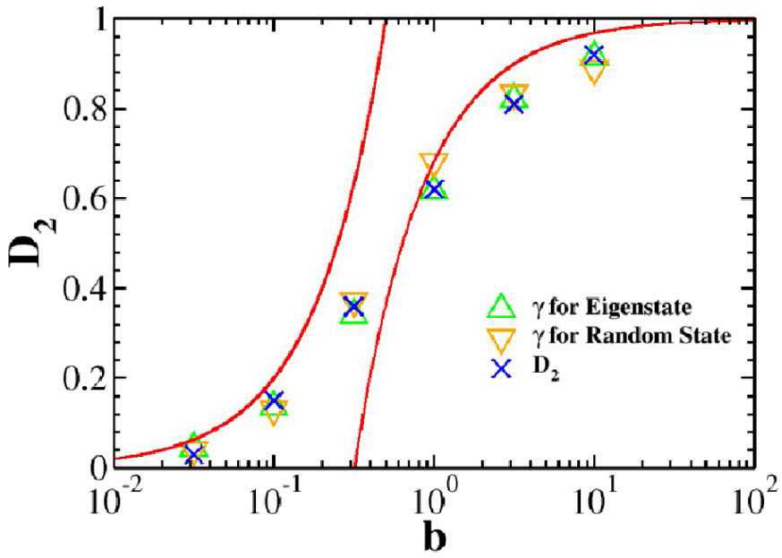

Figure (7.8): The b dependence for the numerical D_2 from Eq.(7.6) (crossmarks), and γ from a power-law fit of the fidelity with both an initial RS (inverted triangle), and an initial ES (triangle). The error bars are on the order of the marker size. The solid lines are the field-theoretical results of Eq. (7.10). A very nice correspondence is seen, such that we can say $\gamma \sim D_2$.

A beautiful correspondence is shown to exist, as evidenced in Fig. (7.8), therefore we can simply state from the numerical results

$$F(t) \propto t^{-D_2(b)} \tag{7.22}$$

7.3.3 A Heuristic Interpretation

Numerically, it has been shown that $\gamma \sim D_2$; however, we would like here to provide an heuristic argument, illustrated in Fig.(7.9), that aims to explain the numerical findings - in particular, the novel power-law of Eq.(7.22). For any finite Hilbert space the fidelity, $F(t)$, approaches the value

$$\lim_{t\to\infty} F(t) \simeq L^{-d}, \tag{7.23}$$

being the inverse of the dimension of the Hilbert space (recall for the WLRM model, $d = 1$). If the dynamics, however, take place in a space with an effective reduced dimension of D_2, we will have[†]

$$\lim_{t\to\infty} F(t) \simeq L^{-D_2}, \tag{7.24}$$

Assuming a power-law decay, Eq.(7.22) for the fidelity, we can estimate a *break time* of t_*, at which point

$$F(t_*) \sim \lim_{t\to\infty} F(t) \tag{7.25}$$

In particular, we are interested in how t_* scales with L, *i.e.*

$$t_* \sim L^{D_2^{\psi}/\gamma} \tag{7.26}$$

[†]For $x > x_{prt}$, the wavefunctions are fractal and therefore fill only a fraction of the available space with an effective dimensionality given by D_2^{ψ} [126].

Noting that the dynamics of a critical system is characterized by an anomalous diffusive law [111] which defines the time needed to explore the available Hilbert space of L as

$$L^2 \sim t_*^{2D_2^\mu/D_2^\psi} \longrightarrow t_* \sim L^{D_2^\mu/D_2^\psi} \tag{7.27}$$

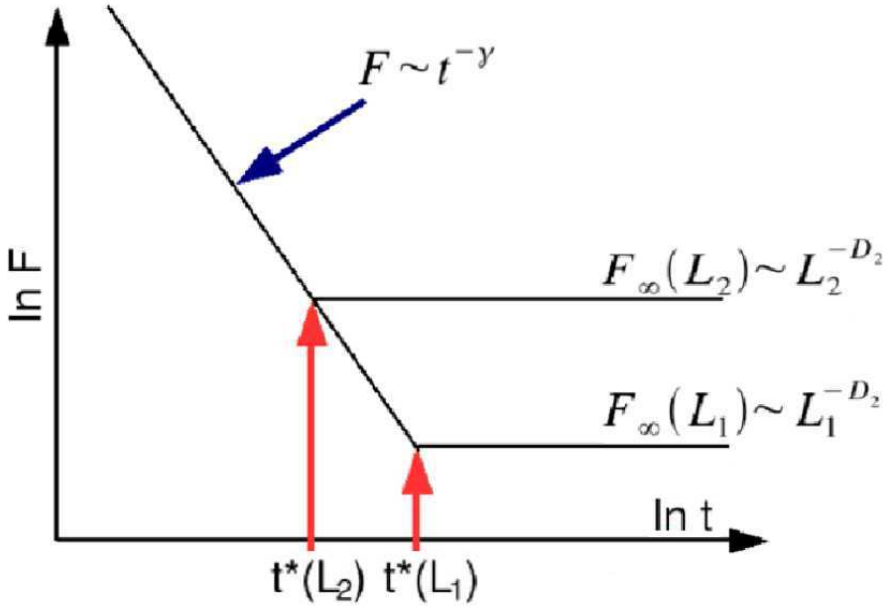

Figure (7.9): A sketch illustrating the heuristic explanation of why $\gamma \sim D_2^\mu$. For a given bandwidth, finite-size effects from two different system lengths, $L_{1,2}$, only manifest in long timescales. The fidelity plateau, $F_\infty(L)$ must connect at some point to the power-law decay. The diffusive timescale for critical systems is anomalous with the correlation dimensions $t \sim L^{D_2^\psi/D_2^\mu}$, which can be used at the connection point between the two different fidelity behaviors to obtain the relation $\gamma = D_2^\mu$. Since the WLRM is one-dimensional, $D_2^\mu = D_2^\psi = D_2$, and the relation $\gamma = D_2(b)$ is confirmed.

Equating the two expressions for t_* we arrive at

$$\gamma \sim D_2^\mu \tag{7.28}$$

Although the numerical results leave no doubt on the validity of Eq.(7.22), a rigorous mathematical proof is much more desirable.

7.4 Conclusion

In conclusion, the fidelity decay of systems at a critical MIT point has been studied, using a one-dimensional critical RMT model, the WLRM. The three regimes of fidelity from Chapter 3 have been identified, and fidelity has been shown to follow LRT approximations in the two regimes $x < x_c$, $x_c < x < x_{prt}$. The third regime $x > x_{prt}$ deviates from the fidelity expectations in Chapter 3, rather the fidelity displays a novel power-law decay that is governed by the critical behavior of the system - manifested in a bandwidth parameter b. Lastly, it has been shown via numerical and heuristic arguments that the power-law exponent in the novel fidelity decay is equivalent to the correlation dimension $D_2(b)$.

Chapter 8

Synopsis

A conclusion is the place where you got tired of thinking.

-Harold Fricklestein

The study of fidelity has intensified in the past decade - largely motivated by a wide array of physics; ranging from atomic systems, microwaves and elastic waves to quantum information and quantum chaos. It has been adopted as a standard measure for quantum reversibility and stability of quantum motion with respect to an external perturbation, linked to the concept of dephasing in mesoscopic devices. The main contribution of this dissertation was to bring the notion of fidelity into a new arena of disordered mesoscopic systems and utilize it in order to quantify localization phenomena. We have developed a theoretical framework for the temporal behavior of fidelity decay based on Random Matrix Theory modeling. In this picture, we have addressed not only the diffusive and localized regimes, but also the Anderson metal-insulator critical transition. The fidelity displays a novel

power-law decay at this point, governed by the critical (multifractal) structure of the eigenfunctions. Although the body of our contribution was theoretical, we have also proposed and executed an experiment in order to compare our theoretical predictions of fidelity decay for localized systems. Using disordered microwave cavities, we have calculated the fidelity both in the diffusive and the localized regimes. The experimental results were in excellent agreement with our theoretical predictions.

Far from the closing chapter, our work is only a beginning. The future applications of fidelity are quite widespread. Motivated by our results for disordered systems at the Anderson transition, the fidelity decay was recently studied in the framework of dynamical systems showing critical chaos [107]. The natural next step is to experimentally study the fidelity decay for critical systems. A promising candidate in this direction is 1D microwave cavities with quasi-periodic arrangements of scatterers. This experimental set-up was used in the past [105,128] from the Marburg group in order to demonstrate anomalous transport in Harper-like structures. The study of surface roughness (in contrast to bulk disorder used throughout this dissertation) using fidelity is another interesting avenue of investigation. Finally, most of the work presented here involved phase transitions for non-interacting systems. Current progress within ultracold atoms in optical lattices opens the possibility to investigate fidelity at the phase-transition from a Mott insulator to a superfluid [129,130], allowing investigation of phase transition due to interactions. In the words of the great Tom Petty, "The future is wide open..."

Appendix A

Delay Time Rescaling

Delay may give clearer light as to what is best to be done.

-Aaron Burr

In Chapter 5 it was established that random disorder within a 1D system provides a means for the eigenstates to localize exponentially. In the case of infinitely-sized systems, this localization is characterized by the localization length, l_∞. The question of finite-size effects on localization has been thoroughly investigated for a variety of random/random-like systems [131–135]. Via rescaling of the q'-moments for these characteristic eigenstate length scales, $l_\infty^{q'}(\epsilon, E)$, and their finite-system counterparts (of size N), $l_N^{q'}(\epsilon, E)$, a suitable scaling law has been developed

$$\frac{1}{l_N^{q'}(\epsilon, E)} = \frac{1}{l_\infty^{q'}(\epsilon, E)} + \frac{1}{l_N^{q'}(0, E)} \tag{A.1}$$

where $l_N^{q'}(0, E)$ is a moment for a purely-ordered lattice. E, N, ϵ are respectively the system energy, system size, and disorder strength. The question we ask is

"Are there other measures that exhibit similar scaling?"

A.1 The Wigner Delay Time

Another measure with the potential to probe a complex system is present in the *Wigner delay time* [136–138], which can be interpreted as a time delay in propagation of the peak of the wavepacket due to scattering interference, in comparison to a free wavepacket propagation; see Fig.(A.2). It is defined in the following analytical fashion. The elements of the scattering matrix, Eq.(6.12), can be written as $S_{ab} = |S_{ab}| \exp(i\phi_{ab})$. For the m^{th} channel, the total phase in the channel is $\phi_m = \sum_j \phi_{jm}$. The Wigner delay time is then defined as the phase change with energy across all the channels

$$\tau(E) = \sum_{m=1}^{M} \frac{d\phi_m}{dE} \tag{A.2}$$

Recent investigations between properties of Wigner delay times and eigenstates [139, 140] beg the question of similar scaling behavior as Eq.(A.1) for the delay times - the motivation being "How do finite-size distributions converge to an asymptotic distribution?" Fig.(A.1) illustrates such convergence for the standard Anderson model, of Eq.(5.4), in which the delay-time distribution approaches (in the lower portion) the $N \to \infty$ limit of

$$\mathcal{P}(\tau) = \frac{l_\infty}{v\tau^2} \exp\left(\frac{-l_\infty}{v\tau}\right); \quad v = |\partial E/\partial k| \tag{A.3}$$

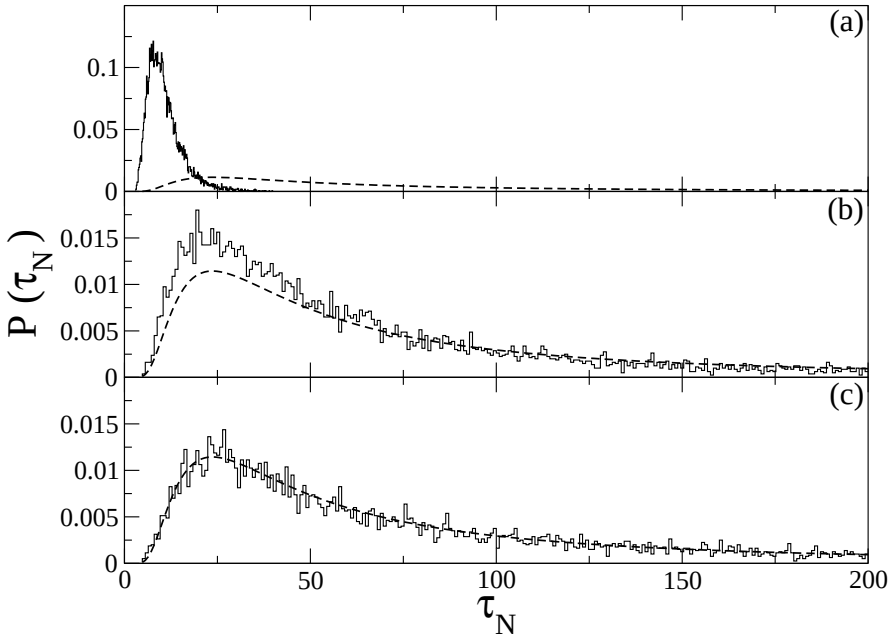

Figure (A.1): Three normalized distributions for various lengths in the standard Anderson model, $\epsilon = 0.5, k = \sqrt{\pi}$ (a) $N = 10$, (b) $N = 10^2$, (c) $N = 10^7$. The dotted line corresponds to the $N \to \infty$ fit, where $l_\infty/v \simeq 47$.

The $q' = 2$ information length, $l_N^2(\epsilon, E)$ is associated with the inverse participation number and measures the "penetration" (*i.e.* localization) length inside a disordered sample before the wavepacket is reflected back (in a one channel scattering setup), as in Fig.(A.2). The corresponding delay time due to disordered scattering is given by $\tau_N = 2l_N^2/v_g$, where v_g is the group velocity of the wavepacket centered around energy E. Substituting τ_N for l_N to Eq.(A.1) gives a similar rescaling for the delay time

$$\left\langle \tau_N^{-q}(\epsilon, E) \right\rangle = \left\langle \tau_\infty^{-q}(\epsilon, E) \right\rangle + \tau_{\rm ref}^{-q} \tag{A.4}$$

where $q = q' - 1$, and $\tau_{\rm ref}$ only depends on finite sample length information.

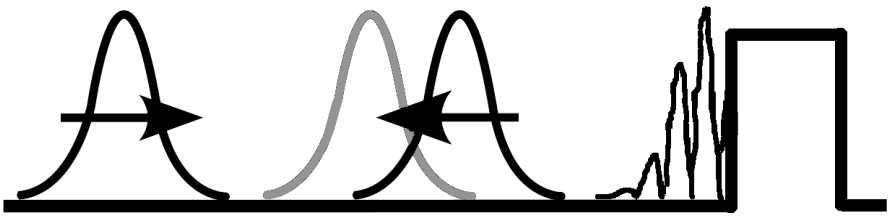

Figure (A.2): Description of Wigner delay time. The left-most packet is an incident Gaussian from the left channel with a peak position of $x(t) = x_0 + v_0 t$ and a group velocity of $v_0 = \hbar k_0/m$. It approaches a Heaviside potential and scatters. If there is no interference, the result is a free propagation reflection; *i.e.* all phases are reversed by π, giving a peak position after scattering of $x(t) = x_0 - v_0 t$. This is presented by the grey packet. However, if potential tunneling occurs, there is interference in the wavepacket - as seen by the sketch near the potential. Eventually, the Gaussian reforms, but it's peak position is shifted, such that $x(t) = x_0 - v_0 t + \alpha\tau(E)$ where $\tau(E)$ is the Wigner delay time, with the prefactor $\alpha = \sqrt{2\hbar E(k_0)/m}$.

Theoretically, eigenstates and delay times are related through a nonlinear σ model (NLσM) [141,142]; however, in the region of strong disorder, the validity of NLσM remains questionable. Recent work [143] assumes that any microscopic system and its mapping to the NLσM converge to the same fixed point under renormalization, thusly sharing the same critical exponents. We aim to test this assumption under adverse conditions, namely various microscopic systems that by their construct, do not show any diffusion and contain strong disorder. At this point, we postulate that Eq.(A.4) is universal and independent of the particular microscopic arrangement, which we will now numerically prove.

A.2 Method of Analysis

Consider a one-dimensional disordered sample that is described by the tight-binding equation of Eq.(5.4), such that

$$\psi_{n+1} + \psi_{n-1} = (E(k) - V_n)\,\psi_n \tag{A.5}$$

where the wavefunction amplitude at the n^{th} site is given by ψ_n, $n \leq L$. The system energy, $E(k)$, and the disordered potential V_n are system-specific. We open the sample by attaching one channel to the first site $n = 1$. The Wigner delay time of a sample of length $n + 1$ is then evaluated with the use of the Hamiltonian map [144]

$$\begin{aligned} x_{n+1} &= x_n \cos k + (p_n - A_n x_n) \sin k \\ p_{n+1} &= -x_n \sin k + (p_n - A_n x_n) \cos k, \end{aligned} \tag{A.6}$$

an interated half-phase can be derived [144], where A_n is proportional to the random V_n,

$$\tan(\phi_{n+1}) = \tan(\phi_n - k) + A_n, \tag{A.7}$$

as well as an iterated delay-time

$$\begin{aligned} \tau_{n+1} &= G_n^{-1}\left(\tau_n + \tfrac{1}{\sin k}\right) + \tfrac{A_n}{1+[\tan(\phi_n - k)+A_n]^2}\tfrac{\cot k}{\sin k}, \\ G_n &= 1 + A_n \sin\left[2(\phi_n - k)\right] + A_n^2 \cos^2(\phi_n - k), \end{aligned} \tag{A.8}$$

This iterative scheme allows calculation of powers of delay times for any system length, τ_N^q, limited only by computational power. The initial values are uniformly randomized, such that $\tau_0 \in (0,1], \phi_0 \in (0, 2\pi]$. The resulting values of τ_N^q are averaged over a set of 10^4 such initial random realizations. The averaged moments are then rescaled by [135]

$$\beta_q = \frac{(2N)^q}{\langle \tau_N^q \rangle \cdot v^q} \tag{A.9}$$

The data is then plotted against an abcissa of the rescaled infinite case

$$\lambda_q = \frac{(2N)^q}{\langle \tau_\infty^q \rangle \cdot v^q} \tag{A.10}$$

From the Anderson case shown in Figure A.1, we take $N = 10^7 \sim \infty$.

A.3 Systems of Interest

Since we are interested in testing the re-normalization claim of [143], we investigate realistic systems of various microscopic origins. For each system, we use a unit lattice spacing and calculate the delay times according to the tight-binding iterative result, Eq. (A.8). For $N \in \{10, 10^2, 10^3, ..., 10^6, 10^7\}$, we find from the

delay times β_{-1}, λ_{-1} according to Eqs.(A.9,A.10) and present for each microscopically different system the data for the system energies and disorder strengths described below.

A.3.1 1D Disordered Electronic System

As the *coup* of disordered systems, we present the standard Anderson system as a benchmark - where in Eq.(A.8), we use

$$E(k) = 2\cos k; \quad A_n = \frac{\epsilon_n}{\sin k} \tag{A.11}$$

in which $\epsilon_n = \epsilon \cdot \zeta_n$. The value of ζ_n is a random uniform deviate, $|\zeta_n| \in (0, 1]$, and ϵ is the disorder strength. We utilize both weak ($\epsilon < 1$) and strong disorder strengths, whose values are given in Fig.(A.3). Since much has been done in scaling phenomena of the localization lengths of the Anderson model, we include the case of $l_N/N, \lambda = 2l_\infty/N$ for comparison. The scaled data for $q = 1$ and $q = 2$ (inset) fall on a single curve - for various N and disordered strengths ϵ - confirming the validity of the theoretical prediction, Eq.(A.4). The agreement between information lengths and delay times is evident, thus confirming that these two quantities are directly related.

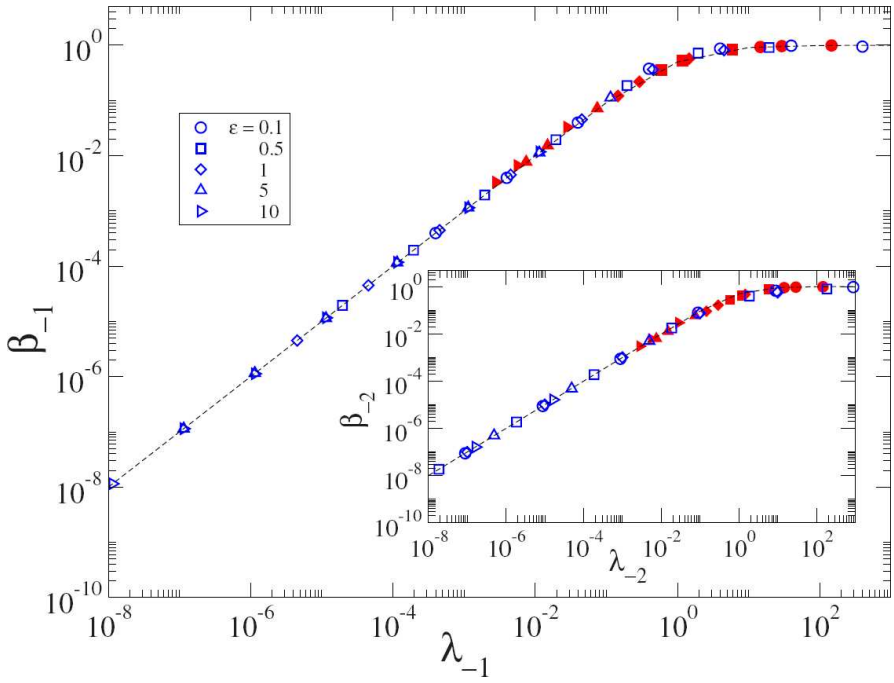

Figure (A.3): Scaled inverse delay times for the Anderson model. Various symbols correspond to different disordered potentials $\epsilon \in \{0.1, 0.5, 1, 5, 10\}$ and $|E(k = \sqrt{\pi})| < 1$. Blue hollow symbols denote delay time data for $q = 1$. For comparison, red solid symbols denote $q' = 2$ information length data, i.e., $l_N^{q'}/N$ vs. $\lambda = 2l_\infty^{q'}(\epsilon, E)/N$. The dashed line is the result of the best fit from Eqs.(A.22, A.23). Inset: same as in the main figure but now $q = 2$ for delay times and $q' = 3$ for information lengths.

A.3.2 Microwaves Propagating in a 1D Waveguide

Due to their immediate technological applications, creation of frequency pass and/or stop bands separated by mobility edges and their manipulation by imposing appropriate correlations in the disordered potential [145–158] have recently gained considerable research interest. One prominent theoretical suggestion [145] was based on the introduction of long range correlations in the on-site disordered

potential. The theoretical predictions were further supported by subsequent experimental microwave measurements [146]. If the scatterers within these correlated experiments are approximated as delta scatters, the system can be described by the Kronig-Penny wave equation, which reads in discrete form

$$\psi_{n+1} + \psi_{n-1} = (E(k) - U_n \cdot k \sin(k))\, \psi_n \tag{A.12}$$

If the random potential is separated into mean and fluctuative terms, $U_n = \epsilon + \epsilon_n$, the tight-binding equation (A.5) is recovered, such that Eq.(A.11) becomes

$$E(k) = 2\cos k + k\langle U_n \rangle \sin(k); \quad A_n = \frac{\epsilon_n}{k} \tag{A.13}$$

The long-range correlation is then defined by [145]

$$\epsilon_n = \epsilon \sum_{m=-\infty}^{\infty} \xi_m \cdot \zeta_{n+m} \tag{A.14}$$

where $\zeta_{n+m} \in (0, 1]$ is a random uniform deviate and

$$\xi_m = \frac{2}{\pi} \int_0^{\pi/2} \sqrt{\phi(\mu)}\, \cos(2\mu m) d\mu. \tag{A.15}$$

The correlated sequence of $\{\epsilon_n\}$ can be made to correspond to a Heaviside dependence of the normalized Lyanpunov exponent, $\Lambda_0(E) = (2/3)\phi\,[\mathrm{a}\cos(E/2)]$, such

that $\Lambda_0 = 0$ for $|E| < 1$ and $\Lambda_0 = 1$ for $1 < |E| < 2$. This yields

$$\xi_m = \frac{3}{2\pi m} \sin\left(\frac{2\pi m}{3}\right) \tag{A.16}$$

which can be re-written by constructing a random potential such that

$$\phi(\mu) = \begin{cases} C_0^2, & 0 < \mu_1 < \mu < \mu_2 < \pi/2 \\ 0, & \mu < 1; \mu_2 < \mu < \pi/2 \end{cases} \tag{A.17}$$

where $C_0^2 = \frac{\pi}{2}(\mu_2 - \mu_1)$. From Eq.(A.15), the correlators become

$$\xi_m = \begin{cases} \frac{2C_0}{\pi}(\mu_2 - \mu_1), & m = 0 \\ \frac{C_0}{\pi m}\left[\sin(2m\mu_2) - \sin(2m\mu_1)\right], & m \neq 0 \end{cases} \tag{A.18}$$

We truncate to 300 correlators, $m \in [-300, 300]$, for the disorder strengths $\epsilon \in \{0.1, 0.5, 2.5, 5\}$. Using the parameters $\mu_1 = 0.2\pi$, $\mu_2 = 0.4\pi$, and $\epsilon = -0.1$, we then scale the data for energies on either side of the mobility edge $|E(k = 0.5\pi)| < 1, |E(k = 0.7\pi)| > 1$. Our results, using the rescaled variables of Eqs.(A.10, A.9) are presented in Fig.(A.4). The remarkable agreement between the data from both sides of the mobility edge confirms again our theoretical prediction, Eq.(A.4), and indicates clearly that the corresponding eigenfunctions have the same structural properties, being unaffected by the potential correlations. Using the Wigner delay time scaling properties, we conclude that $k = 0.57\pi$ does not correspond to any mobility edge separating diffusive from exponentially localized eigenstates.

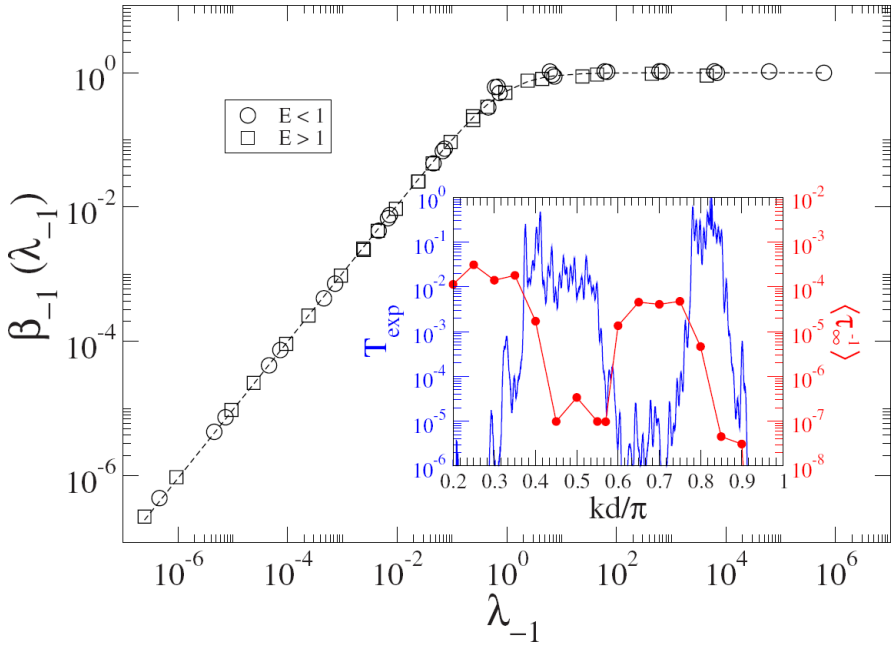

Figure (A.4): Scaled inverse delay times for microwaves propagating in a correlated 1D waveguide. The different symbols correspond to the energies $|E(k = 0.5\pi)| < 1, |E(k = 0.7\pi)| > 1$, being on both sides of the critical wave vector $k = 0.57\pi$. A nice data collapse is observed, indicating that in both cases, the statistical properties of delay times (and thus the structural properties of wave functions) are unaffected by the correlation and correspond to exponentially localized wave functions; albeit the localization length for $k = 0.5\pi$ is much larger than for $k = 0.7\pi$. This is reflected in the overall scaling parameter $\langle \tau_\infty^{-1} \rangle$. The dashed line is the result of the best fit from Eqs.(A.22, A.23). Inset: the experimental transmission coefficient (courtesy U. Kuhl) showing pass and stop bands is displayed by the blue line (left axis). The values for $\langle \tau_\infty^{-1} \rangle$ are shown by the red circles (right axis).

Rather, in both energy regimes, the eigenstates are structurally the same (exponentially localized), albeit the localization length is drastically different, reflected in the overall scaling factor $\langle \tau_\infty^{-1} \rangle$, illustrated by the red circles (right axis) within the inset of Fig.(A.4). Note that $\tau_\infty \sim l_\infty$ [144]. As we can see from the figure, at the pass-band region $\langle \tau_\infty^{-1} \rangle$ is much smaller than that of the stop-band region.

This means l_∞ is much larger in the pass-band, yet remains finite. This is to be contrast with a true mobilty edge transition, which implys that $\langle \tau_\infty^{-1} \rangle \sim N^{-1}$ - the scaling factor must disappear as the system size increases for a true transition. This abrupt change in the magnitude of $\langle \tau_\infty^{-1} \rangle$ around $k = 0.57\pi$ is a fingerprint of the imposed disorder correlations; regardless, the proposed universal scaling law of Eq.(A.4) is again verified.

A.3.3 Disordered Optical Lattice

Given the growth of experimental interest in Bose-Einstein condensates, the last microscopic system investigated is a disordered cold atom lattice [77]. Within this system, cooled vibrational ground-state atoms trapped at the nodes of a periodic optical lattice act as delta scatterers if the kinetic energy of incoming particles (subscript "i") is less than the vibrational energy of the trapped scatterer (subscript "s")

$$\frac{\hbar^2 k^2}{2m_i} \ll \hbar\omega_s \tag{A.19}$$

In the Born regime, the disorder strength is given by

$$\epsilon = 2\hbar \frac{\omega_i \omega_s}{\omega_i + \omega_s} a \tag{A.20}$$

where a is the free space scattering length. We take $m_s = m_i = m, \omega_s = \omega_i$. From [77], the Born regime places a condition on the disorder strength, such that $m\epsilon/\hbar^2 \ll 15$. Localization is then dependent on three parameters: momentum k,

disorder strength ϵ, and the filling factor p.

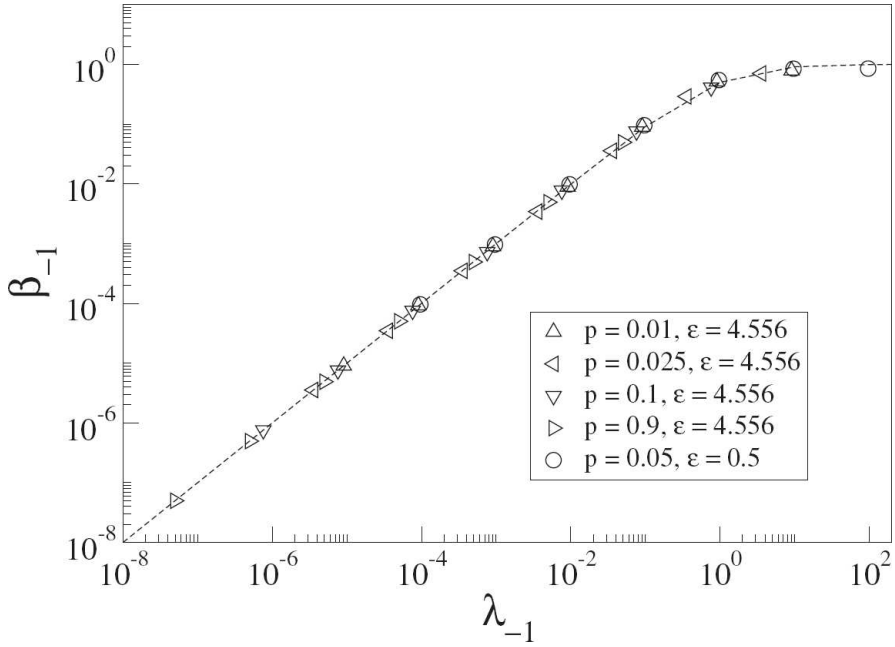

Figure (A.5): Scaled inverse delay time for the disordered optical lattice system, with $\epsilon \in \{4.556, 0.5\}$ and filling factor $p \in \{0.01, 0.025, 0.05, 0.1, 0.9\}$. The dashed line is the result of the best fit from Eqs.(A.22, A.23).

The filling factor, $p \in [0, 1]$, dictates a binomial-like correlation

$$\epsilon_n = \begin{cases} \epsilon, & \zeta_n < p \\ 0, & \zeta_n \geq p \end{cases} \tag{A.21}$$

where ζ_n is a random uniform deviate. Since the disorder is a Kronig-Penny type, Eq.(A.13) can be used in Eq.(A.8). For this case, we use the disorder strengths $\epsilon \in \{4.556, 0.5\}$ and the filling factors $p \in \{0.01, 0.025, 0.05, 0.1, 0.9\}$. The larger

disorder strength corresponds to numerical values used in Ref. [77]. We present our results in Fig.(A.5). Yet again, the rescaled delay times match excellently with the proposed universal scaling law of Eq.(A.4).

A.4 Universal Behavior

From Figures (A.3-A.5) we see that there is very similar behavior in the scaling. Plotting the data for all three systems in the variables [135]

$$Y_q = \ln\left(\frac{\beta_q}{1-\beta_q}\right), \quad X_q = \ln\left(\lambda_q\right) \tag{A.22}$$

yields the scaling of β_q shown in Figure A.6. For $q = 1$ the above scaling reduces to a simple linear form

$$Y_{-1} = a_{-1} + b_{-1}X_{-1} \tag{A.23}$$

For all three systems, a value of $q = 1$ gives $b_{-1} \approx 1$ and $a_{-1} \approx 0$ to best fit[†]. The result that the above simple scaling relation holds in a large range of the scaling parameter, $\Delta X_{-1} \sim 14$. Eq.(A.23) is exact only for $q = 1$ [85, 159, 160]. For smaller values of $q > 1$, Eq.(A.23) remains a good approximation - this is shown in the inset of Fig.(A.6), however, small deviations from linear are evident around $X_{-2} = 0$.

[†]The values of a_{-1} to best fit are exactly 0.077 for the Anderson system, 0.033 for the correlated microwave (Kronig-Penny) system, and 0.038 for the disordered optical lattice system.

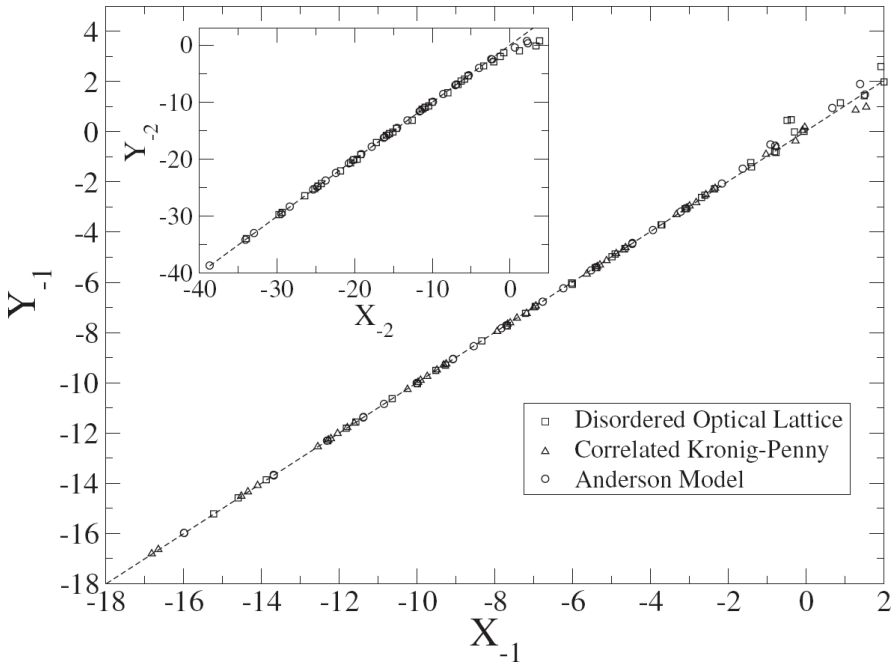

Figure (A.6): Scaling of Eqs.(A.10, A.9) in the variables from Eq.(A.22). Inset: same as in the main figure but now for the $q = 2$ case. Note that the three systems, all with different microscopic disorder behaviors, follow the universal scaling of Eq.(A.4).

A.5 Conclusion

In conclusion, we investigated scaling properties of inverse moments of Wigner delay times. We proposed they are dictated by the scaling law, Eq.(A.4), motivated by similar scaling relations for the information lengths of wave function components. Our theoretical arguments were tested with various physical models where the applicability of NLσM is questionable, thus strongly supporting the relation between the moments of wavefunctions and the inverse moments of Wigner delay times [4].

Appendix B

Miscellaneous Derivations and Concepts

I find that a great part of the information I have was acquired by looking up something and finding something else on the way.

-Franklin P. Adams

B.1 Spectral Quantum-Classical Correspondence

The **classical** energy-averaged correlator, $\langle \mathcal{C}(\tau) \rangle_j$ can be related to the variance of the perturbing **quantum** operator via

$$\begin{aligned} \langle \mathcal{C}(\tau) \rangle_j &= \langle \mathfrak{f}(\tau) \cdot \mathfrak{f}^*(0) \rangle_j \\ &= \langle j | \hat{B}(\tau) \hat{B}(0) | j \rangle \end{aligned} \tag{B.1}$$

Applying a Dirac formalism (see next section) we get

$$\begin{aligned}
\langle \mathcal{C}(\tau) \rangle_j &= \langle j | \, (e^{i\hat{H}_0 t/\hbar} \hat{B} e^{-i\hat{H}_0 t/\hbar}) \hat{B} \, | j \rangle \\
&= e^{iE_j^0 t/\hbar} \langle j | \, \hat{B} e^{-i\hat{H}_0 t/\hbar} \sum_k |k\rangle \langle k| \, \hat{B} \, | j \rangle \\
&= \sum_k e^{iE_j^0 t/\hbar} e^{-iE_k^0 t/\hbar} \langle j | \, \hat{B} \, | k \rangle \langle k | \, \hat{B} \, | j \rangle \\
&= \sum_k |B_{jk}|^2 e^{i\omega_{jk}^0 t} \qquad \text{(B.2)}
\end{aligned}$$

in which the last equation yields Eq.(2.12). Turning the sum to an integration weighed with the density of states $g(E_k^0)$ and performing the integrations gives

$$\begin{aligned}
\langle \mathcal{C}(\tau) \rangle_j &= \frac{1}{2\pi} \int \tilde{C}(\omega) e^{i\omega t} d\omega \\
&= \sum_k |B_{jk}|^2 e^{i\omega_{jk}^0 t} \\
&= \int g(E_k^0) |B_{jk}|^2 e^{i\omega_{jk}^0 t} dE_k^0 \\
&= \int g(\hbar\omega) \left\langle |B_{jk}|^2 \right\rangle_j e^{i\omega t} \hbar d\omega \qquad \text{(B.3)}
\end{aligned}$$

Taking the inverse fourier transform then yields the end result of Eq.(2.13)

$$\frac{\tilde{C}(\omega)}{2\pi\hbar g(E_k^0)} = \left\langle |B_{jk}|^2 \right\rangle_j \qquad \text{(B.4)}$$

B.2 The Dirac Formalism

In order to perform a perturbative approach to fidelity, we need to consider a Dirac formalism (i.e. "picture"). Recall from quantum mechanics, the *Schrödinger formalism* (which we've largely been working in), is

$$\left|\psi^S(t)\right\rangle = \hat{U}(t)\left|\psi^S(0)\right\rangle \tag{B.5}$$

$$\hat{A}^S(t) = \hat{A}^S(0) \tag{B.6}$$

where the superscript S denotes the Schrödinger formalism. In this picture, the wavefunction evolves in time while the observable operations remain stationary. In the *Heisenberg formalism*, it is vice-versa - the wavefunctions remain stationary (akin to a body-centered reference frame in classical dynamics) and the observable operations change in time

$$\left|\psi^H(t)\right\rangle = \left|\psi^H(0)\right\rangle, \tag{B.7}$$

$$\hat{A}^H(t) = \hat{U}(t)\hat{A}^H(0)\hat{U}^\dagger(t) \tag{B.8}$$

where the subscript H denotes the Heisenberg formalism. In both pictures, observable expectations remain invariant. The Dirac formalism arises when one speaks of interactions, such as with a parametric Hamiltonian (hence its more popular moniker, the 'interaction picture'). The interaction is generally time-dependent,

so in this formalism the observable operations evolve with $\hat{H}_0$

$$\hat{A}^D(t) = \hat{U}_0(t)\hat{A}^D(0)\hat{U}_0^\dagger(t) = \exp(i\hat{H}_0 t/\hbar)\hat{A}^D(0)\exp(-i\hat{H}_0^\dagger t/\hbar) \tag{B.9}$$

and the wavefunctions evolve with $\pm x\hat{B}(t)$ (depending on which $\hat{H}_{1,2}$ is used - note we are using $\hat{H}_{1,2} = \hat{H}_0 \pm x\hat{B}$)

$$\begin{aligned}
\left|\psi^D(t)\right\rangle &= \exp(i\hat{H}_0 t/\hbar)\left|\psi^S(t)\right\rangle \\
i\hbar\frac{\partial}{\partial t}\left|\psi^D(t)\right\rangle &= i\hbar\frac{\partial}{\partial t}\left(\exp(i\hat{H}_0 t/\hbar)\left|\psi^S(t)\right\rangle\right) \\
&= -\hat{H}_0\exp(i\hat{H}_0 t/\hbar)\left|\psi^S(t)\right\rangle + \exp(i\hat{H}_0 t/\hbar)(\hat{H}_0 \pm x\hat{B}(t))\left|\psi^S(t)\right\rangle \\
&= \pm x\hat{B}(t)\left(\exp(i\hat{H}_0 t/\hbar)\left|\psi^S(t)\right\rangle\right) \\
i\hbar\frac{\partial}{\partial t}\left|\psi^D(t)\right\rangle &= \pm x\hat{B}(t)\left|\psi^D(t)\right\rangle
\end{aligned} \tag{B.10}$$

Eq. (B.10) is called the *Schwinger-Tomonaga equation*, and it plays the role of the time-dependent Schrödinger equation in the Dirac formalism [161]. Additionally, we wish to have a Schrödinger-like evolution in the Dirac formalism, such that

$$\left|\psi^D(t)\right\rangle = \hat{U}_D(t)\left|\psi^D(0)\right\rangle \tag{B.11}$$

The Schwinger-Tomonaga equation gives a Heisenberg-like equation in which $\hat{H}$ is replaced by $\hat{H}_0$. This yields an evolution operator that changes as

$$i\hbar\frac{d}{dt}\hat{U}_D(t) = \pm x\hat{B}(t)\hat{U}_D(t) \tag{B.12}$$

Using this equation and the fact that the evolution must have $\hat{U}_D(0) = 1$, the differential can be integrated

$$\hat{U}_D(t) = 1 \mp \frac{ix}{\hbar} \int_0^t d\tau \hat{B}(\tau) \hat{U}_D(\tau) \tag{B.13}$$

The above equation is transcendental - what we are looking for, $\hat{U}_D(t)$, is also contained in the solution! However, it can be approximated by applying it to itself iteratively, which yields the Dyson series expansion [161] (also called Born approximation)

$$\begin{aligned} \hat{U}_D(t) &= 1 \mp \frac{ix}{\hbar} \int_0^t d\tau \hat{B}(\tau) \left(1 \mp \frac{ix}{\hbar} \int_0^\tau d\tau' \hat{B}(\tau') \left[1 \mp \frac{ix}{\hbar} \int_0^{\tau'} d\tau'' \hat{B}(\tau'') \times \ldots \right] \right) \\ &= 1 \mp \frac{ix}{\hbar} \int_0^t d\tau \hat{B}(\tau) + \left(\frac{ix}{\hbar} \right)^2 \int_0^t d\tau \int_0^\tau d\tau' \hat{B}(\tau) \hat{B}(\tau') + \ldots \end{aligned} \tag{B.14}$$

The Dyson series expansion is then applied to the initial state in Chapter 3.

B.3 The Bose-Hubbard Hamiltonian

The classical Hamiltonian of an interacting bosonic lattice system consists of four terms: the kinetic energy of a boson, a potential from boson-boson interactions, a potential from the lattice, and finally an adiabatic external confining potential, such as the slowly varying trap used in evaporative cooling. This gives a classical

Hamiltonian of

$$H = \frac{p^2}{2m} + V(\mathbf{r} - \mathbf{r}') + V_{\text{lattice}}(\mathbf{r}) + V_{\text{trap}}(\mathbf{r}) \tag{B.15}$$

In second quantization, two raising and lower field operators $\hat{\Phi}(\mathbf{r}), \hat{\Phi}^\dagger(\mathbf{r})$ which annihilate and create bosons respectively at $\mathbf{r}$, are applied on either side of the classical Hamiltonian to yield a quantized version

$$\begin{aligned}\hat{H} = \int d\mathbf{r}\ \hat{\Phi}^\dagger(\mathbf{r}) \left[-\frac{\hbar^2}{2m} \bigtriangledown^2 + V_{\text{lattice}}(\mathbf{r}) + V_{\text{trap}}(\mathbf{r}) \right] \hat{\Phi}(\mathbf{r}) + \\ \frac{1}{2} \int d\mathbf{r} \int d\mathbf{r}'\ \hat{\Phi}^\dagger(\mathbf{r})\, \hat{\Phi}^\dagger(\mathbf{r}')\, V(\mathbf{r} - \mathbf{r}')\, \hat{\Phi}(\mathbf{r}')\, \hat{\Phi}(\mathbf{r})\end{aligned} \tag{B.16}$$

Two simplifications are now made. First, assume both the density and temperature of the bosons is very low, so that the dominant boson-boson interaction is due to s-wave scattering. This simplifies the complicated boson-boson interaction to a contact potential

$$V(\mathbf{r} - \mathbf{r}') \sim \frac{4\pi a_s \hbar^2}{m} \delta(\mathbf{r} - \mathbf{r}') \tag{B.17}$$

where m is the boson mass, and a_s is the s-wave mean scattering length. For the remainder of this derivation (and throughout Chapter 4), we will consider natural units $\hbar = 2m = 1$.

Since the lattice is purely periodic, $V_{\text{lattice}}(\mathbf{r}) = V_{\text{lattice}}(\mathbf{r} + \mathbf{a})$, where $\mathbf{a}$ is the lattice translation vector. For a single quantum particle moving in such a periodic lattice, the eigensolutions are the *Bloch waves and energy bands*. The energies are periodic $E_n(\mathbf{k}) = E_n(\mathbf{k} + \mathbf{K})$, where $\mathbf{K}$ is the reciprocal lattice vector. For

a given index n, the energy is continuously dependent on $\mathbf{k}$, hence we speak of continuous "bands" of energies for a given index. The eigenstates contain a function periodic with the lattice $u_n(\mathbf{r}, \mathbf{k}) = u_n(\mathbf{r} + \mathbf{a}, \mathbf{k})$, enveloped by a plane wave, so the eigenstate is $\psi_n(\mathbf{r}, \mathbf{k}) = \exp(i\mathbf{k}\cdot\mathbf{r})u_n(\mathbf{r}, \mathbf{k})$. The second assumption we make is that the lattice potential has a large enough amplitude that a boson within a given lattice minimum ("site") has the majority of its wavefunction contained in the site - i.e. the boson wavefunction does not 'leak' into other sites. A basis used to describe such a site-localized view is given by the *Wannier functions*

$$W_n(\mathbf{r} - \mathbf{R}) = \frac{1}{\sqrt{f}} \sum_{\mathbf{k}} \psi_n(\mathbf{r}, \mathbf{k}) \exp(-i\mathbf{k} \cdot \mathbf{R}) \tag{B.18}$$

where f is the number of lattice sites. In such a basis then, the degrees of freedom are the number of bosons in each lattice site. If in addition to our assumption of 'large' potential amplitudes, we quantify 'large' so that the Bloch states are confined only to the first band ($n = 0$) of the Bloch energy spectrum, then the bosonic field operators used in second quantization can be written as

$$\hat{\Phi}(\mathbf{r}) = \sum_{i=1}^{f} \hat{b}_i W_0(\mathbf{r} - \mathbf{R}) \tag{B.19}$$

Applying these two simplifications (the local-mode approximation) to Eq. (B.16) yields the following quantum Hamiltonian, called the **Bose-Hubbard Hamiltonian**

$$\hat{H} = \sum_{i}^{f} \nu_i \hat{b}_i^\dagger \hat{b}_i + \frac{1}{2} \sum_{i}^{f} U_i \hat{b}_i^\dagger \hat{b}_i^\dagger \hat{b}_i \hat{b}_i - \sum_{i,j=i\pm1}^{f} k_{ij} \hat{b}_i^\dagger \hat{b}_j \tag{B.20}$$

B.4 Characterization of the Fidelity Borders in the Banded Random Matrix Model

In Chapter 5 the RMT model of a banded matrix was introduced to model Anderson localized states. Using the LDoS methods outlined in Chapter 3, we calculate the actual energy dispersion, Eq.(3.45) and its PRT approximation, Eq.(3.47). In addition, we calculate Γ from normalization of the approximation in Eq.(3.43). The point at which $\Gamma \sim \Delta$ defines the border λ_c, which is shown in Fig.(B.1) - the red (lower solid) line displays Γ and the dotted line shows $\Delta \sim 1$.

In order to calculate λ_{prt}, we observe where the relation $\delta E_{\text{prt}} \approx \delta E$ diverges. This is also shown in the Fig.(B.1), in which the black (upper solid) line is δE and the dashed line is δE_{PRT}. For the system parameters of $N = 1000, b = 10$, the two borders from Fig.(B.1) are shown as two red dots, respectively at $\lambda_c, \lambda_{\text{prt}} \approx 0.053, 0.56$ - verifying our selections of $\lambda = 0.001 < \lambda_c$ and $\lambda_c < \lambda = 0.1 < \lambda_{\text{prt}}$ as the standard perturbative and Wigner (FGR) regimes within this section. We would like to stress the result shown in the numerics - within the Wigner (FGR) regime, Γ scales as $\Gamma \sim \lambda^2$.

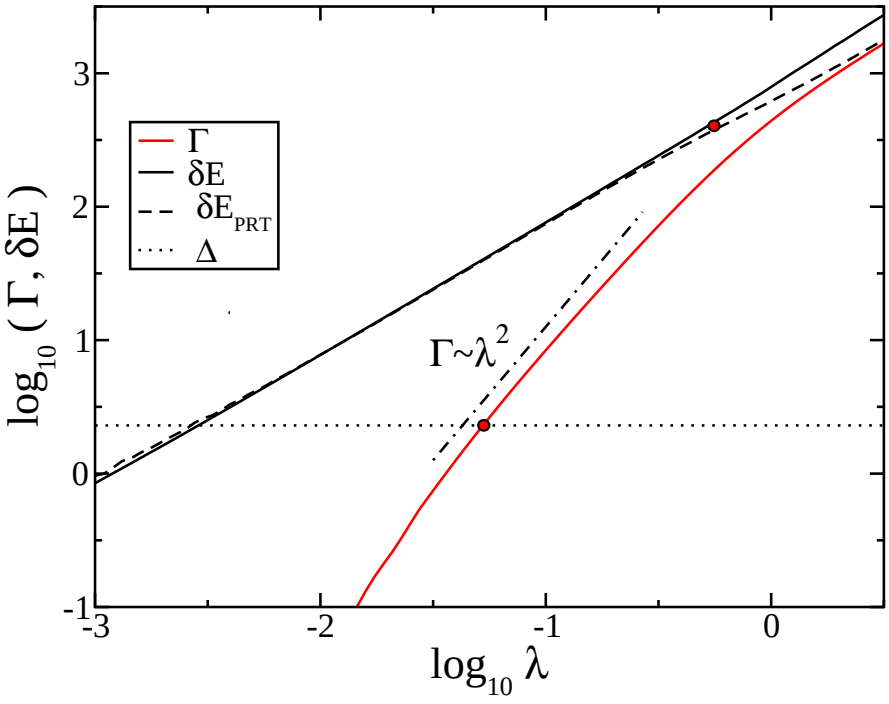

Figure (B.1): Defining the fidelity regime borders numerically - the dashed line shows the mean level spacing, $\Delta \sim 1$. The red (lower solid) line is the bandwidth of the PRT core-region, Γ. The point at which $\Gamma \sim \Delta$ is shown by the left red dot, and occurs for $\lambda_c \sim 0.053$. Also shown are the dispersion δE (black solid upper line) and its *PRT* approximation $\delta E_{\rm PRT}$. The point at which they diverge from one another is plotted as the right red dot, occuring for $\lambda_{\rm prt} \sim 0.56$. The dotted-dashed line displays the $\Gamma \sim \lambda_c^2$ scaling in the Wigner (FGR) regime.

B.5 The Box-Counting Method

Here, we discuss the *box-counting method* used in dimensional analysis of wave-functions. Consider a finite system of volume $V = L^d$, where d is the spatial dimension of the system [$d = 2$ in Fig. (7.1)], in which the eigenstates, $\psi(\mathbf{r})$, are

embedded. If the volume is divided into smaller subvolume cells ("boxes"), each with a scaled length of $L_b = \lambda L$ and volume $V_b = \lambda^d L^d$, so that the total number of boxes is $N = V/V_b = \lambda^{-d}$. What is the probability of finding a portion of the eigenstate within a box? For a given scaling λ, the answer is given by

$$P_b(\lambda) = \int_{V_b} d\mathbf{r} \, |\psi(\mathbf{r})|^2 , \tag{B.21}$$

$$\sum_b^N P_b(\lambda) = 1 \tag{B.22}$$

where the second equation follows from eigenstate normalization. The number of boxes that contain a portion of the eigenstate is then $N_b(\lambda)$. The *Minkowski-Bouligand dimension* is given as

$$D = \lim_{\lambda \to 0} \left(-\frac{\log N_b(\lambda)}{\log \lambda} \right) \tag{B.23}$$

or alternatively, as

$$\begin{aligned} \langle P_b \rangle &= N_b^{-1} \sum_b^N P_b(\lambda) \\ &\propto \lambda^D \end{aligned} \tag{B.24}$$

so that $N_b(\lambda) \simeq \lambda^{-D}$. This is illustrated in Fig. (B.2). For $0 < D < d$ and there exists a number of boxes such that $P_b(\lambda) = 0$, the eigenstates are said to be *single-fractal*. However, in critical systems, fluctuations exist at all scales, therefore $P_b(\lambda) > 0$ for every box at any λ. This gives $N_b = N$ (or $D = d$) showing

that the Minkowski-Bouligand dimension is not a good measure for the critical point.

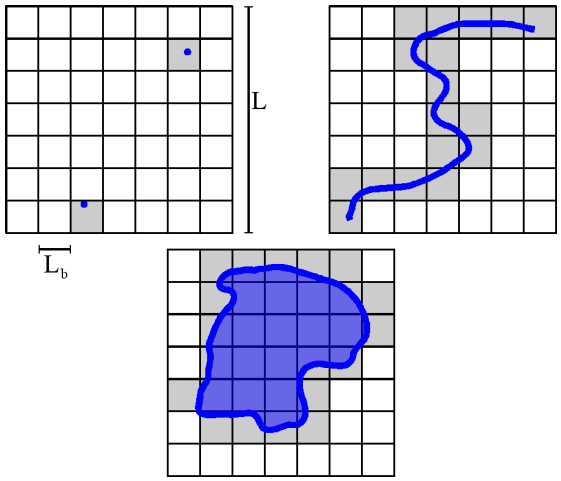

Figure (B.2): Box-counting method for a $L \times L$ volume, meshed with subvolumes of $L_b \times L_b$. For $L_b = \lambda L$, there are a total of $N = \lambda^{-2}$ finite elements. Eigenstates can appear 'point-like' (upper left), 'curve-like' (upper right) with a length of l, or 'area-like' (bottom) with an area of A. Subvolumes that contain a portion of an eigenstate are counted (shaded grey above) to yield a total of $N_b(\lambda)$. For the point-like states, we get $N_b = 2 \propto \lambda^0$. The curve-like states give $N_b = l/L_b \propto \lambda^{-1}$, and the area-like states give $A/L_b^2 \propto \lambda^{-2}$. Therefore the Minkowski-Bouligand dimension appears as λ^{-D}.

B.6 The WLRM Correlator

In Chapter 7, the WLRM correlator is given in Eq.(7.17). We will show the steps in deriving this equation here. We start with the general correlator from Eq.(3.11)

$$\mathcal{C}(\tau, \tau') = \langle \hat{B}(\tau)\hat{B}(\tau')\rangle_0 - \langle \hat{B}(\tau)\rangle_0 \langle \hat{B}(\tau')\rangle_0. \tag{B.25}$$

where $\langle\cdots\rangle_0 = \langle\psi_0|\cdots|\psi_0\rangle$. Expanding this average in the basis of $\hat{H}_0|n\rangle = E_n|n\rangle$ gives

$$\begin{aligned}\mathcal{C}(\tau,\tau') &= \sum_n \langle n|\, c_n^*\, e^{i\hat{H}_0\tau/\hbar}\hat{B}e^{-i\hat{H}_0\tau/\hbar}\cdot e^{i\hat{H}_0\tau'/\hbar}\hat{B}e^{-i\hat{H}_0\tau'/\hbar}\, c_n\,|n\rangle - \\ &\quad \sum_n \langle n|\, c_n^*\, e^{i\hat{H}_0\tau/\hbar}\hat{B}e^{-i\hat{H}_0\tau/\hbar}\, c_n\,|n\rangle \cdot \sum_m \langle m|\, c_m^*\, e^{i\hat{H}_0\tau/\hbar}\hat{B}e^{-i\hat{H}_0\tau/\hbar}\, c_m\,|m\rangle \\ &= \sum_n |c_n|^2 \langle n|\, e^{i\hat{H}_0\tau/\hbar}\hat{B}e^{-i\hat{H}_0\tau/\hbar}\cdot e^{i\hat{H}_0\tau'/\hbar}\hat{B}e^{-i\hat{H}_0\tau'/\hbar}\,|n\rangle - \\ &\quad \sum_n |c_n|^2 e^{iE_n\tau/\hbar}e^{-iE_n\tau/\hbar}B_{nn}\cdot\sum_m |c_m|^2 e^{iE_m\tau/\hbar}e^{-iE_m\tau/\hbar}B_{nn} \qquad \text{(B.26)}\end{aligned}$$

Noting a cancellation on the exponentials in the second term and inserting an identity sum into the first term gives

$$\begin{aligned}\mathcal{C}(\tau,\tau') &= \sum_{n,\gamma} |c_n|^2 \langle n|\, e^{i\hat{H}_0\tau/\hbar}\hat{B}e^{-i\hat{H}_0\tau/\hbar}\,|\gamma\rangle\langle\gamma|\, e^{i\hat{H}_0\tau'/\hbar}\hat{B}e^{-i\hat{H}_0\tau'/\hbar}\,|n\rangle - \\ &\quad \sum_n |c_n|^2 B_{nn}\cdot\sum_m |c_m|^2 B_{mm} \\ &= \sum_{n,\gamma} |c_n|^2 e^{iE_n\tau/\hbar}e^{-iE_\gamma\tau/\hbar}e^{iE_\gamma\tau'/\hbar}e^{-iE_n\tau'/\hbar}B_{n\gamma}B_{\gamma n} - \\ &\quad \sum_n |c_n|^2 B_{nn}\cdot\sum_m |c_m|^2 B_{nn} \\ &= \sum_{n,\gamma} |c_n|^2 e^{i\Delta_{n\gamma}(\tau-\tau')}B_{n\gamma}B_{\gamma n} - \sum_n |c_n|^2 B_{nn}\cdot\sum_m |c_m|^2 B_{nn} \qquad \text{(B.27)}\end{aligned}$$

where in the last line, we have used $\Delta_{n\gamma} = (E_n - E_\gamma)/\hbar$. Eq.(B.27) is now as far as one can go generally. Next, we note the variance σ_{ij} in Eq.(7.9) - for $\alpha = 1$ -

is a specific case of the element-element correlation

$$\langle B_{ij} B_{kl} \rangle = \sigma_{ij}^2 \cdot (\delta_{ik}\delta_{jl} + \delta_{il}\delta_{jk}) \tag{B.28}$$

$$\sigma_{ij}^2 = \frac{1}{1 + \left(\frac{|i-j|}{b}\right)^2} \tag{B.29}$$

Taking a disorder average over Eq.(B.27) allows us to utilize the above element-element correlation

$$\begin{aligned} \mathcal{C}(\tau, \tau') &= \sum_{n,\gamma} |c_n|^2 \, e^{i\Delta_{n\gamma}(\tau-\tau')} \langle B_{n\gamma} B_{\gamma n} \rangle - \sum_{n,m} |c_n|^2 \, |c_m|^2 \langle B_{nn} B_{mm} \rangle \\ &= \sum_{n,\gamma} |c_n|^2 \, e^{i\Delta_{n\gamma}(\tau-\tau')} \sigma_{n\gamma}^2 \left(\delta_{n\gamma}\delta_{\gamma n} + \delta_{nn}\delta_{\gamma\gamma}\right) - \\ &\quad \sum_{n,m} |c_n|^2 \, |c_m|^2 \left(\delta_{nm}\delta_{mn} + \delta_{nn}\delta_{mm}\right) \end{aligned} \tag{B.30}$$

We can contract across γ and m in the following way [note $\{n, \nu, m, \mu\}$ are dummy variables in Eq.(B.31)]

$$\sigma_{nm}^2 \left(\delta_{n\nu}\delta_{m\mu} + \delta_{n\mu}\delta_{m\nu}\right) = \begin{cases} 2\sigma_{nn}^2 = 2; & n = \nu = m = \mu \\ \sigma_{mn}^2 = \sigma_{nm}^2; & n = \nu \neq m = \mu \\ \sigma_{nm}^2; & n = m \neq \nu = \mu \\ 0; & n \neq \nu \neq m \neq \mu \end{cases} \tag{B.31}$$

Applying this then gives

$$\begin{aligned}\mathcal{C}(\tau,\tau') &= \sum_n |c_n|^2 \cdot 2 + \sum_{n,\gamma} |c_n|^2 \, e^{i\Delta_{n\gamma}(\tau-\tau')}\sigma_{n\gamma}^2 \cdot 2 - \sum_n |c_n|^4 \cdot 2 \\ &= 2\sum_n |c_n|^2 \left(1 + \sum_\gamma \sigma_{n\gamma}^2 e^{i\Delta_{n\gamma}(\tau-\tau')}\right) - 2\sum_n |c_n|^4 \end{aligned} \tag{B.32}$$

Since the the fidelity $\in \Re$ and its LRT approximation involves a time integration of the above, we can simply use the real part without loss of generality. Then

$$\mathcal{C}(\tau,\tau') = 2\sum_n |c_n|^2 \left\{1 + \sum_\gamma \sigma_{n\gamma}^2 \cos[\Delta_{n\gamma}(\tau-\tau')]\right\} - 2\sum_n |c_n|^4 \tag{B.33}$$

Noting then the bracketed term is nothing more than $\tilde{C}_n(\tau-\tau')$ of Eq.(7.18), and the second term is likewise the P_2. We have then arrived at

$$\mathcal{C}(\tau,\tau') = 2\sum_n |c_n|^2 \, \tilde{C}_n(\tau-\tau') - 2P_2 \tag{B.34}$$

whose double integration yields the correlator of Eq.(7.17).

B.7 Characterizing Regime Borders in Critical Fidelity

Within Chapter 7, we numerically analyze the fidelity of critical systems, and therefore wish to characterize the traditional three regimes of fidelity using the

same technique discussed in Chapter 3, namely using the LDoS profile. In the case of a critical WLRM, the LDoS analysis was performed extensively in [126, 162]. The first-order and infinite perturbation results are

$$P_{\mathrm{FOPT}}(r) = \frac{x^2 \left|B_{nm}\right|^2}{(E_n - E_m)^2} = \frac{x^2}{(\Delta r)^2} \frac{b^2}{b^2 + r^2},\ r \neq 0 \tag{B.35}$$

$$P_{\mathrm{PRT}}(r) = \frac{x^2 \left|B_{nm}\right|^2}{\Gamma^2 + (E_n - E_m)^2} = \frac{x^2}{(\Delta r)^2 + \Gamma^2} \frac{b^2}{b^2 + r^2} \tag{B.36}$$

where Γ is the core-width of the LDoS representing the width over which levels contribute significantly. As in Chapter 3, under ensemble averaging the variable r can been seen as an average energy separation $r = \langle E_n - E_m \rangle / \Delta$. Outside of the core-widths, $r \gg \Gamma$ we have

$$P_{\mathrm{FOPT,PRT}}(r \gg \Gamma) \sim \frac{1}{r^4} \tag{B.37}$$

Normalizing the area under Eq. (B.36) gives a value for the core-width

$$\Gamma(x) = \frac{b\Delta}{2} \left(\sqrt{1 + \frac{4\pi x^2}{b\Delta^2}} - 1 \right) \tag{B.38}$$

The border between standard perturbative and Wigner(FGR) regimes is defined at the point where levels begin to mix beyond nearest neighbor, at the point $\Gamma(x_c) \simeq \Delta$. Working this equation back to solve x_c gives

$$x_c \simeq \frac{\Delta}{\sqrt{\pi}} \sqrt{1 + b^{-1}} \tag{B.39}$$

The LDoS profiles are shown in Fig.(B.3), in which the upper figure is in the standard perturbative regime and the lower figure is in the Wigner(FGR) regime. The solid lines are the numerical LDoS profiles. The dotted lines are the perturbative approximations, Eqs.(B.35, B.36), and appear to capture nicely the LDoS behavior in the two regimes. The inset displays the behavior outside of the core region, Eq. (B.37).

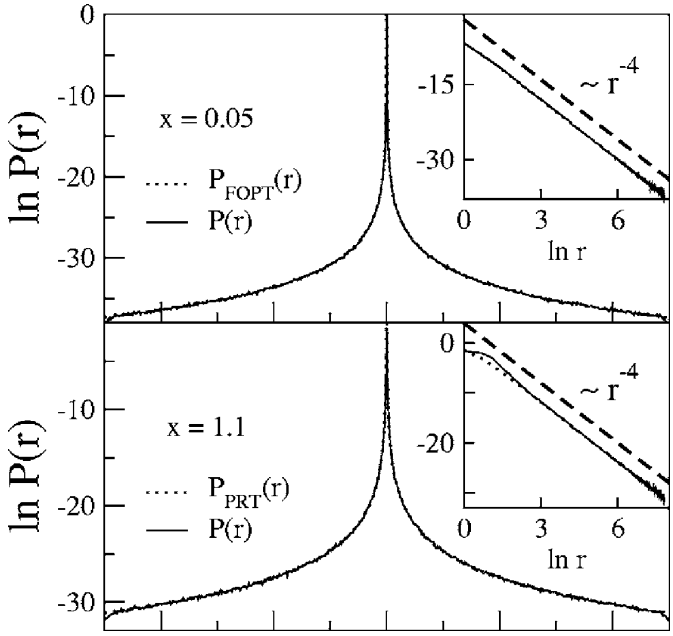

Figure (B.3): LDoS Profiles for the WLRM Model, $L = 5000, b = 1$, yielding $x_c \sim 0.8$. In the upper panel, $x = 0.05$, standard perturbative regime. The dotted line is the first order approximation, Eq. (B.35). In the lower panel, $x = 1.1$, Wigner(FGR) regime. In this case, the dotted line is the infinite order approximation, Eq. (B.36. Both approximations match nicely. Within the insets, the logarithms are plotted, to illustrate behavior outside of the two core-widths, Δ (standard perturbative) and Γ (Wigner (FGR)). Both show the expected r^{-4} dependence, drawn as a dashed line. Figure taken from [126].

In the non-perturbative regime, perturbative theory is no longer valid, and Eqs.(B.35, B.36) fail to capture the LDoS behavior. Specifically, the failure is that the LDoS has a core no longer following a Lorentzian lineshape, Eq. (B.36), but a crossover to a semicircular behavior [126]. This failure is illustrated in Fig. (B.4).

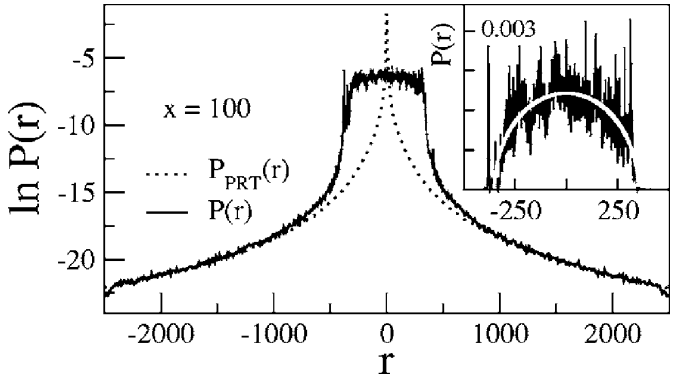

Figure (B.4): LDoS Profiles for the WLRM Model, $L = 5000, b = 1$, in the nonperturbative regime $x_{prt} \sim 1.5 \gg x = 100$. The solid line corresponds to the actual numerical LDoS, and the dotted line to Eq.(B.36). In contrast to Fig.(B.3), the peturbative approximation fails to capture the core behavior. Within the inset, the core behavior is displayed to be semicircular. Figure taken from [126].

In order to find the border between Wigner(FGR) and non-perturbative regimes, x_{prt}, we must find the point at which Eq.(B.36) fails. This 'failing point' is defined as the x value which the dispersion of Eq.(B.36)

$$\delta E_{\mathrm{PRT}} = \Delta \sqrt{\sum_r r^2 P_{\mathrm{PRT}}(r)} \tag{B.40}$$

fails to adequately match the dispersion of the actual LDoS

$$\delta E = x \sum_{n \neq m} |B_{nm}|^2 \tag{B.41}$$

These sums can then be calculated numerically. If however, the sums are taken to a continous limit, $\sum_n, \sum_r \rightarrow \int dr, B_{nm} \rightarrow B(r)$, the analytical integrations yield

$$\delta E_{\mathrm{PRT}} \approx xb\sqrt{\pi} \left(b + \frac{\Gamma}{\Delta} \right)^{-1/2}, \tag{B.42}$$

$$\delta E \approx x\sqrt{2b} \left[\frac{\pi}{2} - \mathrm{atan}\left(b^{-1}\right) \right]^{1/2} \tag{B.43}$$

The non-perturbative border is then found analytically by setting $\delta E \approx \delta E_{\mathrm{PRT}}$ [126], to yield

$$x_{prt} = \Delta\sqrt{b} \frac{\sqrt{\pi - 2\left[\frac{\pi}{2} - \mathrm{atan}\left(b^{-1}\right)\right]}}{2\left[\frac{\pi}{2} - \mathrm{atan}\left(b^{-1}\right)\right]} \tag{B.44}$$

Both the numerical dispersions, Eqs. (B.40, B.41), are plotted in Fig.(B.5).

In addition, the analytical formulae for the dispersions, Eqs.(B.42, B.43), are overplotted. A match between all is observed for $x < x_{prt}$ (here, $x_{prt} = 5.35$). At the points where $x > x_{prt}$, a clear deviation between the dispersions is seen. The analytical form of $\Gamma(x)$, Eq. (B.38), is overlaid as well for comparison.

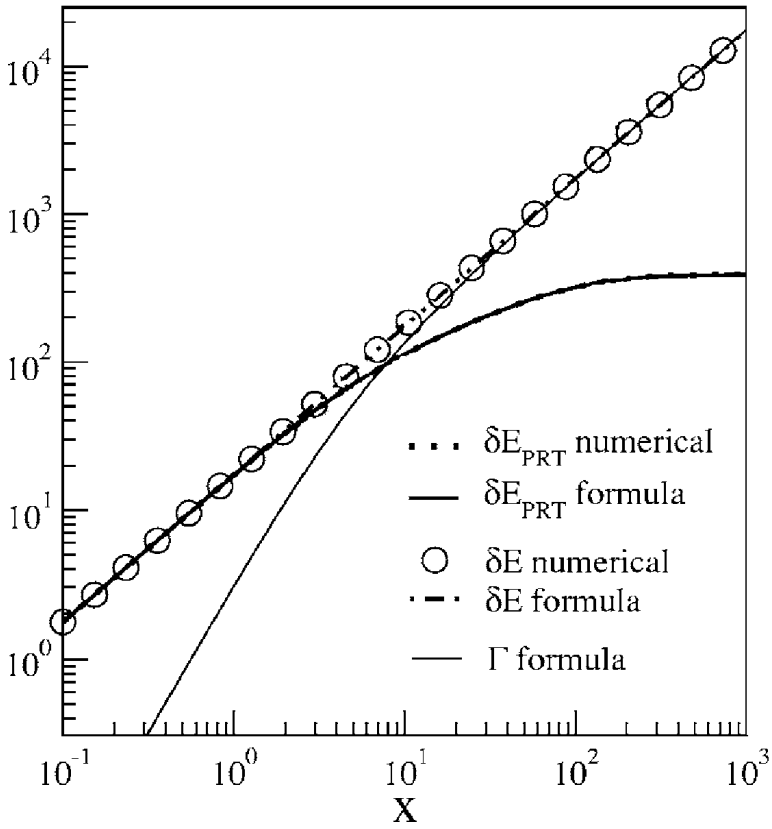

Figure (B.5): Dispersion versus perturbation strength, for $L = 5000, b = 100$. The numerical dispersions, Eqs. (B.40, B.41), are respectively shown as a dotted line and circles. The analytic dispersions, Eqs. (B.42, B.43), are respectively shown as a dash-dotted line and a heavy solid line. A nice agreement between all dispersions is seen, up to $x_{prt} \sim 5.35$, at which point the perturbative expressions deviate and become sublinear, $\propto \sqrt{x}$. The thin solid line displays the core-width $\Gamma(x)$ - Eq. (B.38) - for comparison. Figure taken from [126].

Bibliography

[1] J. Bodyfelt, M. Hiller, & T. Kottos, 'Engineering fidelity echoes in Bose-Hubbard Hamiltonians'. *Europhys. Lett.*, **78**, 50003 (2007).

[2] J. Bodyfelt, M. Zheng, T. Kottos, U. Kuhl, & H.-J. Stöckmann, 'Probing Localization in Absorbing Systems via Loschmidt Echos' (2009).
URL `http://arxiv.org/abs/0901.4544`

[3] G. Ng, J. Bodyfelt, & T. Kottos, 'Critical Fidelity'. *Phys. Rev. Lett.*, **97**, 256404 (2006).

[4] J. Bodyfelt, J. Méndez-Bermúdez, A. Chabanov, & T. Kottos, 'Scaling properties of delay times in one-dimensional random media'. *Phys. Rev. B*, **77**, 045103 (2007).

[5] H. Goldstein, C. Poole, & J. Safko, *Classical Mechanics*. 3rd edition (Addison Wesley, 2002), ISBN 0-201-65702-3.

[6] P. Cvitanović, R. Artuso, R. Mainieri, G. Tanner, & G. Vattay, 'Chaos: Classical and Quantum' (2008).
URL `http://www.ChaosBook.org`

[7] L. Reichl, *The Transition to Chaos: Conservative Classical Systems and Quantum Manifestations*. Institute for Nonlinear Science, 2nd edition (Springer, New York, 2004), ISBN 0-387-98788-6.

[8] 'The Visible Human Project' (2008).
URL `http://www.nlm.nih.gov/research/visible/`

[9] E. Milotti, '1/f noise: a pedagogical review' (2002).
URL `http://arxiv.org/abs/physics/0204033`

[10] P. Bak, C. Tang, & K. Wiesenfeld, 'Self-Organized Criticality: An Explanation of 1/f Noise'. *Phys. Rev. Lett.*, **59**, 381 (1987).

[11] E. Faleiro, U. Kuhl, R. Molina, A. Relaño, J. Retamosa, & H.-J. Stöckmann, '1/f noise in experimental Sinai quantum billiards' (2005).
URL `http://arxiv.org/abs/cond-mat/0502192`

[12] M. Mehta, *Random Matrices*. 2nd edition (Academic Press, 1991), ISBN 0124880517.

[13] J. Sakurai, 'Modern Quantum Mechanics'. Revised edition (Addison Wesley, 1994), ISBN 978-0201539295.

[14] T. Brody, J. Flores, J. Fench, P. Mello, A. Pandey, & S. Wong, 'Random-matrix physics: spectrum and strength fluctuations'. *Rev. Mod. Phys.*, **53**, 385 (1981).

[15] H.-J. Stöckmann, *Quantum Chaos* (Cambridge University Press, 1999), ISBN 0521592844.

[16] T. Guhr, A. Müller-Groeling, & H. Weidenmüller, 'Random-Matrix Theories in Quantum Physics: Common Concepts'. *Phys. Rep.*, **299**, 189 (1998).

[17] O. Bohigas, M. J. Giannoni, & C. Schmit, 'Characterization of Chaotic Quantum Spectra and Universality of Level Fluctuation Laws'. *Phys. Rev. Lett.*, **52**, 1 (1984).

[18] S. Chandrasekhar, 'Stochastic Problems in Physics and Astronomy'. *Rev. Mod. Phys.*, **15**, 1 (1943).

[19] A. Peres, 'Stability of quantum motion in chaotic and regular systems'. *Phys. Rev. A*, **30**, 1610 (1984).

[20] F. Cucchietti, H. Pastawski, & D. Wisniacki, 'Decoherence as Decay of the Loschmidt Echo in a Lorentz Gas'. *Phys. Rev. E*, **65**, 045206 (2002).

[21] T. Gorin, T. Prosen, T. Seligman, & M. Žnidarič, 'Dynamics of Loschmidt echoes and fidelity decay'. *Phys. Rep.*, **435**, 33 (2006).

[22] F. M. Cucchietti, C. H. Lewenkopf, E. R. Mucciolo, H. M. Pastawski, & R. O. Vallejos, 'Measuring the Lyapunov exponent using quantum mechanics'. *Phys. Rev. E*, **65**, 046209 (2002).

[23] F. Cucchietti, H. Pastawski, & R. Jalabert, 'Universality of the Lyapunov regime for the Loschmidt echo'. *Phys. Rev. B*, **70**, 035311 (2004).

[24] F. Cucchietti, C. Lewenkopf, & H. Pastawski, 'Decay of the Loschmidt echo in a time-dependent environment'. *Phys. Rev. E*, **74**, 026207 (2006).

[25] T. Gorin, T. Prosen, & T. Seligman, 'A random matrix formulation of fidelity decay'. *New J. of Phys.*, **6**, 20 (2004).

[26] D. Cohen, 'Chaos and Energy Spreading for Time-Dependent Hamiltonians, and the various Regimes in the Theory of Quantum Dissipation'. *Ann. Phys.*, **283**, 175 (2000).

[27] D. Cohen & T. Kottos, 'Parametric dependent Hamiltonians, wavefunctions, random-matrix-theory, and quantal-classical correspondence'. *Phys. Rev. E*, **63**, 36203 (2001).

[28] M. Hiller, D. Cohen, T. Geisel, & T. Kottos, 'Wavepacket Dynamics, Quantum Reversibility and Random Matrix Theory'. *Ann. Phys.*, **321**, 1025 (2006).

[29] D. Jaksch, C. Bruder, J. Cirac, C. Gardiner, & P. Zoller, 'Cold Bosonic Atoms in Optical Lattices'. *Phys. Rev. Lett.*, **81**, 3108 (1998).

[30] T. Calarco, U. Dorner, P. Julienne, C. Williams, & P. Zoller, 'Quantum computations with atoms in optical lattices: Marker qubits and molecular interactions'. *Phys. Rev. A*, **70**, 012306 (2004).

[31] D. Jaksch & P. Zoller, 'The cold atom Hubbard toolbox'. *Ann. Phys.*, **315**, 52 (2005).

[32] E. Cornell, W. Ketterle, & C. Wieman, 'Les Prix Nobel-2001' (Nobel Foundation, 2002).

[33] G. Ekspong (Editor) *Nobel Lectures in Physics 1991-1995* (World Scientific Publishing Company, 1997), ISBN 981-02-2677-2.

[34] J. Fritz, M. Baller, H. Lang, H. Rothuizen, P. Vettiger, E. Meyer, H.-J. Günterodt, C. Gerber, & J. Gimzewski, 'Translating Biomolecular Recognition into Nanomechanics'. *Science*, **288**, 316 (2000).

[35] M. Sato, B. Hubbard, A. Sievers, B. Ilic, D. Czaplewski, & H. Craighead, 'Observation of Locked Intrinsic Localized Vibrational Modes in a Micromechanical Oscillator Array'. *Phys. Rev. Lett.*, **90**, 044102 (2003).

[36] J. Eilbeck, P. Lomdahl, & A. Scott, 'The discrete self-trapping equation'. *Physica D*, **16**, 318 (1985).

[37] A. C. Scott, P. S. Lomdahl, & J. C. Eilbeck, 'Between the local-mode and normal-mode limits'. *Chem. Phys. Lett.*, **113**, 29 (1985).

[38] A. C. Scott & J. C. Eilbeck, 'On the CH stretch overtones of benzene'. *Chem. Phys. Lett.*, **132**, 23 (1986).

[39] A. C. Scott, L. Bernstein, & J. C. Eilbeck, 'Local modes in molecules'. *J. Mol. Liq.*, **41**, 105 (1989).

[40] A. Scott, L. Bernstein, & J. Eilbeck, 'Energy levels of the quantized discrete self-trapping equation'. *J. of Bio. Phys.*, **17**, 1 (1989).

[41] E. Wright, J. Eilbeck, M. Hays, P. Miller, & A. Scott, 'The quantum discrete self-trapping equation in the Hartree approximation'. *Physica D*, **69**, 18 (1993).

[42] P. Binder, D. Abraimov, A. Ustinov, S. Flach, & Y. Zolotaryuk, 'Observation of Breathers in Josephson Ladders'. *Phys. Rev. Lett.*, **84**, 745 (2000).

[43] E. Trías, J. Mazo, & T. Orlando, 'Discrete Breathers in Nonlinear Lattices: Experimental Detection in a Josephson Array'. *Phys. Rev. Lett.*, **84**, 741 (2000).

[44] R. Meyer, S. E. Korshunov, C. Leemann, & P. Martinoli, 'Dimensional crossover and hidden incommensurability in Josephson junction arrays of periodically repeated Sierpinski gaskets'. *Phys. Rev. B*, **66**, 104503 (2002).

[45] M. Albiez, R. Gati, J. Folling, S. Hunsmann, M. Cristiani, & M. Oberthaler, 'Direct Observation of Tunneling and Nonlinear Self-Trapping in a Single Bosonic Josephson Junction'. *Phys. Rev. Lett.*, **95**, 010402 (2005).

[46] C. Bruder, R. Fazio, & G. Schön, 'The Bose-Hubbard model: from Josephson junction arrays to optical lattices'. *Ann. Physik*, **14**, 566 (2005).

[47] M. Hiller, T. Kottos, & T. Geisel, 'Complexity in parametric Bose-Hubbard Hamiltonians and structural analysis of eigenstates'. *Phys. Rev. A*, **73**, 061604 (2006).

[48] M. Hiller, T. Kottos, & T. Geisel, 'Wave-packet dynamics in energy space of a chaotic trimeric Bose-Hubbard system'. *Phys. Rev. A*, **79** (2009).

[49] C. Petitjean, D. Bevilaqua, E. Heller, & P. Jacquod, 'Displacement Echoes: Classical Decay and Quantum Freeze'. *Phys. Rev. Lett.*, **98**, 164101 (2007).

[50] J. Liu, W. Wang, C. Zhang, Q. Niu, & B. Li, 'Fidelity of a Bose-Einstein Condensate'. *Phys. Rev. A*, **72**, 063623 (2005).

[51] A. Chefles, 'Nearest-neighbour level spacings for the non-periodic discrete nonlinear Schrödinger equation'. *J. Phys. A*, **29**, 4515 (1996).

[52] S. de Filippo, M. Fusco-Girard, & M. Salerno, 'Avoided-crossing and nearest-neighbour level spacings for the quantum DST equation'. *Nonlinearity*, **2**, 477 (1989).

[53] F. Cucchietti, 'Loschmidt echo in the Bose-Hubbard Model: turning back time in an optical lattice' (2006).
URL `http://arxiv.org/abs/quant-ph/0609202v1`

[54] M. Andersen, A. Kaplan, & N. Davidson, 'Echo spectroscopy and quantum stability of trapped atoms'. *Phys. Rev. Lett.*, **90**, 023001 (2003).

[55] M. Andersen, T. Grünzweig, A. Kaplan, & N. Davidson, 'Revivals of coherence in chaotic atom-optics billiards'. *Phys. Rev. A*, **69**, 063413 (2004).

[56] M. Andersen, A. Kaplan, T. Grünzweig, & N. Davidson, 'Decay of Quantum Correlations in Atom Optics Billiards with Chaotic and Mixed Dynamics'. *Phys. Rev. Lett.*, **97**, 104102 (2006).

[57] M. Molina & G. Tsironis, 'Dynamics of self-trapping in the discrete nonlinear Schrödinger-equation'. *Physica D*, **65**, 267 (1993).

[58] M. Molina & G. Tsironis, 'Disorder in the discrete nonlinear schrödinger-equation'. *Int. J. of Mod. Phys. B*, **9**, 1899 (1995).

[59] H.-J. Stöckmann & R. Schäfer, 'Recovery of the fidelity amplitude for the Gaussian ensembles'. *New J. Phys.*, **6**, 199 (2004).

[60] H.-J. Stöckmann & R. Schäfer, 'Fidelity Recovery in Chaotic Systems and the Debye-Waller Factor'. *Phys. Rev. Lett.*, **94**, 244101 (2005).

[61] R. Schäfer, H.-J. Stöckmann, T. Gorin, & T. H. Seligman, 'Experimental Verification of Fidelity Decay: From Perturbative to Fermi Golden Rule Regime'. *Phys. Rev. Lett.*, **95**, 184102 (2005).

[62] C. Pineda, R. Schäfer, T. Prosen, & T. Seligman, 'First verification of generic fidelity recovery in a dynamical system'. *Phys. Rev. E*, **73**, 066120 (2006).

[63] V. Kenkre & G. Tsironis, 'Nonlinear effects in quasielastic neutron scattering: Exact line-shape calculation for a dimer'. *Phys. Rev. B*, **35**, 1473 (1987).

[64] V. Kenkre & D. Campbell, 'Self-trapping on a dimer: Time-dependent solutions of a discrete nonlinear Schrödinger equation'. *Phys. Rev. B*, **34**, R4959 (1986).

[65] P. Jacquod, P. Silvestrov, & C. Beenakker, 'Golden rule decay versus Lyapunov decay of the quantum Loschmidt echo'. *Phys. Rev. E*, **64**, 055203 (2001).

[66] P. Jacquod, I. Adagideli, & C. Beenakker, 'Anomalous power law of quantum reversibility for classically regular dynamics'. *Europhys. Lett.*, **61**, 729 (2003).

[67] M. Hiller, T. Kottos, D. Cohen, & T. Geisel, 'Quantum Reversibility: Is there an Echo?' *Phys. Rev. Lett.*, **92**, 010402 (2004).

[68] P. Anderson, 'Absence of Diffusion in Certain Random Lattices'. *Phys. Rev.*, **109**, 1492 (1958).

[69] T. Brandes & S. Kettemann (Editors) *Anderson Localization and Its Ramifications*. Lecture Notes in Physics (Springer-Verlag, 2003), ISBN 3-540-40785-5.

[70] S. John, 'Electromagnetic Absorption in a Disordered Medium near a Photon Mobility Edge'. *Phys. Rev. Lett.*, **53**, 2169 (1984).

[71] M. Gurvitch, 'Ioffe-Regel criterion and resistivity of metals'. *Phys. Rev. B*, **24**, 7404 (1981).

[72] E. Abrahams, P. W. Anderson, D. C. Licciardello, & T. V. Ramakrishnan, 'Scaling Theory of Localization: Absence of Quantum Diffusion in Two Dimensions'. *Phys. Rev. Lett.*, **42**, 673 (1979).

[73] F. Evers & A. Mirlin, 'Anderson Transitions'. *Rev. Mod. Phys.*, **80**, 1355 (2008).

[74] H. De Raedt, A. Lagendijk, & P. de Vries, 'Transverse Localization of Light'. *Phys. Rev. Lett.*, **62**, 47 (1989).

[75] A. Chabanov, M. Stoytchev, & A. Genack, 'Statistical Signatures of Photon Localization'. *Nature*, **404**, 850 (2000).

[76] A. Chabanov & A. Genack, 'Statistics of Dynamics of Localized Waves'. *Phys. Rev. Lett.*, **87**, 233903 (2001).

[77] A. Genack & A. Chabanov, 'Signatures of photon localization'. *J. Phys. A*, **38**, 10465 (2005).

[78] J. Edwards & D. Thouless, 'Numerical Studies of Localization in Disordered Systems'. *J. Phys. C*, **5**, 807 (1972).

[79] H. Hu, A. Strybulevych, J. Page, S. Skipetrov, & B. van Tiggelen, 'Localization of Ultrasound in a Three-Dimensional Elastic Network'. *Nature-Phys.*, **4**, 945 (2008).

[80] T. Schwartz, G. Bartal, S. Fishman, & M. Segev, 'Transport and Anderson localization in disordered two-dimensional photonic lattices'. *Nature*, **446**, 05623 (2007).

[81] J. Billy, V. Josse, Z. Zuo, A. Bernard, B. Hambrecht, P. Lugan, D. Clément, L. Sanchez-Palencia, P. Bouyer, & A. Aspect, 'Direct observation of Anderson localization of matter-waves in a controlled disorder'. *Nature*, **453**, 891 (2008).

[82] K. Efetov, *Supersymmetry in Disorder and Chaos* (Cambridge University Press, 1997), ISBN 0-521-47097-8.

[83] Y. Fyodorov & A. Mirlin, 'Scaling Properties of Localization in Random Band Matrices - A Sigma-Model Approach'. *Phys. Rev. Lett.*, **67**, 2405 (1991).

[84] Y. Fyodorov & A. D. Mirlin, 'The Statistics of Eigenvector Components of Random Band Matrices - Analytical Results'. *J. Phys. A*, **26**, L551 (1993).

[85] Y. Fyodorov & A. Mirlin, 'Statistical Properties of Eigenfunctions of Random Quasi 1D One-Particle Hamiltonians'. *Int. J. of Mod. Phys. B*, **8**, 3795 (1994).

[86] G. Casati, I. Guarneri, F. Izrailev, L. Molinari, & K. Życzkowski, 'Periodic Band Random Matrices, Curvature, and Conductance in Disordered Media'. *Phys. Rev. Lett.*, **72**, 2697 (1994).

[87] F. Izrailev, 'Scaling properties of spectra and eigenfunctions for quantum dynamical and disordered systems'. *Chaos, Solitons and Fractals*, **5**, 1219 (1995).

[88] T. Kottos, A. Politi, F. Izrailev, & S. Ruffo, 'Scaling properties of Lyapunov spectra for the band random matrix model'. *Phys. Rev. E*, **53**, R5553 (1996).

[89] F. Izrailev, T. Kottos, A. Politi, & G. Tsironis, 'Evolution of wave packets in quasi-1D and 1D random media: diffusion versus localization'. *Phys. Rev. E*, **55**, 4951 (1997).

[90] T. Kottos, A. Politi, & F. Izrailev, 'Finite-Size Corrections in Lyapunov Spectra for Band Random Matrices'. *J. Phys. C*, **10**, 5965 (1998).

[91] T. Kottos, F. Izrailev, & A. Politi, 'Finite-length Lyapunov exponents and conductance for quasi-1D disordered solids'. *Physica D*, **131**, 155 (1999).

[92] P. Kunstman, K. Życzkowski, & J. Zakrzewski, 'Nonuniversality in level dynamics'. *Phys. Rev. E*, **55**, 2446 (1997).

[93] Y. Fyodorov, 'Distribution of "level velocities" in quasi 1D disordered or chaotic systems with localization'. *Phys. Rev. Lett.*, **73**, 2688 (1994).

[94] H. Baranger & P. Mello, 'Mesoscopic transport through chaotic cavities: A random S-matrix theory approach'. *Phys. Rev. Lett.*, **73**, 142 (1994).

[95] A. D. Mirlin, R. Pnini, & B. Shapiro, 'Intensity distribution for waves in disordered media: Deviations from Rayleigh statistics'. *Phys. Rev. E*, **57**, R6285 (1998).

[96] A. A. Chabanov & A. Z. Genack, 'Statistics of the mesoscopic field'. *Phys. Rev. E*, **72**, 055602 (2005).

[97] M. E. Gertsenshtein & V. B. Vasil'ev, 'Waveguides with Random Inhomogeneities and Brownian Motion In the Lobachevsky Plane'. *Theory of Probability and its Applications*, **4**, 391 (1959).

[98] U. Kuhl, *Microwave scattering on Complex Systems* (Fachbereich Physik der Phillips-Universität Marburg, 2008), Habilitation Thesis.

[99] R. Schäfer, *Correlation functions and fidelity decay in chaotic systems*. Ph.D. thesis, Fachbereich Physik der Phillips-Universität Marburg (2004).

[100] H. Weidenmüller, 'Statistical theory of nuclear reactions and the Gaussian orthogonal ensemble'. *Ann. Phys.*, **158**, 120 (1984).

[101] R. Schäfer, T. Gorin, T. H. Seligman, & H. J. Stöckmann, 'Fidelity amplitude of the scattering matrix in microwave cavities'. *New J. Phys.*, **7**, 152 (2005).

[102] A. Barnett, D. Cohen, & E. Heller, 'Deformations and Dilations of Chaotic Billiards: Dissipation Rate, and Quasiorthogonality of the Boundary Wave Functions'. *Phys. Rev. Lett.*, **85**, 1412 (2000).

[103] J. Analytis, S. Blundell, & A. Ardavan, 'Landau levels, electric dipole transitions, and the Hofstadter butterfly in finite lattices'. *J. Phys. IV France*, **114**, 283 (2004).

[104] G. Ng & T. Kottos, 'Wavepacket dynamics of the nonlinear Harper model'. *Phys. Rev. B*, **75**, 205120 (2007).

[105] U. Kuhl & H.-J. Stöckmann, 'Microwave Realization of the Hofstadter Butterfly'. *Phys. Rev. Lett.*, **80**, 3232 (1998).

[106] A. García-García & J. Wang, 'Anderson Transition in Quantum Chaos'. *Phys. Rev. Lett.*, **94**, 244102 (2005).

[107] C. West, T. Prosen, & T. Kottos, 'Loschmidt Gap in Dynamical Systems with Critical Chaos' (2008).
URL `http://arxiv.org/abs/0812.3994`

[108] A. Furusaki, 'Recent progress in the theory of Anderson localization' (2006).
URL `http://www.physics.hku.hk/ ctcp/HKForum/index_files/talks/Furusaki.ppt`

[109] D. Braun, E. Hofstetter, G. Montambaux, & A. MacKinnon, 'Boundary conditions, the critical conductance distribution, and one-parameter scaling'. *Phys. Rev. B*, **64**, 155107 (2001).

[110] D. G. Polyakov, 'Critical Conductance of a Mesoscopic System: Interplay of the Spectral and Eigenfunction Correlations at the Metal-Insulator Transition'. *Phys. Rev. Lett.*, **81**, 4696 (1998).

[111] R. Ketzmerick, K. Kruse, S. Kraut, & T. Geisel, 'What Determines the Spreading of a Wave Packet?' *Phys. Rev. Lett.*, **79**, 1959 (1997).

[112] J. Chalker & G. Daniell, 'Scaling, Diffusion, and the Integer Quantized Hall Effect'. *Phys. Rev. Lett.*, **61**, 593 (1988).

[113] J. Chalker, 'Scaling and eigenfunction correlations near a mobility edge'. *Physica A*, **167**, 253 (1990).

[114] B. Huckestein & R. Klesse, 'Wave-packet dynamics at the mobility edge in two- and three-dimensional systems'. *Phys. Rev. B*, **59**, 9714 (1999).

[115] J. Méndez-Bermúdez & T. Kottos, 'Probing the eigenfunction fractality using Wigner delay times'. *Phys. Rev. B*, **72**, 064108 (2005).

[116] G. Ekspong (Editor) *Nobel Lectures in Physics 1981-1990* (World Scientific Publishing Company, 1993).

[117] D. Tsui, H. Stormer, & A. Gossard, 'Two-dimensional Magnetotransport in the Extreme Quantum Limit'. *Phys. Rev. Lett.*, **48**, 1559 (1982).

[118] D. Hofstadter, 'Energy levels and wave functions of Bloch electrons in rational and irrational magnetic fields'. *Phys. Rev. B*, **14**, 2239 (1976).

[119] P. Harper, 'Single Band Motion of Conduction Electrons in a Uniform Magnetic Field'. *Proc. Phys. Soc. Lond. A*, **68**, 874 (1955).

[120] A. Mirlin, Y. Fyodorov, F.-M. Dittes, J. Quezada, & T. Seligman, 'Transition from localized to extended eigenstates in the ensemble of power-law random banded matrices'. *Phys. Rev. E*, **54**, 3221 (1996).

[121] V. E. Kravtsov & K. A. Muttalib, 'New Class of Random Matrix Ensembles with Multifractal Eigenvectors'. *Phys. Rev. Lett.*, **79**, 1913 (1997).

[122] A. D. Mirlin & F. Evers, 'Multifractality and critical fluctuations at the Anderson transition'. *Phys. Rev. B*, **62**, 7920 (2000).

[123] I. Varga, 'Fluctuation of correlation dimension and inverse participation number at the Anderson transition'. *Phys. Rev. B*, **66**, 094201 (2002).

[124] E. Cuevas, 'Two-level correlation function of critical random-matrix ensembles'. *Phys. Rev. B*, **71**, 024205 (2005).

[125] V. Kravtsov & A. Tsvelik, 'Energy level dynamics in systems with weakly multifractal eigenstates: equivalence to 1D correlated fermions'. *Phys. Rev. B*, **62**, 9888 (2000).

[126] J. Méndez-Bermúdez, T. Kottos, & D. Cohen, 'Parametric invariant random matrix model and the emergence of multifractality'. *Phys. Rev. E*, **73**, 036204 (2006).

[127] B. Huckestein & R. Klesse, 'Spatial and spectral multifractality of the local density of states at the mobility edge'. *Phys. Rev. B*, **55**, R7303 (1997).

[128] U. Kuhl, F. Izrailev, & A. Krokhin, 'Enhancement of Localization in One-Dimensional Random Potentials with Long-Range Correlations'. *Phys. Rev. Lett.*, **100**, 126402 (2008).

[129] I. Bloch, J. Dalibard, & W. Zwerger, 'Many-body physics with ultracold gases'. *Rev. Mod. Phys.*, **80**, 885 (2008).

[130] 'Quantum Phase Transition from a Superfluid to a Mott Insulator in a Gas of Ultracold Atoms' (2007), Johannes Gutenberg-Universität Mainz, Zentrum für Datenverarbeitung.
URL `http://www.quantum.physik.uni-mainz.de/bec/experiments/mottinsulator.html`

[131] L. Molinari, 'Scaling of distribution eigenvectors in a 1D Anderson model'. *J. Phys: Cond. Mat.*, **5**, L319 (1993).

[132] G. Casati & L. Molinari, 'Scaling Properties of Band Random Matrics'. *Phys. Rev. Lett.*, **64**, 1851 (1990).

[133] F. Izrailev, 'Scaling Properties of Spectra and Eigenfunctions for Quantum Dynamical and Disordered Systems'. *Chaos, Solitons, and Fractals*, **5**, 1219 (1995).

[134] G. Casati, I. Guarneri, F. Izrailev, S. Fishman, & L. Molinari, 'Scaling of the information length in 1D tight-binding models'. *J. Phys.: Cond. Mat.*, **4**, 149 (1992).

[135] F. Izrailev, T. Kottos, & G. Tsironis, 'Scaling properties of the localization length in one-dimensional paried correlated binary alloys of finite size'. *J. Phys.: Cond. Mat.*, **8**, 2823 (1996).

[136] E. Wigner, 'Lower Limit for the Energy Derivative of the Scattering Phase Shift'. *Phys. Rev.*, **98**, 145 (1955).

[137] F. Smith, 'Lifetime Matrix in Collision Theory'. *Phys. Rev.*, **118**, 349 (1960).

[138] C. A. A. de Carvalho & H. M. Nussenzveig, 'Time delay'. *Phys. Rep.*, **364**, 83 (2002).

[139] A. Ossipov & Y. Fyodorov, 'Statistics of delay times in mesoscopic systems as a manifestation of eigenfunction fluctuations'. *Phys. Rev. B*, **71**, 125133 (2005).

[140] J. Méndez-Bermúdez & T. Kottos, 'Probing the eigenfunction fractality using Wigner delay times'. *Phys. Rev. B*, **72**, 064108 (2005).

[141] F. Evers & A. D. Mirlin, 'Fluctuations of the Inverse Participation Ratio at the Anderson Transition'. *Phys. Rev. Lett.*, **84**, 3690 (2000).

[142] F. Wegner, 'Disordered electronic system as a model of interacting matrices'. *Phys. Rep.*, **67**, 15 (1980).

[143] A. Mirlin, Y. Fyodorov, A. Mildenberger, & F. Evers, 'Exact Relations between Multifractal Exponents at the Anderson Transition'. *Phys. Rev. Lett.*, **97**, 046803 (2006).

[144] A. Ossipov, T. Kottos, & T. Geisel, 'Statistical properties of phases and delay times of the one-dimensional Anderson model with one open channel'. *Phys. Rev. B*, **61**, 11411 (2000).

[145] F. Izrailev & A. Krokhin, 'Localization and the Mobility Edge in One-Dimensional Potentials with Correlated Disorder'. *Phys. Rev. Lett.*, **82**, 4062 (1999).

[146] U. Kuhl, F. Izrailev, A. Krokhin, & H.-J. Stöckmann, 'Experimental observation of the mobility edge in a waveguide with correlated disorder'. *Appl. Phys. Lett.*, **77**, 633 (2000).

[147] A.Krokhin, F. Izrailev, U. Kuhl, H.-J. Stöckmann, & S. Ulloa, 'Random 1D structures as filters for electrical and optical signals'. *Physica E*, **13**, 695 (2002).

[148] D. Dunlap, H.-L. Wu, & P. Phillips, 'Absence of localization in a random-dimer model'. *Phys. Rev. Lett.*, **65**, 88 (1990).

[149] P. Phillips & H.-L. Wu, 'Localization and its abscence - a new metallic state for conducting polymers'. *Science*, **252**, 1805 (1991).

[150] F. Izrailev, T. Kottos, & G. Tsironis, 'Hamiltonian map approach to resonant states in paired correlated binary alloys'. *Phys. Rev. B*, **52**, 3274 (1995).

[151] F. de Moura & M. Lyra, 'Delocalization in the 1D Anderson Model with Long-Range Correlated Disorder'. *Phys. Rev. Lett.*, **81**, 3735 (1998).

[152] H. Shima, T. Nomura, & T. Nakayama, 'Localization-delocalization transition in one-dimensional electron systems with long-range correlated disorder'. *Phys. Rev. B*, **70**, 075116 (2004).

[153] P. Carpena, P. Bernaola-Galván, P. Ivanov, & H. Stanley, 'Metal-insulator transition in chains with correlated disorder'. *Nature*, **418**, 955 (2002).

[154] P. Carpena, P. Bernaola-Galván, & P. Ivanov, 'New Class of Level Statistics in Correlated Disordered Chains'. *Phys. Rev. Lett.*, **93**, 176804 (2004).

[155] V. Bellani, E. Diez, R. Hey, L. Toni, L. Tarricone, G. B. Parravicini, F. Domínguez-Adame, & R. Gómez-Alcalá, 'Experimental Evidence of Delocalized States in Random Dimer Superlattices'. *Phys. Rev. Lett.*, **82**, 2159 (1999).

[156] A. Rodríguez, V. A. Malyshev, G. Sierra, M. A. Martín-Delgado, J. Rodríguez-Laguna, & F. Domínguez-Adame, 'Anderson Transition in Low-Dimensional Disordered Systems Driven by Long-Range Nonrandom Hopping'. *Phys. Rev. Lett.*, **90**, 027404 (2003).

[157] A. Rodríguez, V. Malyshev, & F. Domínguez-Adame, 'Quantum diffusion and lack of universal one-parameter scaling in one-dimensional disordered lattices with long-range coupling'. *J. Phys. A*, **33**, L161 (2000).

[158] A. V. Malyshev, V. A. Malyshev, & F. Domínguez-Adame, 'Monitoring the localization-delocalization transition within a one-dimensional model with nonrandom long-range interaction'. *Phys. Rev. B*, **70**, 172202 (2004).

[159] Y. Fyodorov & A. Mirlin, 'Analytical Derivation of the Scaling Law for the Inverse Participation Ratio in Quasi-One-Dimensional Disordered Systems'. *Phys. Rev. Lett.*, **69**, 1093 (1992).

[160] A. Mirlin & Y. Fyodorov, 'The statistics of eigenvector components of random band matrices: analytical results'. *J. Phys. A*, **26**, L551 (1993).

[161] S. Strogatz, *Nonlinear Dynamics and Chaos*. Studies in Nonlinearity (Perseus Books Publishing, 1994).

[162] J. Méndez-Bermúdez, T. Kottos, & D. Cohen, 'Parametric evolution of eigenstates: Beyond perturbation theory and semiclassics'. *Phys. Rev. E*, **72**, 027201 (2005).